2006-05-26

Development and Comparison of Highly Directional Loudspeakers

Gordon Robert Dix
Brigham Young University - Provo

DEVELOPMENT AND COMPARISON OF HIGHLY

DIRECTIONAL LOUDSPEAKERS

by

Gordon R. Dix

A thesis submitted to the faculty of

Brigham Young University

in partial fulfillment of the requirements for the degree of

Master of Science

Department of Physics and Astronomy

Brigham Young University

August 2006

BRIGHAM YOUNG UNIVERSITY

GRADUATE COMMITTEE APPROVAL

of a thesis submitted by

Gordon R. Dix

This thesis has been read by each member of the following graduate committee and by majority vote has been found to be satisfactory.

_____	_____
Date	Timothy W. Leishman, Chair
_____	_____
Date	Scott D. Sommerfeldt
_____	_____
Date	Jonathan D. Blotter

BRIGHAM YOUNG UNIVERSITY

As chair of the candidate's graduate committee, I have read the thesis of Gordon R. Dix in its final form and have found that (1) its format, citations, and bibliographical style are consistent and acceptable and fulfill university and department style requirements; (2) its illustrative materials including figures, tables, and charts are in place; and (3) the final manuscript is satisfactory to the graduate committee and is ready for submission to the university library.

_____   _____
Date   Timothy W. Leishman
                                          Chair, Graduate Committee

Accepted for the Department

_____   _____
Date   Ross L. Spencer
                                          Graduate Coordinator
                                          Department of Physics and Astronomy

Accepted for the College

_____   _____
Date   Tom W. Sederberg
                                          Associate Dean, College of Physical and
                                          Mathematical Sciences

ABSTRACT

DEVELOPMENT AND COMPARISON OF HIGHLY

DIRECTIONAL LOUDSPEAKERS

Gordon R. Dix

Department of Physics and Astronomy

Master of Science

Highly directive loudspeakers have long been important tools for sound system designers, experimental acousticians, and many other professionals in the audio industry. They allow sound engineers to more easily manipulate the radiation pattern of their loudspeakers to accommodate the purpose of the venue. Many commercially available products, while exhibiting good directivity at mid and high frequencies, generally lack control in the low frequency range. A new method for controlling the radiation pattern of a loudspeaker at low frequencies has been developed and modeled extensively. Prototypes have been built and tested in an anechoic chamber. Results from computer modeling and experimental measurements will be presented and compared in this thesis.

ACKNOWLEDGEMENTS

TABLE OF CONTENTS

LIST OF TABLES

LIST OF FIGURES

Chapter 2

Chapter 3

Chapter 4

Chapter 8

Appendix A

GLOSSARY OF SYMBOLS

This glossary contains variables that are used repeatedly in this thesis.

a_h Hole radius (m)

a_t Tube radius (m)

Bl Motor strength or strength factor

c Speed of sound in air (343 m/s)

$\tilde{c}$ Complex speed of sound in air

c_p Specific heat for constant pressure

C Compliance

C_{AB} Acoustic compliance of the loudspeaker enclosure

C_{MS} Mechanical compliance of driver suspension

e_g Electrical input voltage

G Relative sensitivity

f Frequency (Hz)

f_c Cutoff frequency for the first cross mode of the shotgun tube

F_s Free-air resonance frequency of driver

I Current

j Imaginary number $\left(\sqrt{-1}\right)$

j_{mn} Spherical Bessel function zeros

k Wavenumber $\left(\dfrac{\omega}{c}\right)$

$\widetilde{k}$ Complex wavenumber

L Distance between elements in an array

L_e Series inductance term for the voice coil

L_g Width of air gap between driver and shotgun tube

m Mass

M_{AB} Acoustic mass of the loudspeaker enclosure

M_{AR} Imaginary part of the radiation impedance

M_{MS} Moving mass of driver diaphragm assembly including the air loading

N Number of elements in an array

p Pressure

p_{dB} Far-field pressure measured in units of dB

P_r Prandtl number

Q Quality factor

Q_{MS} Mechanical quality factor

r Measurement point distance from center of source

R Complex reflection coefficient

R_{12} Real part of the mutual radiation impedance

R_{AB} Acoustic resistance of the loudspeaker enclosure

R_{AR} Real part of the radiation impedance

R_e DC resistance of driver voice coil

R_g Output impedance of signal generator

R_{MS} Mechanical resistance of driver suspension

R_α Ratio of pressures as defined by Olson

S Cross-sectional area of shotgun tube

S_g Cross-sectional area of air gap between driver and shotgun tube

S_D Effective radiating surface area of driver

t Thickness of shotgun tube wall

U Volume velocity, particle velocity multiplied by surface area

V Volume

X_{12} Imaginary part of the mutual radiation impedance

Z Impedance

Z_{12} Mutual radiation impedance

$Z_{A,B}$ Acoustic impedance of the loudspeaker enclosure

$Z_{A,D}$ Acoustic impedance of the driver's mechanical structure

$Z_{A,VC}$ Acoustic impedance of the driver's motor structure

Z_H Impedance of a hole in a shotgun tube

Z_I Input impedance

Z_o Impedance of a small length of tube

Z_r Radiation impedance of an orifice

Z_{RAD} General radiation impedance

Z_{TA} Impedance of an anechoic termination

Z_{TC} Impedance of a rigid termination

Z_{TD} Impedance of a drone cone termination

Z_{TO} Impedance of an open termination

α Sound absorption coefficient

α_c Classical absorption coefficient for losses

α_T	Total losses coefficient
α_w	Losses coefficient due to boundary interactions
γ	Ratio of specific heats
η	Coefficient of shear viscosity
θ	Angle from normal of shotgun tube axis to measurement point
κ	Thermal conductivity
λ	Wavelength
μ	Absolute viscosity
ρo	Ambient density of air ($1.21 \ kg/m^3$)
τ	Delay between elements in an array
ω	Angular frequency (rad/s)

CHAPTER 1

INTRODUCTION

Highly directional loudspeakers have long been important tools for sound system designers, acousticians, and many other professionals in the audio industry. They allow them to more easily control the radiation patterns of loudspeaker systems and accommodate the purposes of given venues. Museum displays, CD listening stations, and computer kiosks are a few commercial audio applications that have taken advantage of highly directional sound sources. Small loudspeaker arrays, loudspeakers mounted inside large domes or parabolic reflectors, and horns are typically the only cost-effective options available to professionals in order to achieve any substantial degree of directivity in these applications. These types of products exhibit good directivity control for mid and high frequencies, but generally lack control at lower frequencies. They are thus unacceptable for many applications wherein it is necessary to reproduce the entire audible frequency range.

The union of digital signal processing (DSP) and large arrays of loudspeakers to obtain high degrees of directional control has recently been accepted by the professional audio industry for many sound reinforcement applications. Passive arrays of loudspeakers naturally exhibit a more directional radiation pattern due to the basic physical principles involved in their radiation. However, once DSP was properly applied to those arrays, it gave audio professionals the ability to optimize control of radiation patterns and adjust them to meet specific needs and applications. Once again, these arrays can be very directional in the high and mid frequency ranges, but the amount of

control achieved at lower frequencies is proportional to the size of the array. Thus, more control in the bass region of the audio spectrum requires a much larger and undoubtedly more expensive array. The required size and cost of such arrays prevent many professionals from using them in their designs.

One might ask why control of the radiation at low frequencies is so desirable. There are several reasons. First, lower tones more easily mask higher tones. This is due to the mechanics of the ear, or more specifically, the method by which the cochlea responds to the sound waves incident upon the ear drum. If a sound field has an excess of low frequency energy, then higher frequency bands will likely be masked and clarity will suffer. For example, consider a museum that has two displays, each of which plays an audio track intended to be confined to a small listening area directly in front of it. If the low-frequency content of one source is not controlled, leakage to adjacent sound fields occurs, resulting in this masking phenomenon.

Second, in a given sound field, sound pressure waves can interact with each other, resulting in constructive and destructive interference. The likelihood of undesirable interference may be increased by the failure to use highly directional loudspeakers.

Outdoor noise control is yet another problem in which a solution can be found in highly directional sound sources. An example of this problem is outdoor concert venues. These performance areas are commonly found near residential neighborhoods. Mid and high frequencies can easily be focused only on the listening areas using traditional techniques, but uncontrolled low-frequency sound is allowed to leak into adjacent residential areas if no steps are taken to direct this energy towards the audience.

Along those same lines, sound in an enclosed space can seem too reverberant, or "boomy", if low-frequency energy is not directed toward a defined listening position as opposed to radiating omnidirectionally. This results in undesirable room resonance effects causing interference and masking for the listener.

All these problems point to a need for a low-cost highly directional loudspeaker that performs well at low frequencies. This industry need served as our motivation for this research.

1.1 Objectives

The primary goals of this research were to design, model, construct and experimentally evaluate a low-cost highly directional loudspeaker that performs well in the low frequency region where control is most difficult. A passive end-fire array or "shotgun" loudspeaker was eventually chosen as the focus of the research. A mathematical model of the device was created and predictions of the performance were extracted and compared to physical measurements. Current audio industry standards use the 6 dB down points on either side of the on-axis response to define the beamwidth of a directional device. This measure was chosen to gauge the directivity of the models and prototypes. It should be noted, however, that the levels of side lobes can also have an impact on the perceived ability of a device to contain sound and should not be completely ignored. Nevertheless, this research primarily uses the industry-standard beamwidth and on-axis frequency response to evaluate performance.

The designs and prototypes were intended to be inexpensive and reasonably compact, while maintaining many desirable characteristics of larger and much more

expensive commercially available systems. Simplicity in design and manufacturing were of primary importance.

A secondary goal of the research was to compare the performance of the prototypes to the performance of relatively low-cost directional loudspeakers of the parabolic reflector variety. The intent was to create a new design that outperformed these existing loudspeakers while reducing manufacturing costs.

1.2 Literature Review

A thorough literature search on past publications and patents relating to the topic of interest was completed as part of the research project. The searches branched out into other related fields and became an excellent method of collecting useful information. Articles on directional microphones [1-4] gave great insight on unique procedures for manipulating sound waves. Many of the techniques could be applied in reverse for controlling the radiation of loudspeakers. Because specific microphone designs are well guarded by microphone manufacturers, very few references are available that go into much detail. However, some excellent references by Ted N. Carnes [1] and Harry F. Olson [2] were found to be very helpful in understanding how the devices functioned.

Another motive for carrying out the literature search was to understand and become aware of all previous attempts to create directional low-frequency loudspeakers. Marinus M. Boone [5] and Harry F. Olson [6] published two well-known methods to accomplish this. They are each unique in their implementation, but are based on the same basic physical principles to achieve their goals. Both methods can produce dipole, cardioid and hypercardioid directivity functions, as opposed to an omnidirectional

directivity function (or monopole) that is characteristic of most commercial products at low frequencies. Boone uses two drivers and feeds each a unique amplitude weighted signal. The weighting function can be changed to obtain a desired directivity function. Olson simply changes the effective positions of the two drivers by adding delays to achieve the same directivity functions.

Each of these two designs focuses on control of the lower frequency bands in the audible spectrum and demonstrates substantial improvements over what was currently commercially available. Although they did not achieve the level of control we wished to attain, their methods and theory could help us in creating and evaluating our own models.

Perhaps the most interesting paper that surfaced in the search was one authored by Holland and Fahy [7]. They developed a low-cost directional sound source that was similar to the shotgun loudspeaker proposed in this research. Their device used many of the same principles as our own prototypes, but there are many differences in the modeling procedure and frequency ranges of interest. Much of this research overlaps with theirs, but it also goes well beyond their conclusions and investigates many areas left untouched by their analysis.

1.3 Plan of Development

The chapters in this thesis will proceed as follows. Chapter 2 will outline the governing physical principles, advantages, and disadvantages of several directional devices and explain the reason for selecting the basic design we chose. Chapter 3 will focus on the physics of the shotgun microphone and shotgun loudspeaker, and discuss the assumptions made in our model. The mathematical model for the shotgun loudspeaker

will then be presented in Chapter 4 and the analysis of the system will be detailed. Chapter 5 will discuss the numerical model results and describe the effect that shotgun tube characteristics have on the resulting beamwidth. Chapter 6 will discuss the prototypes that were built, measured, and compared to modeling results, and then draw several conclusions from the measurements. Improvements to the numerical model will be detailed in Chapter 7 and again compared to the measured data. Refined conclusions are also presented. Chapter 8 looks into several further investigations for the shotgun tube. Finally, Chapter 9 will compare the final shotgun tube design with existing products and draw some general conclusions for the research. Possibilities for future work will also be discussed.

CHAPTER 2

PROTOTYPE SELECTION

As indicated earlier, many existing products exhibit reasonable directivity control at mid and high frequencies, but generally lack control in the lower frequency range. It is this lack of control that has lead to this investigation for a new inexpensive loudspeaker that maintains many desirable characteristics of larger and much more expensive commercially available systems. This chapter will discuss the theory behind several loudspeakers that were considered (but not selected as the final design) and the benefits and drawbacks of each. It also discusses certain principles that are pertinent to the shotgun loudspeaker discussed in Chapter 3.

2.1   Domes

Sound focusing domes, such as the device shown in Fig. 2.1, are frequently found in low-budget installations where isolation of sound is desired at a given location. Common venues where these devices are found include information booths or tradeshow kiosks. They attempt to beam sound directly below the dome to prevent "bleeding" into adjacent listening areas. This is done by placing a small loudspeaker beneath the dome. It faces upward into the dome, which reflects the sound back down toward the listener.

Many different done shapes have been developed, each claiming to reach different levels of performance due to design innovations. The two most common types are parabolic and hemispherical. The parabolic domes place the driver at the focal point of the reflector to form a "beam" or "pillar" of sound directly beneath the dome, as shown in

Fig. 2.2 (a). The hemispherical dome, on the other hand, places the driver off-center in an attempt to create an area where the sound is focused down to a single point, as shown in Fig. 2.2 (b).

Figure 2.1. Commercial sound focusing domes (Soundtube FP6030). Used with permission from Soundtube Entertainment.
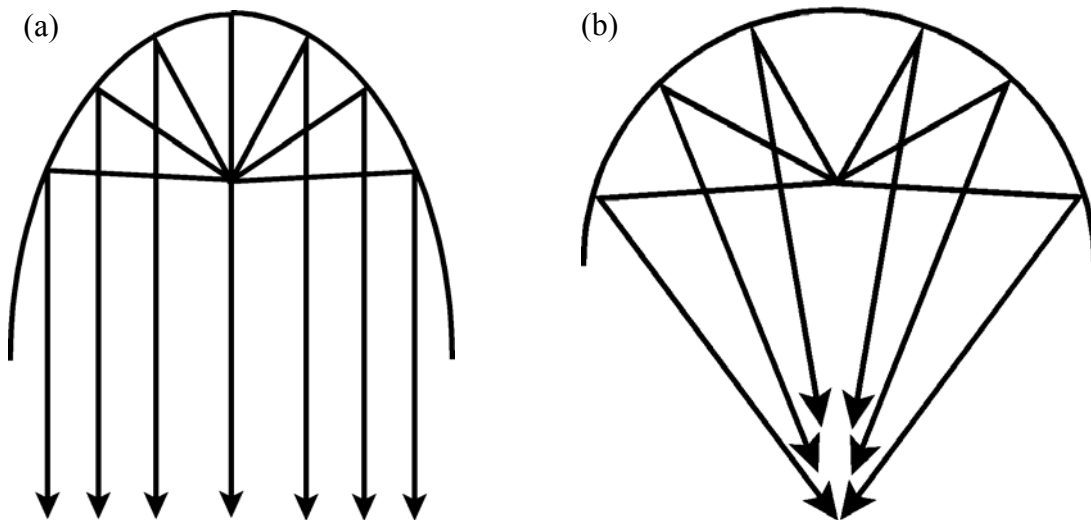
Figure 2.2. Sound focusing dome schematics. (a) Parabolic dome. (b) Hemispherical dome.

We obtained three commercial domes for testing. Each dome was taken into the anechoic chamber and the far-field pressure was measured and plotted for many different

frequencies. This was done by fabricating a stand (shown in Fig. 2.3) that mounted to a turntable and held the domes horizontally. This setup was centered in the center of a stationary arc of 19 microphones, giving an angular resolution of 5 degrees. The turntable was rotated every 5 degrees and the full arc of 19 microphones recorded the frequency dependant pressure amplitude at each position.

Figure 2.3. Dome measurement stand mounted to the turntable.

Figures 2.4 through 2.9 are a few example balloon plots that show the behavior of each design at two frequencies. These figures show the upper hemisphere of the radiated sound measured around the devices. The length of the radius from the origin to the

balloon plot surface is proportional to the level (in dB) of the measured sound. The wire

mesh surrounding each surface corresponds to a perfect hemisphere with amplitude equal

to the maximum value of the surface, or the on-axis value. This is done to more clearly

illustrate the omnidirectional characteristics of these devices. Simple inspection of the

plots shows that at 300 Hz, the devices are quite omnidirectional while at higher

frequencies, a frontal lobe begins to form increasing the directionality of the device.
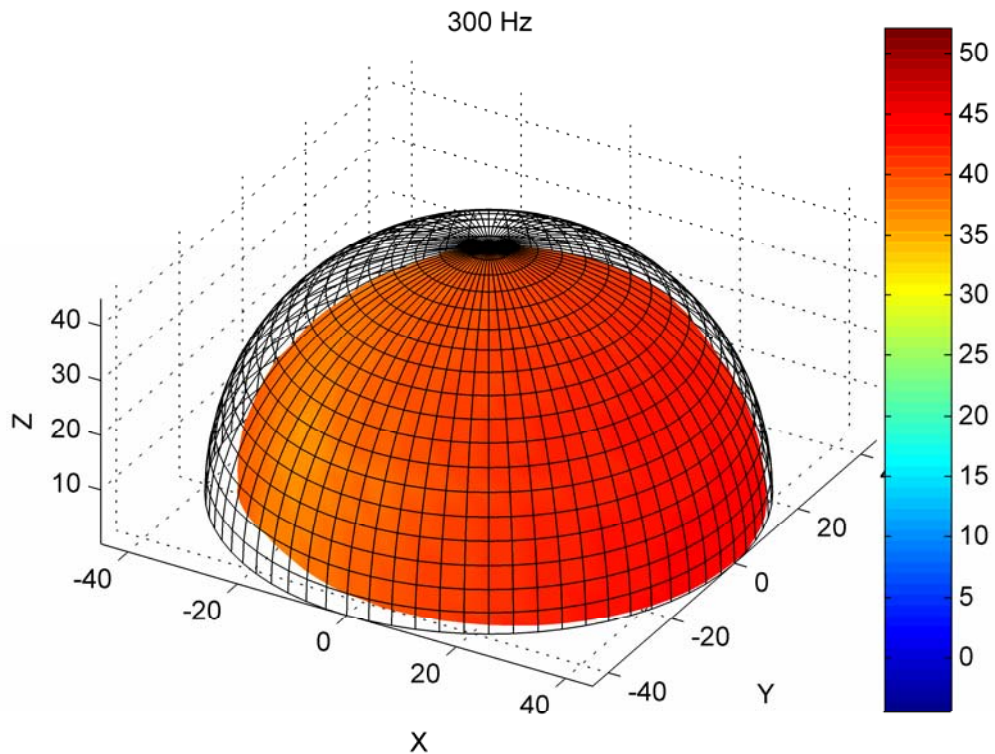
Figure 2.4. Dome #1: A dual-parabolic dome beam pattern for 300 Hz.
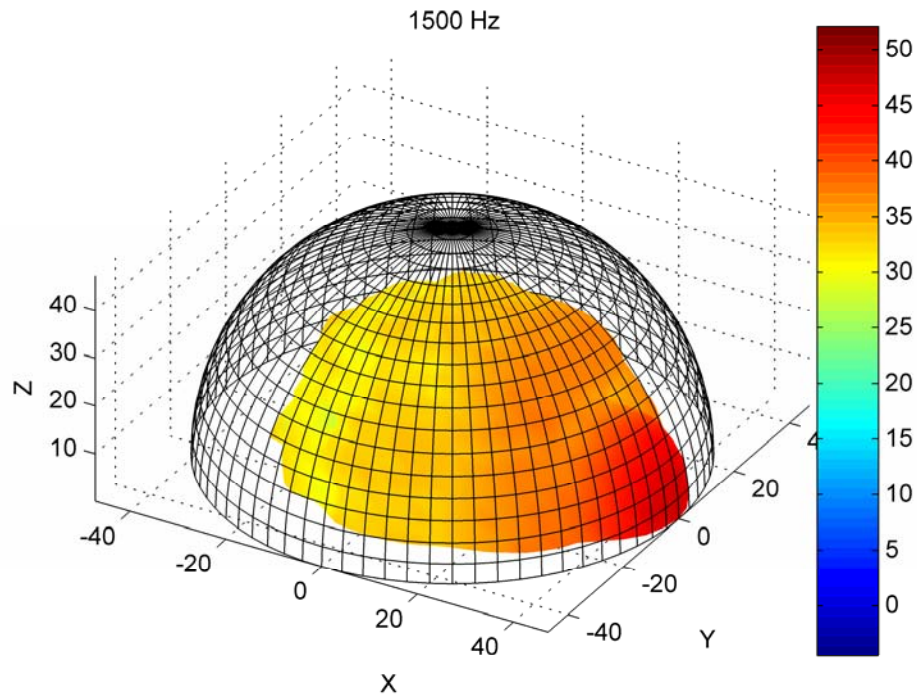
Figure 2.5. Dome #1: A dual-parabolic dome beam pattern for 1500 Hz.
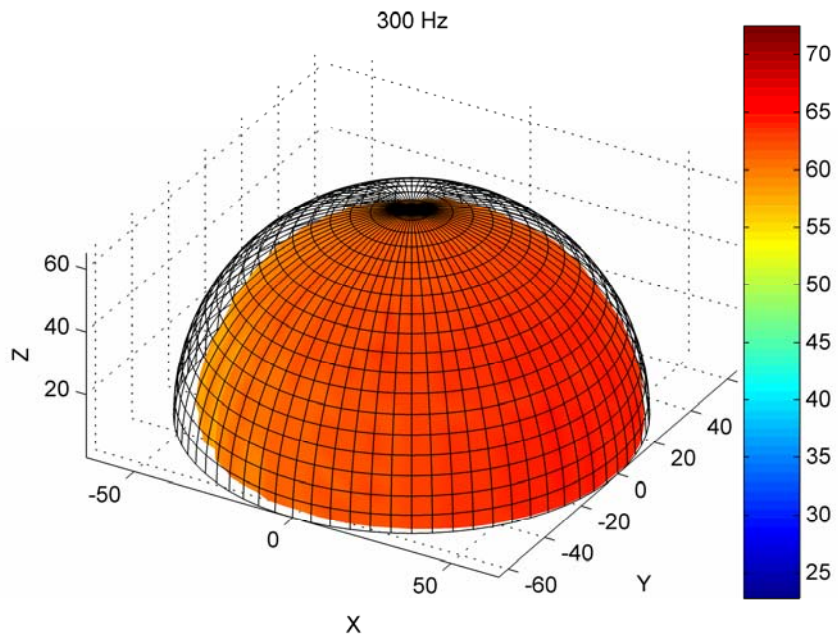
Figure 2.6. Dome #2: A hemispherical dome beam pattern for 300 Hz.
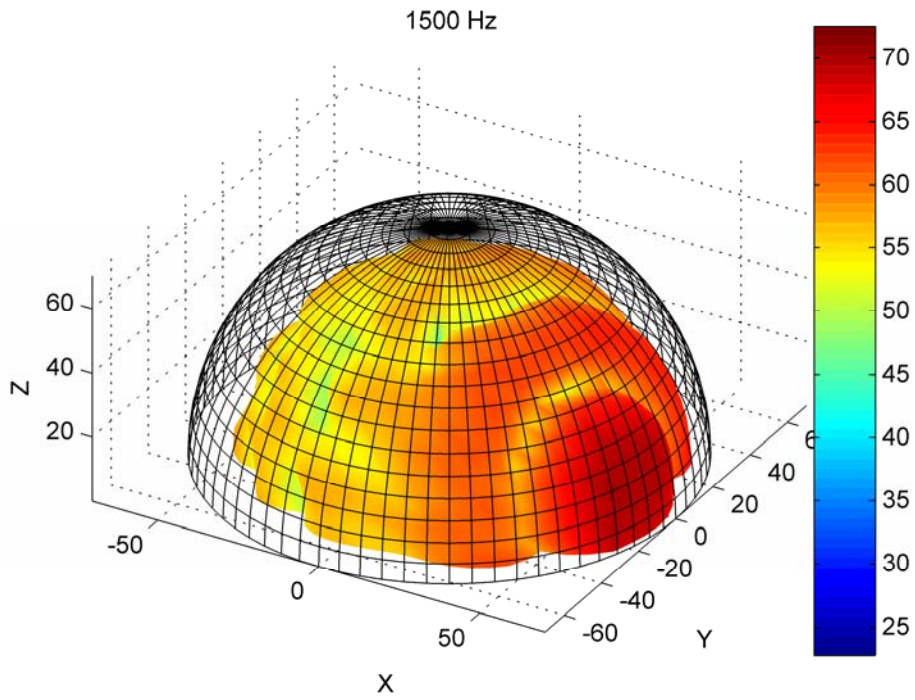
Figure 2.7. Dome #2: A hemispherical dome beam pattern for 1500 Hz.
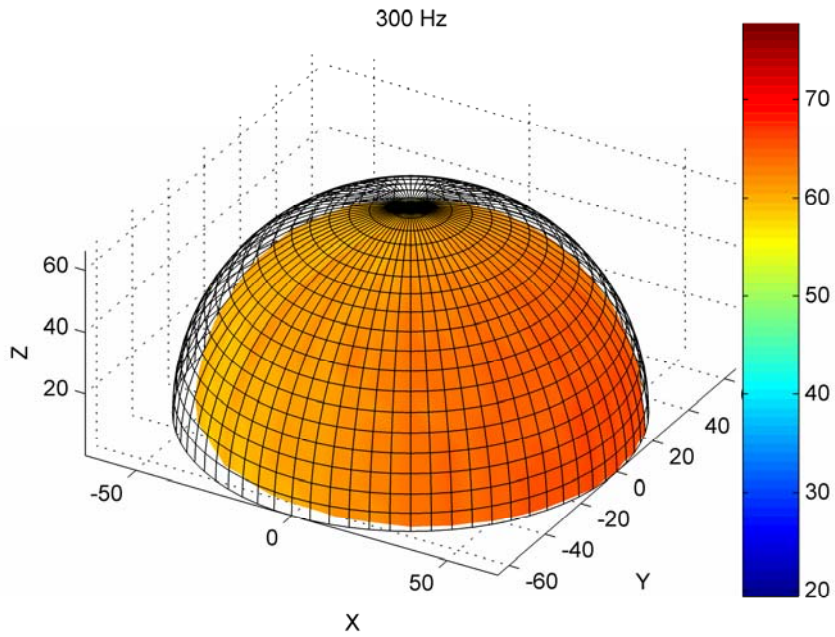
Figure 2.8. Dome #3: A parabolic dome beam pattern for 300 Hz.
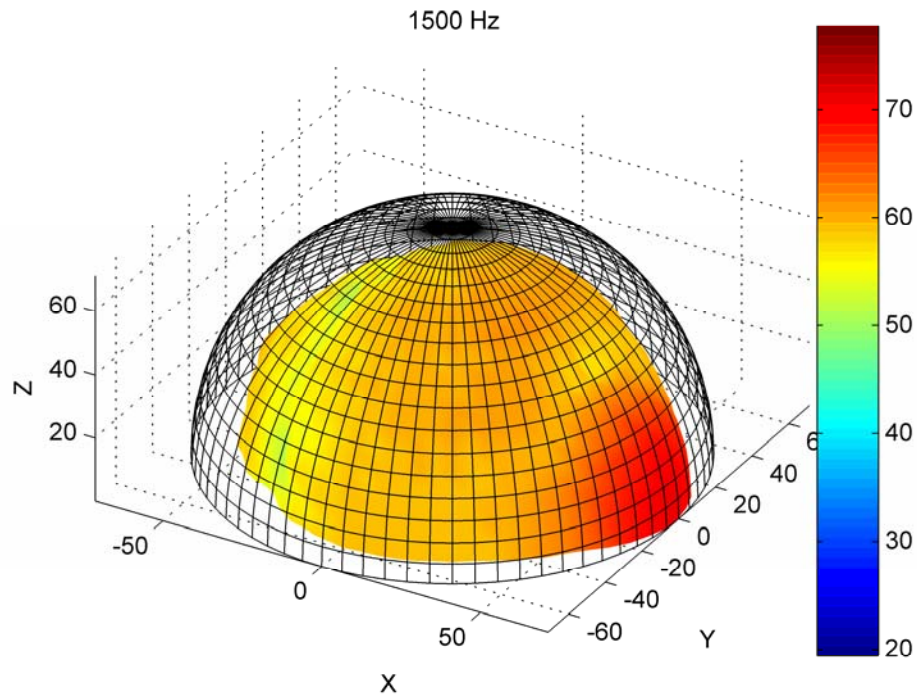
Figure 2.9. Dome #3: A parabolic dome beam pattern for 1500 Hz.

Figures 2.10, 2.11, and 2.12 are the same three domes, but now the horizontal polar plots for three different frequencies are shown. This is done to show how the radiation pattern evolves over frequency. Notice that the horizontal polar plots in these figures correspond to the footprint of the previous balloon plots.
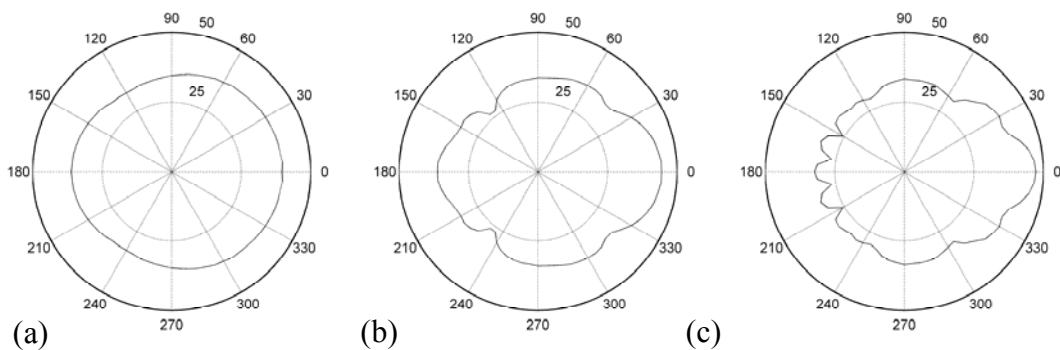
Figure 2.10. Dome #1: a dual-parabolic dome. (a) 300 Hz. (b) 800 Hz. (c) 1500 Hz.
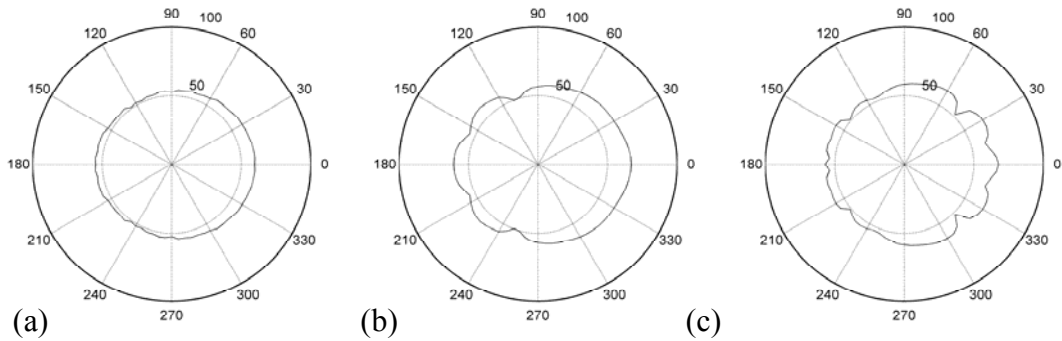
Figure 2.11. Dome #2: a hemispherical dome. (a) 300 Hz. (b) 800 Hz. (c) 1500 Hz.
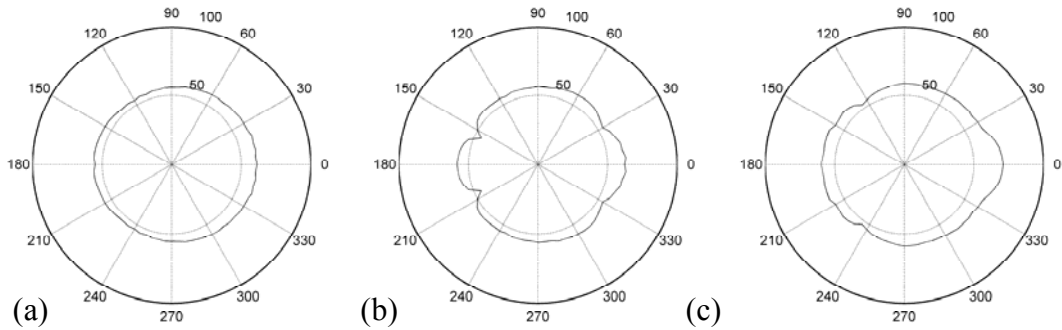
Figure 2.12. Dome #3: a parabolic dome. (a) 300 Hz. (b) 800 Hz. (c) 1500 Hz.

Domes such as these have several advantages. First and foremost, they employ a single driver in most cases. The plastic or acrylic domes are very lightweight and are easily molded. Both of these attributes contribute in keeping the cost relatively low.

The domes also have significant disadvantages. The concept of a reflective device assumes that most or all of the acoustic energy radiated by the loudspeaker is actually hitting the reflector. This is essentially true at high frequencies. However, at low frequencies, the loudspeakers become more omnidirectional. Sound is therefore not directed where it was intended to be, directional control is reduced, and sound then spills

14

to adjacent listening areas. As the loudspeaker excites the dome, it too becomes an omnidirectional source at these low frequencies (i.e. when the dome becomes small compared to wavelength). As can be seen by the measurements above, the domes are consistently omnidirectional at 300 Hz, while they perform well at mid and high frequencies.

2.2 Cardioid Loudspeakers

Another simple directional device is the cardioid loudspeaker. A typical cardioid polar response is shown in Fig. 2.13.
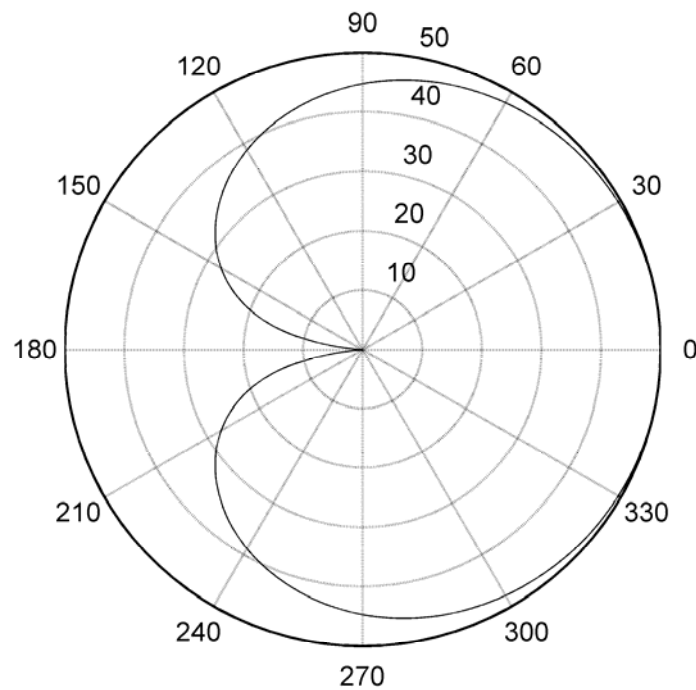
Figure 2.13. Cardioid polar response at 500 Hz.

This response can be achieved by using two loudspeakers spaced close together relative to the wavelength of interest [8], as shown in the diagram in Fig. 2.14. The

polarity of one of the drivers is reversed and delayed proportional to the spacing of the loudspeakers. The required delay is given by,

$$\tau = \frac{L}{c},$$ (2.1)

where L is the spacing between the loudspeakers and c is the speed of sound.
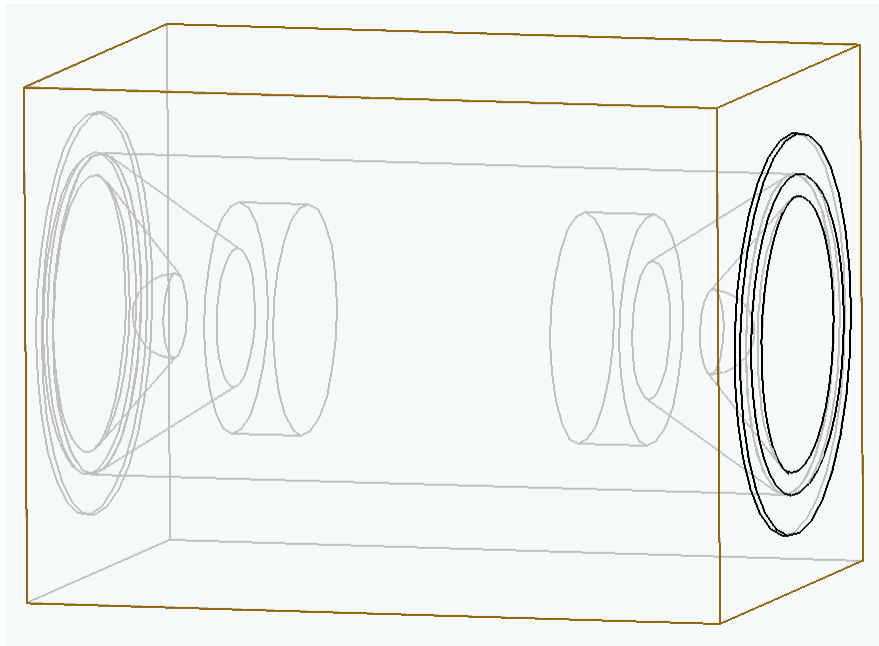
Figure 2.14. Cardioid loudspeaker diagram.

There are two main problems with this design. First, it lacks the capability to be adapted very well to a variety of applications. The only variables are the delay and the spacing between the loudspeakers. Correct calculation of these variables can give the cardioid pattern at any frequency, but once set the beam pattern is not independent of frequency. There is still a large null in the rear for frequencies below that for which the parameters were set, but at higher frequencies the pattern begins to take on the form of a dipole. Second, there is a definite lack of a narrow main lobe. While it is true that a

16

cardioid response is much better than the omnidirectional response exhibited by the domes, the beamwidth is still much too broad for our application.

2.3   Linear and Planar Arrays

Linear and planar arrays are also very common devices used to control the directivity of radiation.   Arrays of in-phase and equivalent amplitude loudspeakers naturally exhibit a directional radiation pattern due to the basic physical principles of constructive and deconstructive interference.   Examples of these resulting radiation patterns will be shown in this chapter.   When DSP is applied to weight the signals feeding the drivers in the arrays, the ability to electronically optimize their directivity control is available, but it increases the overall cost. These arrays can be very directional in the high and mid frequency ranges, but the amount of control achieved at lower frequencies is limited by the size of the array.

In order to keep the cost of the device low, this project only considered passively controlled arrays as a possibility. When passive components, such as common resistors, are used to vary the amplitude of each element in an array, the result is called amplitude shading. It is well known that the common windowing functions used in Fourier analysis (such as rectangular, Hamming, and Blackman windows) can be used to model the effect that amplitude shading has on the far-field radiation pattern for a given array due to the space-time duality [9].   Figure 2.15 shows three windowing functions that are very common in Fourier analysis.
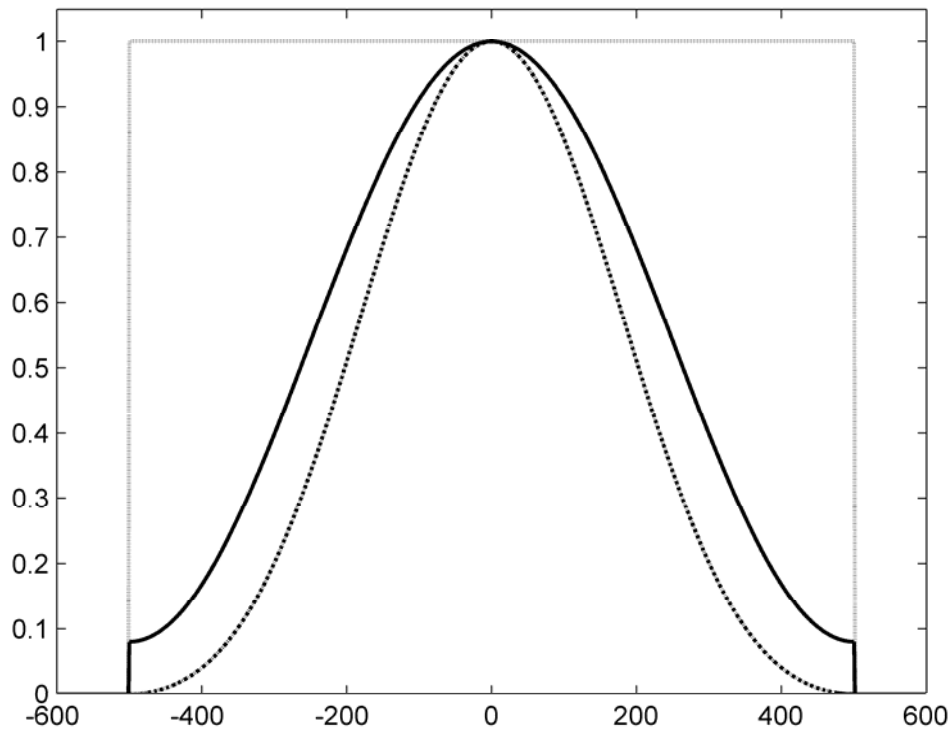
Figure 2.15. Common windowing functions. Rectangular window (dashed trace), Hamming window, (solid trace), and the Blackman window (dot-dash trace).

Applying these function values to the amplitudes of corresponding elements in an array will result in radiation patterns like those in Figs. 2.16 and 2.17. These figures show four examples of amplitude shading on a 2 meter line array of nine elements for two frequencies (Fig. 2.16 is computed at 500 Hz and Fig. 2.17 is computed at 1 kHz). In these plots, the vertical axis of the array results in horizontal main lobes along a line normal to the axis.
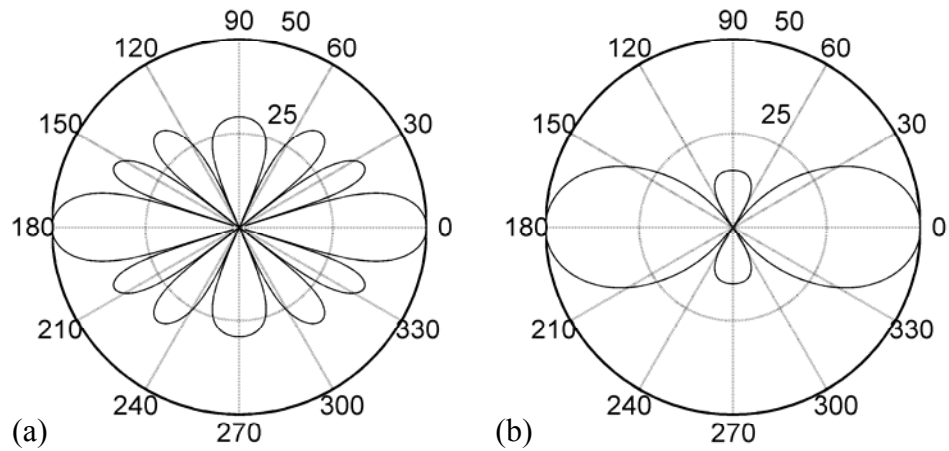
Figure 2.16. Effect of amplitude shading arrays at 500 Hz. (a) Rectangular window shading. (b) Hamming window shading.
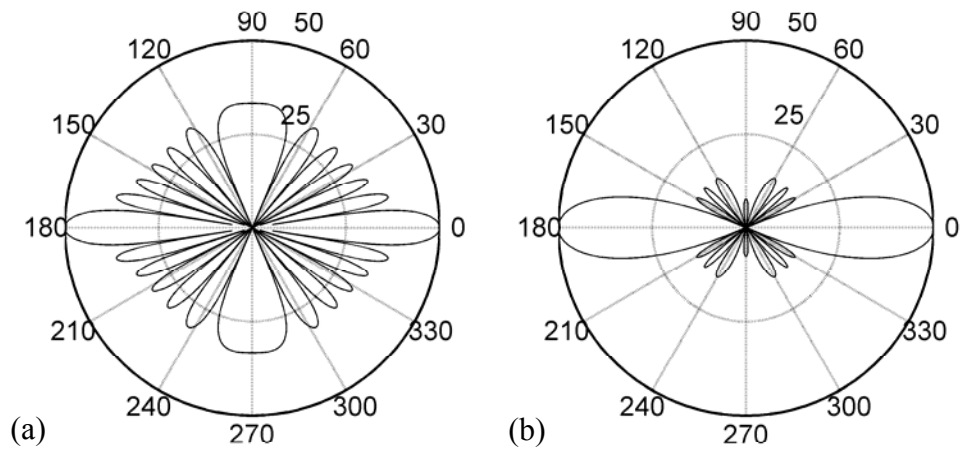
Figure 2.17. Effect of amplitude shading arrays at 1000 Hz. (a) Rectangular window shading. (b) Hamming window shading.

These figures demonstrate one of the main disadvantages of using a linear array. In order to get a reasonable amount of control in the low frequency region, the array must have considerable size. Figure 2.18 shows the same array configuration used in the previous two figures with the Hamming windowing function applied, but the length has

been increased from two to four meters. Here, a drastic narrowing of the main lobe is obvious when compared to Fig. 2.16 and is remarkably similar to Fig. 2.17. This is again due to the space-time duality where a doubling in frequency behaves in the same manner as a doubling in the length of the array [9].
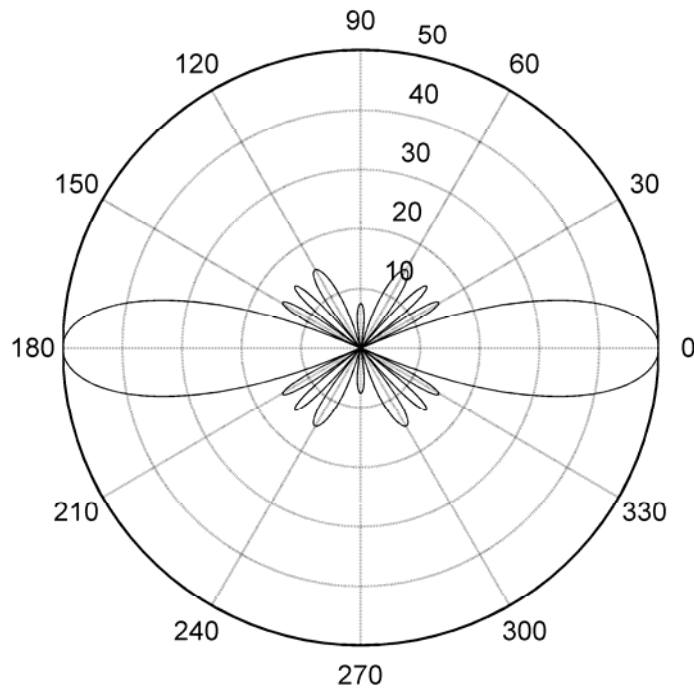
Figure 2.18. Hamming window shading with an array length of 4 meters for 500 Hz.

There are several other disadvantages of using linear arrays. First, there is a large trade-off when using different windowing functions between the width of the main lobe and the level of the side lobes. This is very clear in Figs. 2.16 and 2.17 where a narrower main lobe can be seen when the rectangular windowing function is used, as opposed to the Hamming window. The cost of this narrower main lobe manifests itself in the level of the side lobes which are approximately 20 dB higher for the Rectangular window

result than in the Hamming window result. This phenomenon is well understood [9] and was an expected outcome of these models.

A second disadvantage is that each element in the array is another loudspeaker. The more elements employed in the array, the more expensive the device becomes. Given that one of the goals for this project was to ensure that cost would not be out of reach for common commercial use, this design was not chosen as our prototype. Furthermore, this is the reason we did not look any further into planar arrays, where 20 or more individual loudspeakers could possibly be needed, rendering such devices very unrealistic for our goals.

Finally, linear arrays cannot distinguish between the front and back of the array. In Fig. 2.18 it is clear that the response is symmetric about the axis of the array. If many of these devices were positioned over areas where isolation of sound from one area to the next was desired, an equal amount of energy would be directed toward the ceiling of the room as towards the listeners. The sound could therefore be reflected back into the surrounding areas. While the level of the reflected sound may be much lower than the direct sound, this phenomenon is still undesirable.

2.4   End-fire Arrays

An end-fire array is simply a linear array where a delay has been introduced between each element of the array [8]. As the delay between sources increases (within bounds), the beam is increasingly steered in the direction of the delay. When the delay is equal to the time it takes for the sound to travel from one element to the next, as defined

in Eq. (2.1), the array becomes an end-fire array; the sound is then beamed along the axis of the array.

The next three figures were created to show the effect these time delays have on the radiated sound field for an array of point sources. Figure 2.19 shows a plot of the sound field around an array of nine point sources with no delay applied to any single element. This was calculated by assuming each element in the array was a point source, or monopole. Spherical spreading was assumed and the complex pressure field calculated for each source. The principle of superposition was then used to sum together the contributions from each source and finally plotting the pressure magnitude over the field.
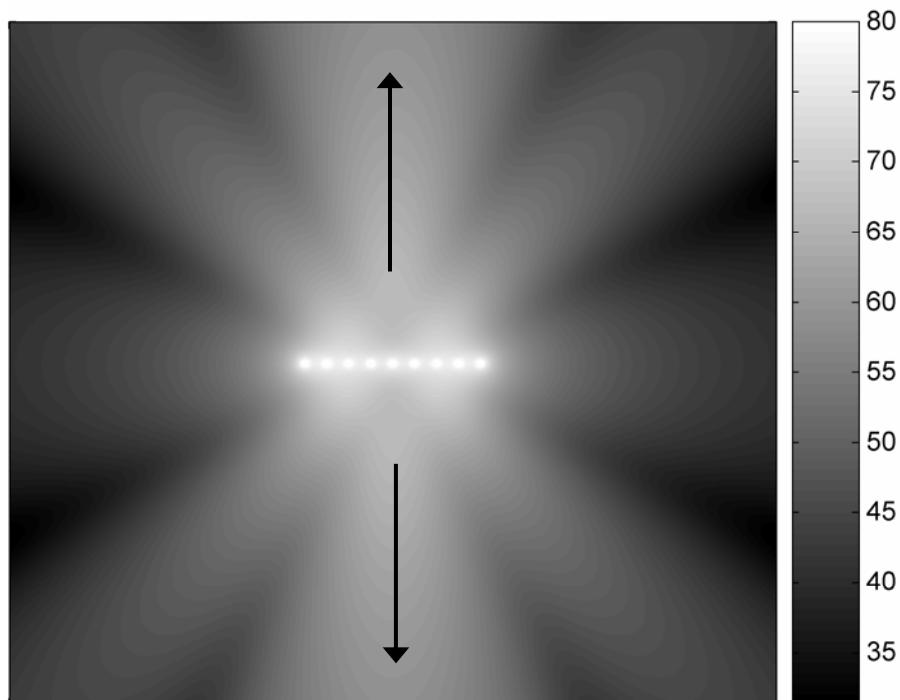
Figure 2.19. Sound field for a nine element array with $\tau = 0$. Arrows show the direction of main lobes.

It is clear that the main lobes are normal to the axis of the array (running from left to right), as shown by the arrows, as was seen in the plots for the line array previously. Note that the axes of these arrays are rotated 90 degrees from those seen in Figs. 2.16 and 2.17.

Figure 2.20 is a plot of the sound field around the same array, but now a delay of $\tau = \dfrac{L}{2c}$ has been applied between each consecutive element. This results in two beams that have been steered to approximately 60 degrees from the normal as indicated by the arrows.
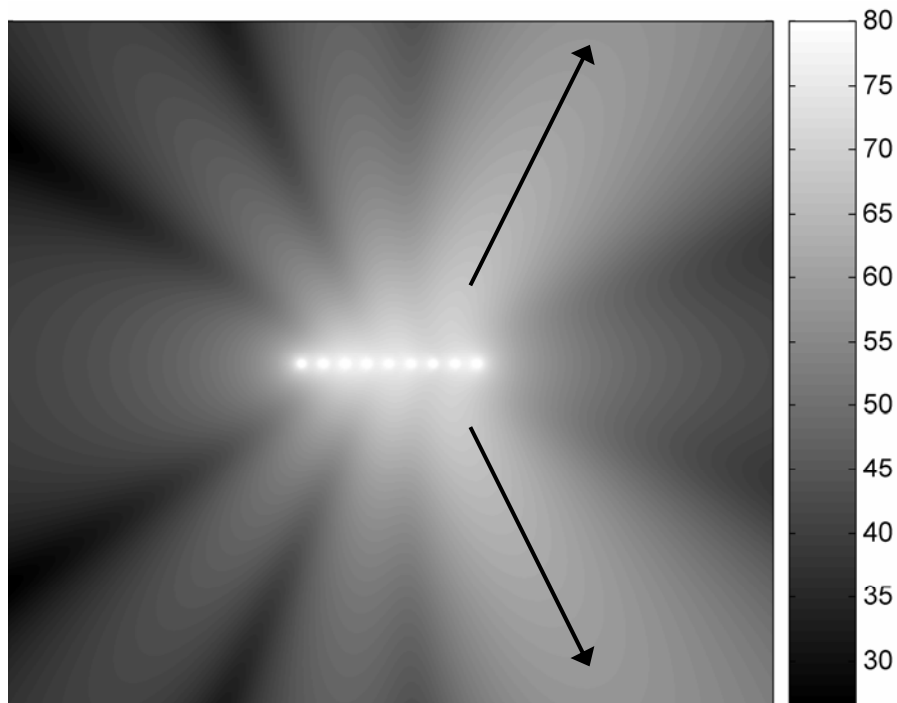
Figure 2.20. Sound field for a nine element array with $\tau = L/(2c)$.

Finally, Fig. 2.21 is a plot of the sound field around the same array wherein the delay has been increased to $\dfrac{L}{c}$. This clearly shows a main lobe along the axis of the array pointing in the direction of the delay.
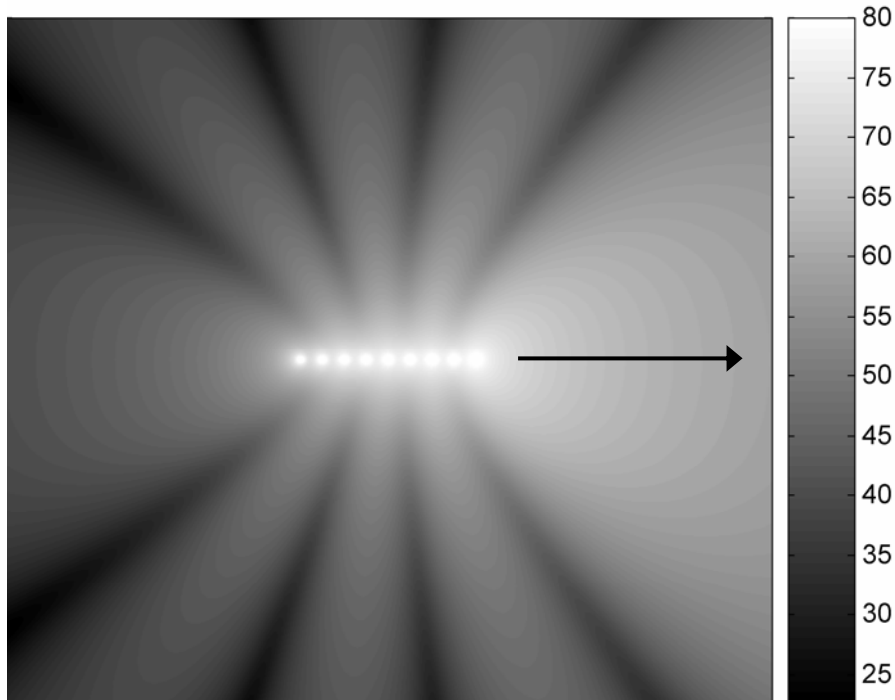
Figure 2.21. Sound field for a nine element array with $\tau = L/c$.

Kinsler and Frey derived a simple equation for the polar response of an array of N elements spaced d apart [10]. The result can be expressed as,

$$H(\theta) = \left| \frac{\sin\left[\left(\dfrac{Nkd}{2}\right)\sin(\theta)\right]}{N\sin\left[\left(\dfrac{kd}{2}\right)\sin(\theta)\right]} \right| \qquad (2.2)$$

where θ is the angle measured from the normal to the array axis. If delays are applied to the elements to steer the main front beam to an angle other than $\theta = 0$, the equation becomes,

$$H(\theta) = \frac{\left| \sin\left[\left(\frac{Nkd}{2}\right)(\sin(\theta) - \sin(\theta_0))\right] \right|}{\left| N \sin\left[\left(\frac{kd}{2}\right)(\sin(\theta) - \sin(\theta_0))\right] \right|} \tag{2.3}$$

where θ_o is the direction the main lobe is to be steered.. Using Eq. (2.3), the polar response in Fig. 2.22 can be calculated at 500 Hz.
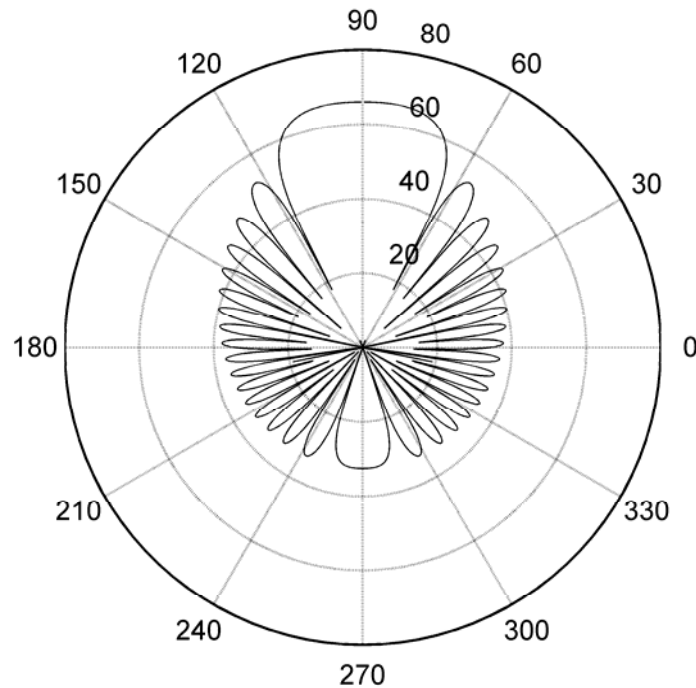
Figure 2.22. End-fire array polar response at 500 Hz.

While the end-fire array has the disadvantage of requiring multiple drivers as do linear and planar arrays, it has a significant advantage over these conventional arrays.

Adding the delay between neighboring elements not only allows the beam of sound to be steered away from the normal direction to the array, but when the beam is aimed along the axis (to create the end-fire condition), the rear lobe is drastically reduced. In Fig. 2.18, it is clear that an amplitude shaded linear array does not have the ability to distinguish between the front and back of the array, as we have already seen. However, the end-fire array shown in Fig. 2.22 demonstrates the reduction of the rear lobe of approximately 25 dB relative to the front lobe. This made the end-fire array a very good choice for our design. However, the hurdle was the fact that multiple drivers are required to achieve the end-fire condition.

Through searching related literature, it was found that shotgun microphones attain the end-fire directivity in their pick-up pattern through a passive approach which only requires a single receiver. In the analogous case of a shotgun loudspeaker, only one driver would be required. This concept led to a deeper investigation into shotgun microphone theory and the idea of a shotgun loudspeaker.

CHAPTER 3

SHOTGUN MICROPHONE AND LOUDSPEAKER THEORY

In order to successfully convert the design of a shotgun microphone into a shotgun loudspeaker, a good understanding of the theory behind the shotgun microphone is needed. This chapter consequently begins with a thorough description of shotgun microphone theory. It then applies these concepts to a shotgun loudspeaker.

3.1 Shotgun Microphones

A typical shotgun microphone is simply a plane-wave tube with holes along its axis, where acoustic waves are allowed to enter the tube, and rigid terminations on both ends of the tube. Once inside the tube, the pressure wave created at each hole interacts with the sound field created by adjacent holes in a way that creates a directional response. A simple diagram of a shotgun microphone is shown in Fig. 3.1.
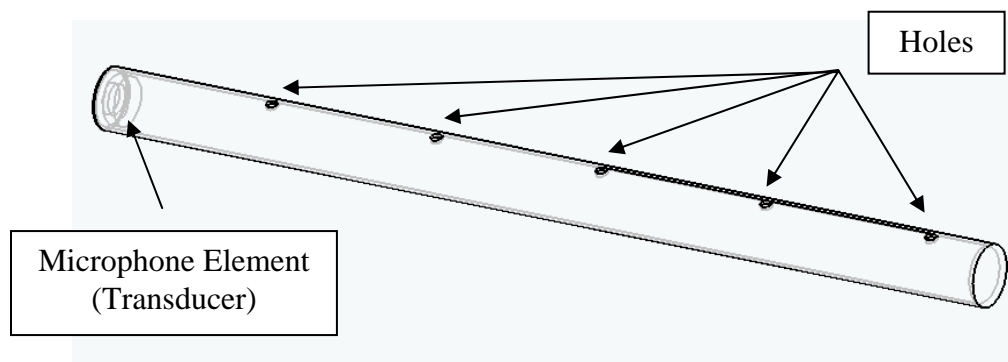
Figure 3.1. Typical shotgun microphone.

In order to investigate the behavior of the shotgun microphone, we first assume a point source is in the far-field of the microphone. Figure 3.2 shows the geometry used in this section.
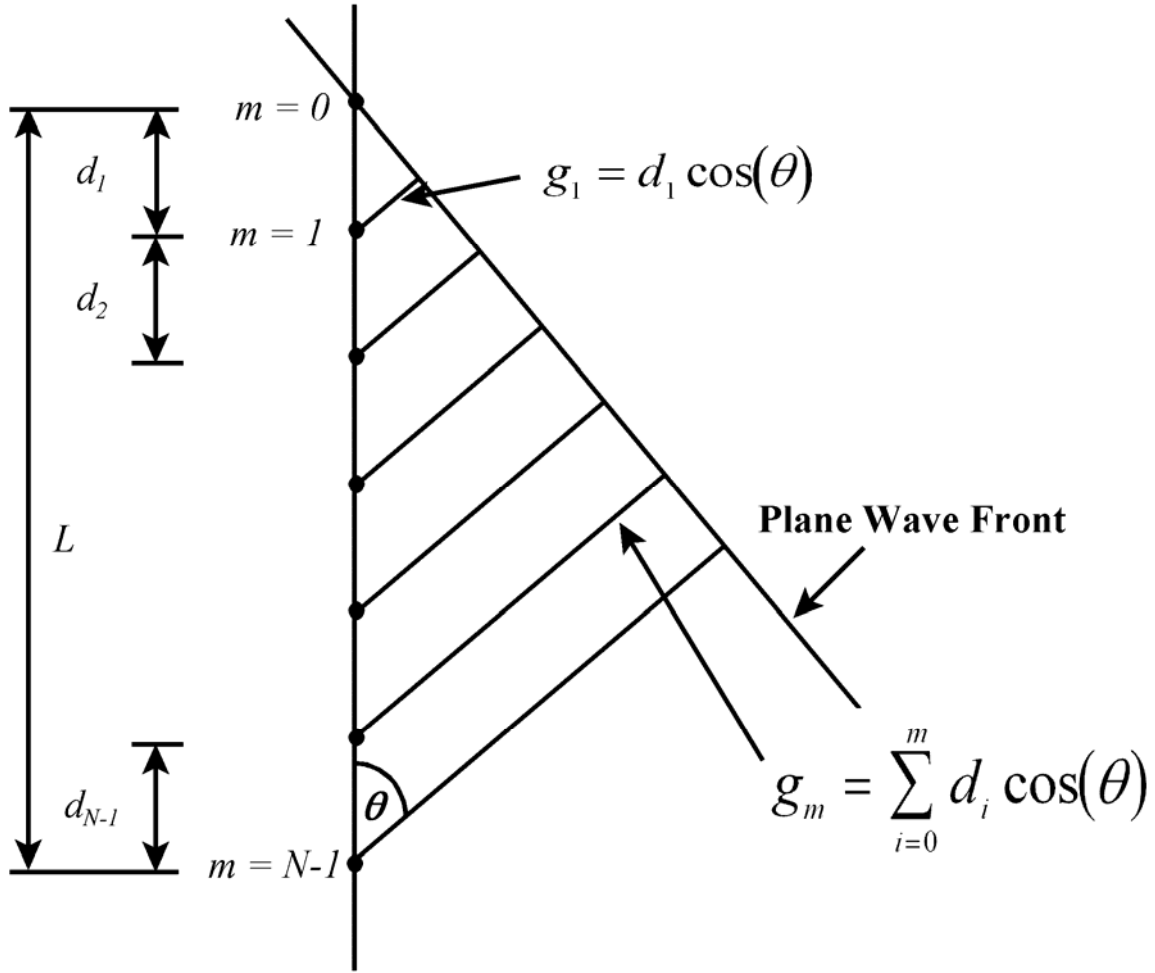
Figure 3.2. Shotgun microphone geometry.

We can write a simple expression for the complex pressure amplitude as

$$\hat{p}_0 = \frac{\hat{A}}{r} e^{-jkr} \tag{3.1}$$

where $\hat{A}$ is the complex monopole amplitude, r is the large distance of propagation from the source, and k is the wave number. If we assume that the magnitude $\left|\hat{p}_0\right|$ is

28

approximately equal for all holes in the tube (i.e. the wave fronts are locally planer), we can simply compensate for the additional distance traveled and propagation time delay by the wave front to get to successive holes. The additional distance for the mth hole can be given as

$$g_m = \left[\sum_{i=0}^{m} d_i\right] \cos(\theta), \tag{3.2}$$

where θ is the angle of arrival for the wave front with respect to the axis of the tube and d_i is the spacing between the holes [11]. The propagation delay for the mth hole is then

$$\tau_m = \frac{g_m}{c}, \tag{3.3}$$

the phase shift for a given frequency ω is

$$\phi_m = \omega \tau_m, \tag{3.4}$$

and the pressure phase factor becomes

$$e^{-jkg_m}. \tag{3.5}$$

This accounts for the phase difference between the wave front reaching the first hole and that reaching the mth hole. Given the phase shift, the pressure at each hole is written as

$$\hat{p}_m(\omega,\theta) \approx \hat{p}_0 e^{-jkg_m}. \tag{3.6}$$

Once the wave has entered the tube, a second delay needs to be accounted for as the excited plane wave travels from the hole to the end of the tube, ultimately arriving at the microphone element. We thus employ another phase factor

$$e^{-jka_{mi}} \tag{3.7}$$

where a_{mi} is defined for the mth hole by

$$a_{mi} = L - \sum_{i=0}^{m} d_i. \tag{3.8}$$

29

L is the length of the tube and d_i is the spacing between neighboring holes. The pressure from each hole arriving at the microphone element is then

$$\hat{p}_0 e^{-jkg_m} e^{-jka_{mi}} \tag{3.9}$$

and the total pressure $\hat{p}_T$ from all holes seen by the microphone element is

$$\hat{p}_T(\omega,\theta) = \sum_{m=0}^{N-1} \hat{p}_0 e^{-jk(a_{mi}+g_m)} \tag{3.10}$$

After substituting Eqs. (3.2) and (3.8) into Eq. (3.10), we then obtain

$$\hat{p}_T(\omega,\theta) = \hat{p}_0 \sum_{m=0}^{N-1} e^{-jk\left[\left(L-\sum_{i=0}^{m} d_i\right) + \sum_{i=0}^{m} d_i \cos(\theta)\right]}. \tag{3.11}$$

This then simplifies to

$$\hat{p}_T(\omega,\theta) = \hat{p}_0 e^{-jkL} \sum_{m=0}^{N-1} e^{-jk[\cos(\theta)-1]\sum_{i=0}^{m} d_i} \tag{3.12}$$

which is in a generalized form for a non-uniform hole spacing. If the spacing between adjacent holes is assumed to be equal along the length of the tube, Eq. (3.12) reduces to

$$\hat{p}_T(\omega,\theta) = \hat{p}_0 e^{-jkL} \sum_{m=0}^{N-1} e^{-jkmd[\cos(\theta)-1]} \tag{3.13}$$

where d is the hole spacing. The normalized directivity function of a system is defined as

$$D(\omega,\theta) = \frac{P_T(\omega,\theta)}{P_{T,\max}(\omega,\theta)}, \tag{3.14}$$

which has a maximum value at $\theta = 0°$ for a shotgun microphone configuration, as opposed to $\theta = 90°$ for a similarly oriented broadside linear array described previously in Chapter 2. Another useful measure of the directivity is the beam pattern which is given by,

$$B(\omega,\theta) = 20\log[D(\omega,\theta)]. \tag{3.15}$$

The two plots in Fig. 3.3 show the beam patterns for a model of a shotgun microphone using Eqs. (3.13), (3.14) and (3.15). This model has 15 holes spaced 1 cm apart from each other and is computed for both 5 kHz and 10 kHz.
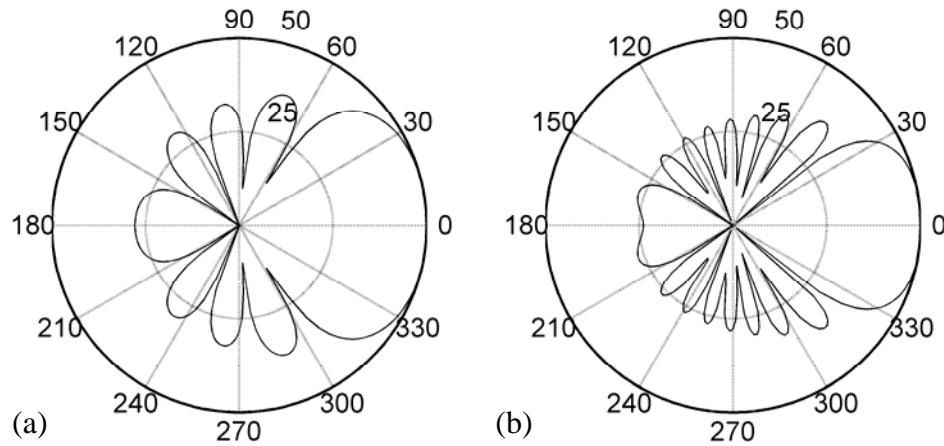
Figure 3.3. Shotgun microphone beam patterns. (a) 5 kHz. (b) 10 kHz.

As discussed earlier, one of the drawbacks of the end-fire array was the requirement of multiple transducers in the design, which increases the manufacturing and maintenance costs. The shotgun microphone achieves the directional behavior of an end-fire array of microphones, but with only a single microphone at the end of a long tube with carefully placed holes. Each hole essentially acts as an individual receiver in the array. The summation of the pressures seen by the holes is done inside the tube by way of the superposition principle as they reach the microphone.

This implies that a shotgun loudspeaker might be constructed using only a single loudspeaker at the end of a tube with holes along the axis to act as radiating elements in an array. It decreases the number of required loudspeakers and cost of the device, and

allows a designer to adjust the length and number of holes in the tube for specific applications.

3.2   Shotgun Loudspeakers

The basic design of the shotgun loudspeaker is quite simple. Figure 3.4 shows a diagram of the device. A single loudspeaker is mounted in a sealed box that has been somewhat optimized over the audio bandwidth for a flat far-field frequency response for the particular driver being used. An exact optimization of the volume required in the enclosure for a given driver is difficult because the loading on the loudspeaker cone is much different once the loudspeaker is mounted to the tube, as opposed to radiating into free space. The box must be sealed to ensure that all the energy is being delivered down the tube and not out a port external to the tube. An external port would create undesirable interference effects and likely degrade the directivity performance of the device.
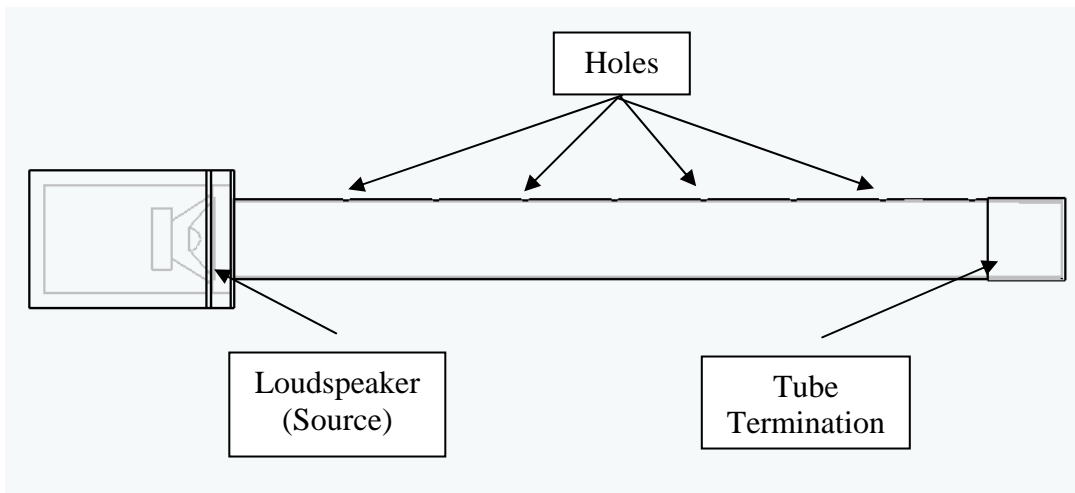
Figure 3.4. Typical shotgun loudspeaker diagram.

As the wave fronts travel down the tube from the loudspeaker and encounter each hole, a discrete source is created that radiates into the far-field acoustic space. As seen in Chapter 2, if the delay between elements is given by

$$\tau = \frac{d}{c}$$
(3.16)

where τ is the delay, d is the spacing between the elements of the array, and c is the speed of sound, then the resulting radiation pattern will be focused in the direction of the delay or, in our case, along the axis of the tube. The delay d/c is exactly equal to the time it takes a sound wave to propagate a distance d. Therefore, this passive setup will result in an end-fire configuration.

The number of holes, radius of the holes and tube, and the acoustic properties of the termination all have an effect on the polar response of the shotgun loudspeaker. Reflections from both the tube termination and the impedance discontinuities at each hole complicate the model and change the radiated pressure at each hole. These phenomena, and their effects on the performance of the device, are all discussed in detail in the next chapter, where the analytical model is described.

3.3   Model Assumptions

Some basic assumptions used in developing a detailed analytical model for this shotgun loudspeaker require mention previous to that discussion. First, only plane wave propagation is assumed to exist inside the tube.   In practice, this limits the useful frequency range (related to the radius of the tube) when making measurements of the prototypes. The smaller the radius, the higher the cutoff frequency beyond which the

physical model breaks down. The actual calculation for the cutoff frequency will be discussed in Chapter 5.

Second, radiated field measurement points are assumed to be in the geometric and acoustic far field relative to the shotgun loudspeaker. Third, we assume that the wave amplitudes are small enough to use linear theory. Finally, our initial model assumes that there is no external coupling between holes of the tube to simplify the model. In Chapter 7, the coupling between holes is considered and the far-field effects are discussed.

CHAPTER 4

PRELIMINARY ANALYTICAL MODEL

An analytical model of the shotgun loudspeaker is required to predict the volume velocity generated at each hole, calculate the associated sound pressure radiated from each hole, and superpose the outputs in the far field to find the polar response of the array. The directivity of a given configuration can then be predicted and explained. This chapter presents an initial idealized model of a shotgun loudspeaker that provides several insights into its general behavior. Refinements to the model will be presented in Chapter 7.

4.1 Equivalent Circuits

Of the many approaches to modeling acoustic phenomena, one of the most common techniques for lumped-element and one-dimensional systems involves equivalent circuits. Proven circuit analysis methods are used to formulate equations of motion and derive physical quantities of interest (e.g., volume velocity or pressure) [12]. As is true of any method, equivalent circuit analysis has its advantages and disadvantages. Many common physical systems (e.g., transducers) require that multiple domains (such as acoustical, electrical, or mechanical) be represented in a single circuit to adequately describe the entire system. These circuits have the ability to represent all elements of the various domains in a single circuit by way of coupling elements (e.g., transformers and gyrators). Another advantage of this method is that many circuits can be drawn quite easily by simple inspection of the physical systems.

Equivalent circuit analysis has drawbacks as well. For many elements, only a low-frequency approximation to the system is valid where the dimensions involved are small relative to the acoustic wavelength [13]. Wave effects are also ignored in individual lumped elements. This requires great care in interpreting the solutions to the circuit.

The accuracy of the equations of motion derived from equivalent circuits is limited by the accuracy with which the lumped elements of the circuits correctly describe the physical phenomena. For example, the impedance of a volume of air can be modeled as a capacitor in the acoustic impedance domain, where the wavelengths of interest are many times longer than any single dimension of the cavity. However, once the wavelengths are comparable to the dimensions of the cavity, this approximation is no longer valid. Commercially available software packages implementing finite element or boundary element methods are often needed to accurately describe the acoustic fields for higher frequencies in devices with arbitrary geometries.

4.2   Waveguides

Another inadequacy of common lumped-element circuits is their inability to represent dynamic changes in boundary conditions. However, these can be modeled in one-dimensional systems by way of "waveguide circuits," which take into account cross-sectional variations. They also serve as a means to translate impedances from one end of a tube to another (as seen in Fig. 4.1), in the same manner as the lossless impedance translation theorem given by:

$$Z_{AI} = \left(\frac{\rho_0 c}{S}\right) \frac{Z_{AT} + j\left(\frac{\rho_0 c}{S}\right)\tan(kL)}{\frac{\rho_0 c}{S} + jZ_{AT}\tan(kL)} \tag{4.1}$$

where Z_{AT} is the termination acoustic impedance to be translated a distance L down a tube of cross-sectional area S, k is the acoustic wave number, ρ_0 is the density of air, and c is the speed of sound [10].
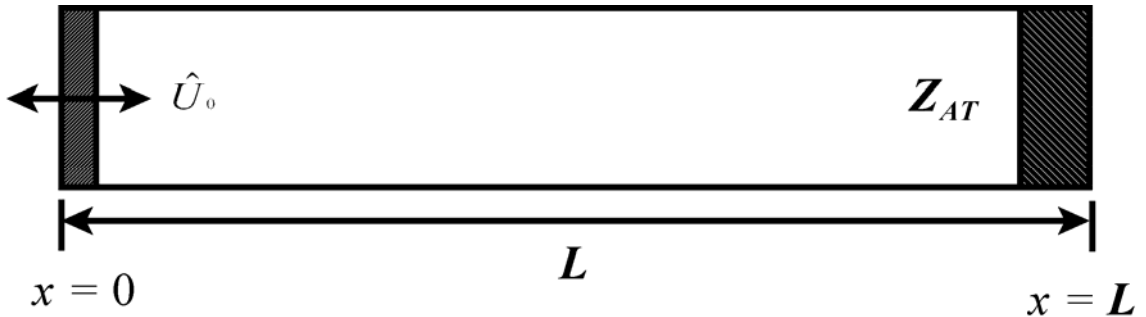
Figure 4.1. Diagram of a one-dimensional tube terminated by an acoustic impedance Z_{AT}.

Waveguide circuits also allow for a more accurate representation of the sound field *within* a one-dimensional acoustic space. They are not limited to extremely low frequencies and can account for many axial resonances of a tube. The circuit in Fig. 4.2 accurately models the sound field at the source and termination positions of the system described above for frequencies below the cutoff frequency of the first tube cross mode. This circuit is commonly known as a "T-network" and can be used to model one-dimensional waves in a tube with an arbitrary termination [12].
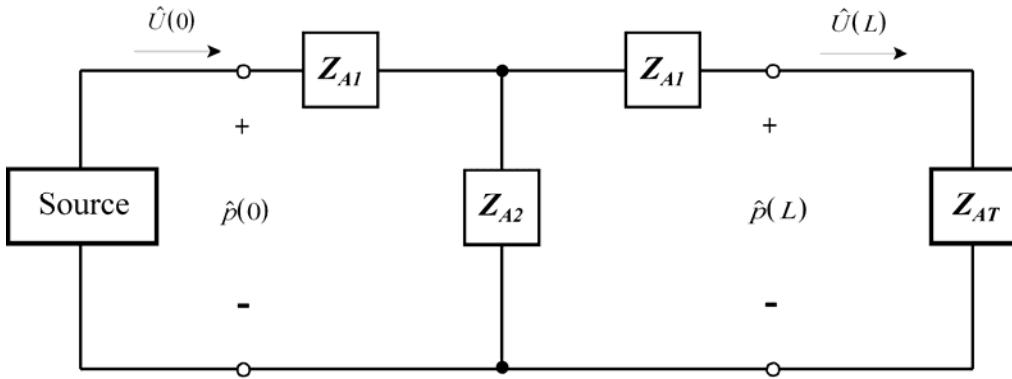
Figure 4.2. Acoustic impedance circuit for a one-dimensional waveguide with an arbitrary source at one end and an arbitrary termination at the other.

In order to get values for Z_{A1} and Z_{A2}, we first solve for the acoustic input impedance Z_{AI} of the circuit. This is expressed as

$$Z_{AI} = Z_{A1} + \cfrac{1}{\cfrac{1}{Z_{A2}} + \cfrac{1}{Z_{A1} + Z_{AT}}}, \qquad (4.2)$$

where Z_{AT} is the acoustic termination impedance. With some simplification and rearranging of terms, we can express Z_{AI} as

$$Z_{AI} = \frac{Z_{A1}^2 + 2Z_{A1}Z_{A2} + Z_{AT}(Z_{A1} + Z_{A2})}{Z_{A1} + Z_{A2} + Z_{AT}}. \qquad (4.3)$$

The impedance translational theorem in Eq. (4.1), gives the acoustic input impedance as

$$Z_{AI} = \left(\frac{\rho_0 c}{S}\right) \frac{Z_{AT} + j\left(\dfrac{\rho_0 c}{S}\right)\tan(kL)}{\dfrac{\rho_0 c}{S} + jZ_{AT}\tan(kL)}. \qquad (4.4)$$

If we make the substitution

$$\gamma = \frac{\rho_0 c}{S} \tag{4.5}$$

into Eq. (4.4) and divide the numerator and denominator by $\left[j \tan(kl) \right]$, it then becomes

$$Z_{AI} = \gamma \left[\frac{\gamma - j Z_{AT} \cot(kL)}{Z_{AT} - j\gamma \cot(kL)} \right]. \tag{4.6}$$

We can now use the identity

$$\csc^2(x) - \cot^2(x) = 1 \tag{4.7}$$

and rearrange terms to get the expression

$$Z_{AI} = \gamma \left\{ \frac{\gamma \left[\csc^2(kL) - \cot^2(kL) \right] - j Z_{AT} \cot(kL)}{Z_{AT} - j\gamma \cot(kL)} \right\}. \tag{4.8}$$

Next, we use a second identity

$$\tan\left(\frac{x}{2} \right) = \csc(x) - \cot(x) \tag{4.9}$$

and rearrange terms again to get a final expression for Z_{AI}.

$$Z_{AI} = \frac{\left[j\gamma \tan\left(\frac{kL}{2} \right) \right]^2 + 2\left[j \tan\left(\frac{kL}{2} \right) \right]\left[-j\gamma \csc(kL) \right] + Z_{AT}\left[j\gamma \tan\left(\frac{kL}{2} \right) - j\gamma \csc(kL) \right]}{Z_{AT} + j\gamma \tan\left(\frac{kL}{2} \right) - j\gamma \csc(kL)} \tag{4.10}$$

If we resubstitute for γ and compare Eq. (4.3) to Eq. (4.10), we find that

$$Z_{A1} = j\left(\frac{\rho_0 c}{S} \right) \tan\left(\frac{kL}{2} \right) \tag{4.11}$$

$$Z_{A2} = -j\left(\frac{\rho_0 c}{S} \right) \csc(kL). \tag{4.12}$$

While a single T-network can offer valuable information at the input or termination, inspection of the sound field at points away from the ends of the tube cannot

be extracted without a modification to the circuit. Two successive waveguide circuits can

be coupled together, as shown in Fig. 4.3, to provide the spatially dependant acoustic

field quantities at inner points. In the diagram, x is the axial position of interest and L is

the length of the tube.
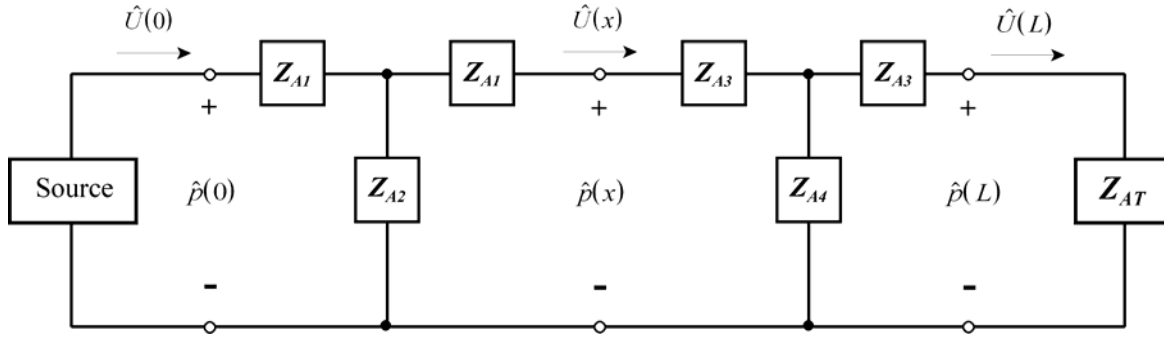
Figure 4.3. Acoustic impedance circuit for a one-dimensional waveguide with an arbitrary source at one end and an arbitrary termination at the other. The circuit permits inspection of acoustic field quantities at any arbitrary field position x inside the tube.

Here Z_{A1}, Z_{A2}, Z_{A3}, and Z_{A4} are defined as

$$Z_{A1} = j\left(\frac{\rho_0 c}{S}\right)\tan\left(\frac{kx}{2}\right) \tag{4.13}$$

$$Z_{A2} = -j\left(\frac{\rho_0 c}{S}\right)\csc(kx) \tag{4.14}$$

$$Z_{A3} = j\left(\frac{\rho_0 c}{S}\right)\tan\left[\frac{k(L-x)}{2}\right] \tag{4.15}$$

$$Z_{A4} = -j\left(\frac{\rho_0 c}{S}\right)\csc[k(L-x)]. \tag{4.16}$$

At the junction of the two waveguide circuits, the pressure and volume velocity can be calculated as the potential and flow (current), respectively. We will now use these waveguides to model the sections of the shotgun tube between holes to find the volume velocity at each hole.

4.3   Shotgun Tube Circuit

The sound field inside our shotgun tube is modeled by a quasi-ladder network of alternating waveguide circuits and shunted impedance terms for each hole. An example of such a circuit for a tube with two holes is given in Fig. 4.4. This model has four main elements: a source, three waveguide circuits, two hole impedance terms (Z_{AH}), and a termination to the tube (Z_{AT}).
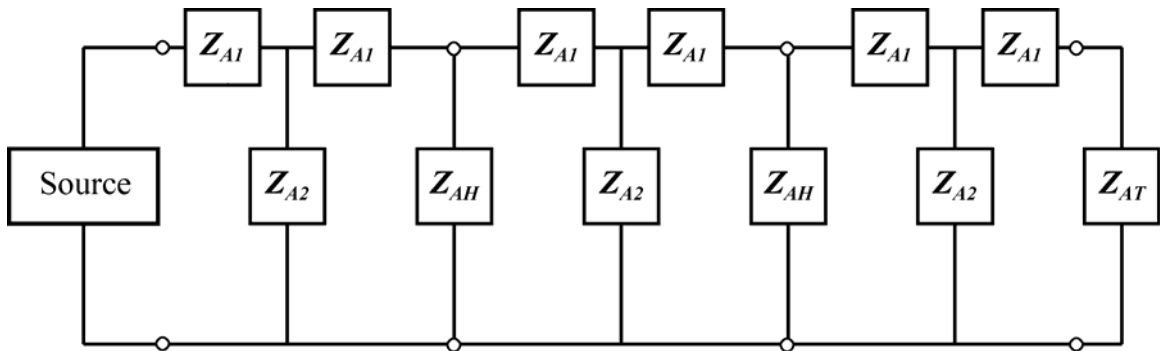
Figure 4.4. Equivalent circuit for a tube with two holes.

4.3.1   Source Models

The source used in the preliminary model is a simple constant volume velocity source with infinite internal impedance. This is a first approximation to a loudspeaker driving the end of the tube. In Chapter 7, we will introduce a more accurate model of the loudspeaker to account for its finite internal impedance.

4.3.2   Hole Impedances

Research into work done on tone holes of musical instruments offered great insight into how such orifices may be modeled [14-17]. A more analytic approach, however, by Ted Carnes was found in a paper on the theory of shotgun microphones [11].

Assuming the volume velocity through each hole is insufficient to require the inclusion of nonlinear terms for the viscous flow resistance, the impedance representation of each hole is simply made up of two parts: the radiation impedance and the impedance of the orifice length.

Simplifications can be made by assuming that $ka << 1$ (where a is the radius of the orifice) and the orifices are mounted in the wall of a tube whose radius of curvature is very large compared to the radius of the orifice itself. Thus, the orifice can be approximated as if it were a piston in an infinite baffle. Using this assumption, we write the radiation impedance (Z_{AR}) as

$$Z_{AR} = \frac{\rho_0 c}{\pi a^2}\left[R(2ka) + jX(2ka)\right], \qquad (4.17)$$

where

$$R(2ka) = 1 - \frac{J_1(2ka)}{ka} \qquad (4.18)$$

$$X(2ka) = \frac{H_1(2ka)}{ka}. \tag{4.19}$$

In these equations, a is the radius of the hole, J_1 is a first-order Bessel function of the first kind, and H_1 is a first-order Struve function. The series expansions for both expressions can be written as

$$R(x) = \frac{x^2}{2 \cdot 4} - \frac{x^4}{2 \cdot 4^2 \cdot 6} + \frac{x^6}{2 \cdot 4^2 \cdot 6^2 \cdot 8} \cdots \tag{4.20}$$

$$X(x) = \frac{4}{\pi}\left[\frac{x}{3} - \frac{x^3}{3^2 \cdot 5} + \frac{x^5}{3^2 \cdot 5^2 \cdot 7} \cdots \right]. \tag{4.21}$$

In the low-frequency approximation ($ka \ll 1$), all but the first term in each series can be neglected. In this case, $R(2ka)$ and $X(2ka)$ reduce to

$$R(2ka) \approx \frac{(2ka)^2}{8} \tag{4.22}$$

$$X(2ka) \approx \frac{8ka}{3\pi}, \tag{4.23}$$

which can be substituted back into Eq. (4.17) to give

$$Z_{AR} \approx \frac{\rho_0 c}{\pi a^2}\left[\frac{(2ka)^2}{8} + j\frac{8ka}{3\pi} \right] = \frac{\rho_0 c k^2}{2\pi} + j\frac{8\rho_0 ck}{3a\pi^2}. \tag{4.24}$$

The impedance of the orifice length (Z_{AO}) was derived by Carnes, who modeled it as a very short section of a tube [11]. His first-order approximation is given by

$$Z_{AO} \approx \frac{(8\mu\rho_0\omega)^{\frac{1}{2}}}{\pi a^2}\left(\frac{t}{2a} \right) + j\frac{\omega\rho_0 t}{\pi a^2} \tag{4.25}$$

where μ is the absolute viscosity and t is the thickness of the tube wall. Adding Z_{AR} and Z_{AO} together yields the total impedance of a hole in the tube wall:

$$Z_{AH} = Z_{AR} + Z_{AO} \approx \left[\frac{\rho_0 c k^2}{2\pi} + \frac{(8\mu\rho_0\omega)^{\frac{1}{2}}}{\pi a^2}\left(\frac{t}{2a}\right) \right] + j\left[\frac{8\rho_0 ck}{3a\pi^2} + \frac{\omega\rho_0 t}{\pi a^2} \right]. \tag{4.26}$$

Seeing that the value of μ is $1.85\text{x}10^{-5}$, we can neglect viscous terms, which will be several orders of magnitude lower than neighboring terms for typical values of t and a. Making this simplification reduces our equation even further. Our final form for the impedance of a hole in our shotgun tube is then given by the equation

$$Z_{AH} \approx \frac{\rho_0 c k^2}{2\pi} + j\frac{\omega\rho_0}{\pi a^2}\left(\frac{8a}{3\pi} + t\right). \tag{4.27}$$

4.3.3 Termination Impedances

Our preliminary model uses three basic tube terminations: anechoic (Z_{ATA}), closed (Z_{ATC}), and open (Z_{ATO}). One further termination possibility is the drone cone (Z_{ATD}) and will be explored later. The expressions for each of these three terminations can be written as,

$$Z_{ATA} = \frac{\rho_0 c}{S} \tag{4.28}$$

$$Z_{ATR} \approx \infty \tag{4.29}$$

$$Z_{ATO} = \frac{\rho_0 c}{S}\left[\frac{(ka)^2}{4} + j(0.61ka) \right]. \tag{4.30}$$

The different terminations have different effects on the performance of the shotgun tube as will be discussed in Chapter 5.

4.4 Circuit Analysis

Once the parameters of each element in the circuit are carefully selected, the input impedance of the tube can be calculated. This is found by beginning at the termination impedance (Z_{AT}) and summing together the individual elements, either in series (Z_S) or in parallel (Z_P), using the rules for summing impedances below.

$$Z_S = Z_1 + Z_2 \qquad (4.31)$$

$$\frac{1}{Z_P} = \frac{1}{Z_1} + \frac{1}{Z_2} . \qquad (4.32)$$

Figure 4.5 provides an example of the normalized input impedance of a tube with a rigid termination and 5 holes, each with a radius of 0.635 cm. This hole radius gives a maximum *ka* value of 0.0233 in the bandwidth of interest (0 to 3 kHz) which satisfies the *ka* << 1 condition placed on our analytical model. The hole spacing is set to 11.85 cm which gives an overall length of approximately 71 cm. The tube wall has a thickness of 0.5 cm and the tube radius is 5.08 cm.

The peaks in Fig. 4.5, with the exception of the first peak which will be explained momentarily, all appear to be evenly spaced. As the plane waves travel down the tube, an impedance discontinuity is encountered at each hole where a portion of the incident wave is reflected back toward the source. This happens at all holes and terminations, which gives rise to resonances between holes or combinations of holes and the termination.

The hole spacing for this model is 11.85 cm which corresponds to a half-wavelength at a frequency of 1447 Hz, where a standing wave can be created between a pair of neighboring holes. This same phenomenon can also occur when the spacing between holes equals any integer multiple of a half-wavelength.
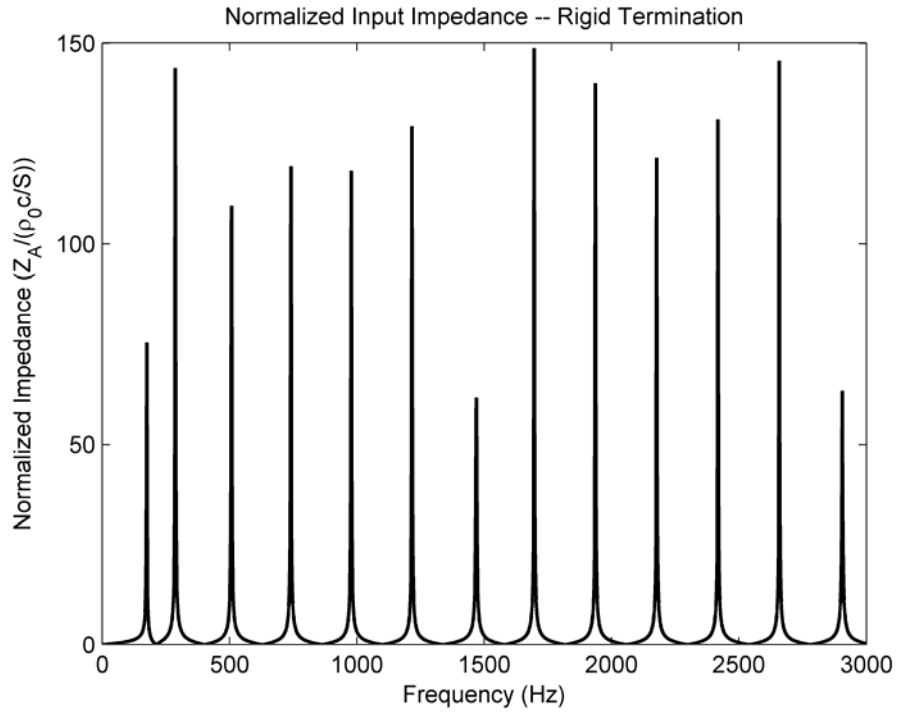
Figure 4.5. Normalized input impedance for a 5.08 cm radius lossless tube, rigid termination, 5 holes, 0.635 cm hole radius, 0.5 cm tube wall thickness, and 11.85 cm hole spacing which gives an overall tube length of 71 cm.
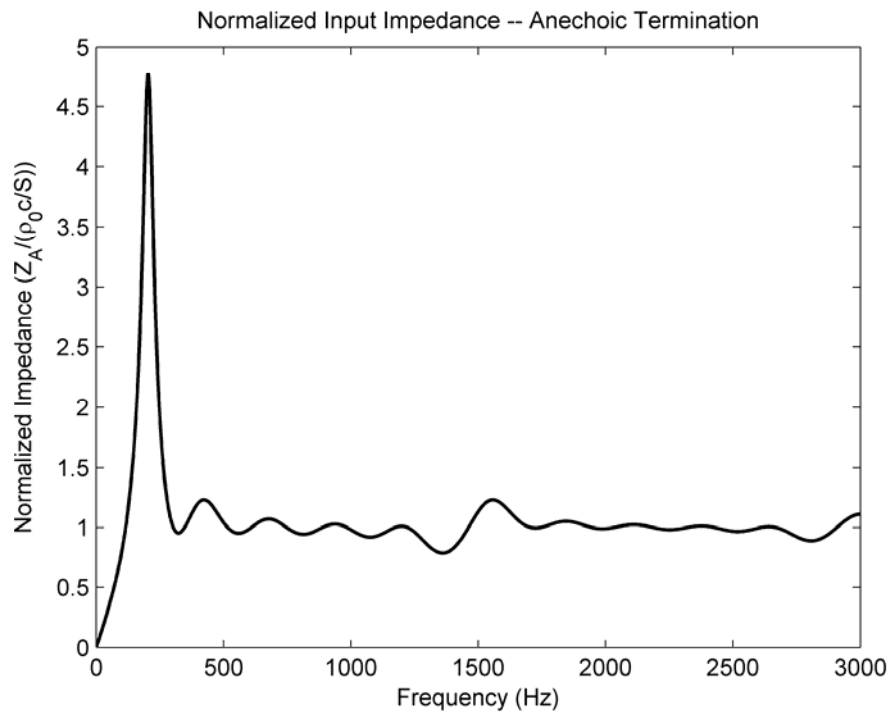
Figure 4.6. Normalized input impedance for a 5.08 cm radius tube, anechoic termination, and 5 holes.

46

A peak at 1447 Hz appears on the graph in addition to its next harmonic, 2894 Hz, which correspond to the 11.85 cm hole spacing. The other peaks are due to resonances arising from interactions between the non-neighboring holes and the termination along the tube length and their respective harmonics.

The first peak was an interesting phenomenon that was not expected initially. This frequency is caused by a Helmholtz resonator effect between the masses of air in the holes and the inner volume of the tube. To examine this anomaly more closely, the same tube model was given an anechoic termination to exaggerate this particular resonance above the others. This occurs because the anechoic termination eliminates any reflected waves from the end of the tube and thereby reduces the amplitude of any standing waves between holes and the termination. Figure 4.6 shows the same tube as in Fig. 4.5 but with an anechoic termination. As is clearly seen in the figure, small undulations still appear in the input impedance due to resonances between holes.

As previously stated, the large resonance in Fig. 4.6 is due to the interaction of the "plug" of air in the hole and small volumes of air in the tube beneath each hole. To investigate this behavior, the masses were varied and the corresponding changes were observed. Figure 4.7 shows the result when the inertance, or mass-like term of the hole impedance, is either increased or decreased by a factor of 10.

As expected, an increase of mass shifts the resonance frequency downward. Not only does it shift the peak down, but it also reduces the amplitude of the resonance with respect to the impedance "floor" which is at a value of 1 on the normalized plot. Therefore, as the mass increases, the acoustic input impedance of the shotgun tube looks

more like a plane wave tube with no holes in it which has a value of $\rho_0 c/S$, or 1 if normalized as in the plot.
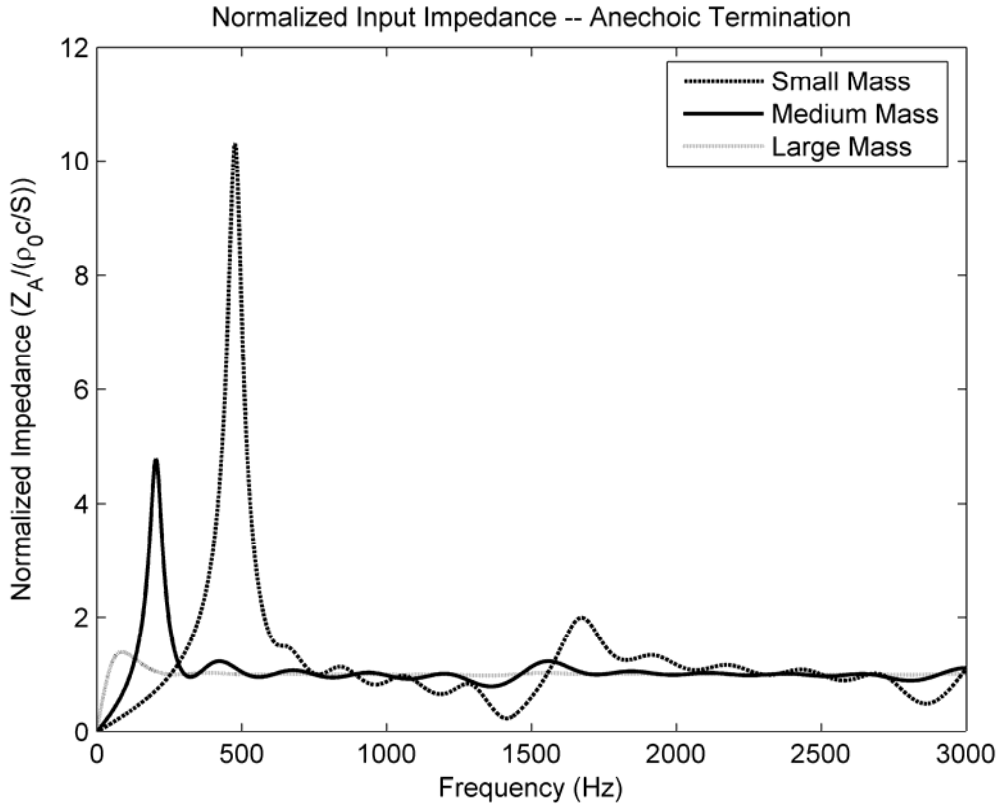
Figure 4.7. Normalized input impedance for a 5.08 cm radius tube with an anechoic termination and 5 holes with varying mass values. The medium mass value is given by the imaginary part in Eq. (4.27). The small mass is 1/10 times the medium mass. The large mass is 10 times the medium mass.

Figure 4.7 also shows that a decrease in the mass shifts the resonance frequency upward. This has a practical limit, though. As the reactance of the hole radiation impedance becomes very small, the shunted hole impedance term in the circuit approaches zero which effectively shorts the circuit at that point. Thus, as the mass of air in the shotgun tube holes decreases, the input impedance can be approximated by a single

48

waveguide circuit with a termination impedance of zero. Figure 4.8 shows this approximation where the solid trace is for a very small mass and the dotted trace is for a single waveguide circuit, terminated with a zero impedance value.
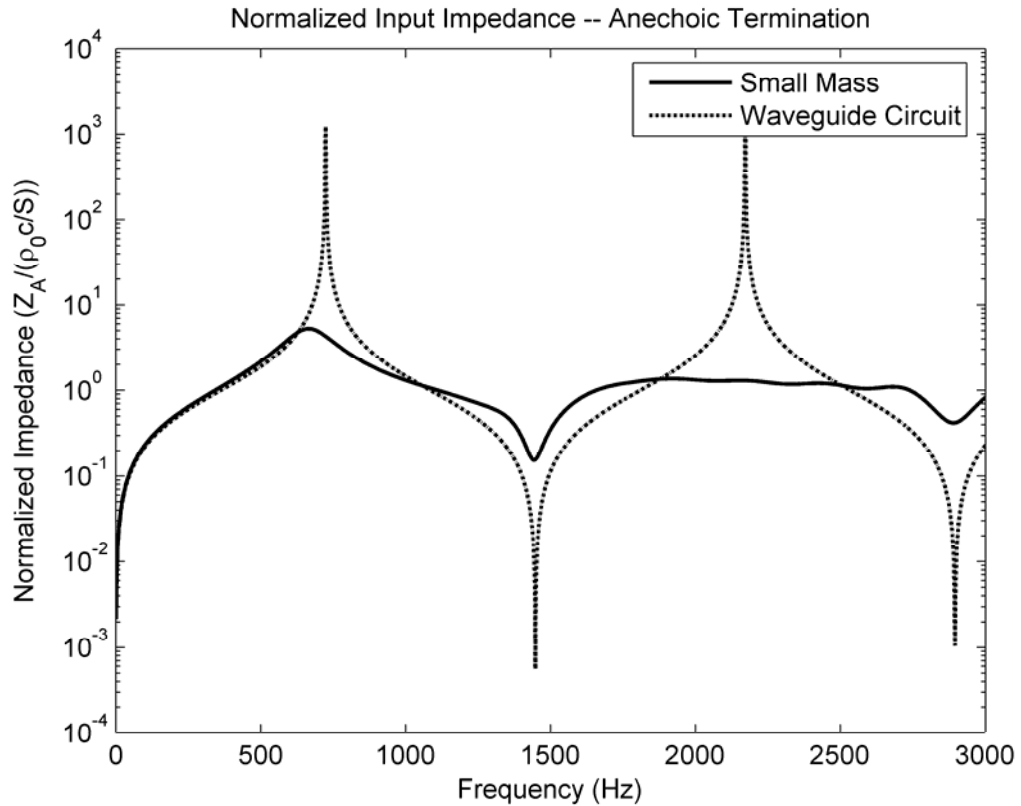
Figure 4.8. Normalized input impedance comparison. Solid trace is the input impedance for a very small mass. Dotted trace is the input impedance of a single waveguide circuit with a termination impedance of zero.

To further investigate this resonance resulting from the mass of air in the holes and the volume of air inside the shotgun tube, we wish to find the relationship between the known volume of air in the tube and the effective volume of air seen by each hole. If we treat each hole region as an acoustic mass M_A and acoustic compliance C_A, we can use the two equations [18]:

$$f_0 = \frac{1}{2\pi} \sqrt{\frac{1}{M_A C_A}} \tag{4.33}$$

$$C_A = \frac{V_H}{\rho_0 c^2} . \tag{4.34}$$

f_0 is the frequency at which the peak appears in the impedance plot where the Helmholtz resonance occurs. Solving for the effective volume V_H then gives

$$V_H = \frac{\rho_0 c^2}{4\pi^2 f_0^2 M_A} . \tag{4.35}$$

In principle, the total volume of the tube would then equal the sum of the various effective hole volumes. However, this notion leads to some discrepancies. Figure 4.9 shows the actual volume inside the shotgun tube versus the calculated total volume from the model as described above. Obviously, there is a decreasing difference as the number of holes in the tube increases or the spacing between holes decreases.

The masses of air in the holes are only seeing an effective volume equal to the volume of air between adjacent holes. This explains why the two traces in Fig. 4.9 are not identical. If the effective volume of air is centered on the hole, there remains "unused" air near the source and the termination in the tube. The more holes in the tube, the smaller this excess air volume becomes, which leads to the asymptotic behavior in Fig. 4.9.
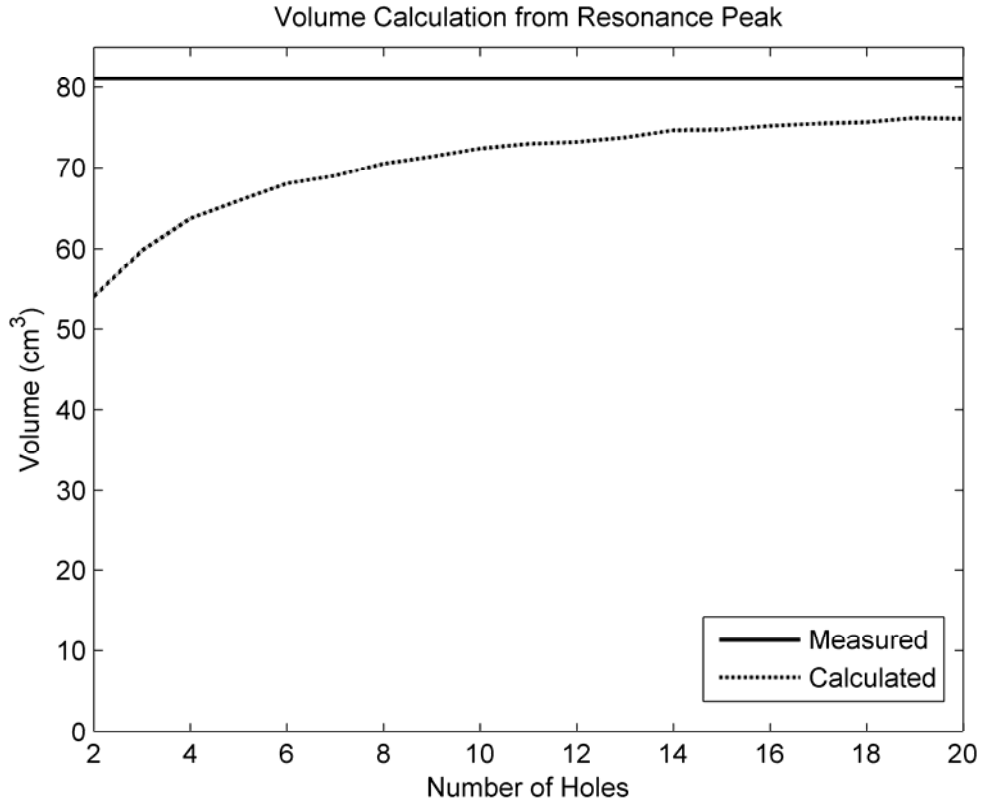
Figure 4.9. Actual volume inside the shotgun tube (solid trace). Calculated volume in the shotgun tube model (dashed trace). The tube radius is 5.08 cm and the tube length is 1 m.

Once the acoustic input impedance Z_{AI} of the tube is calculated, the output pressure from the source coupled to the tube can be found from the following relation,

$$\hat{p}(0) = \hat{U}(0)Z_{AI} \tag{4.36}$$

where $\hat{U}(0)$ is the volume velocity value associated with the source. For a constant volume velocity source, the output pressure is directly related to the input impedance of the tube.

The next step is to use the source volume velocity and the tube impedance values to solve for the volume velocities at each hole in the tube. This can be done by using the well-known current-divider rule to solve for the flows into the shunt branches of the tube circuit (see Fig. 4.4).

Once the volume velocities are known, we need to calculate the radiated pressure for each hole at a given field position. Assuming each hole radiates as a point source, the far-field pressure at a distance r away is expressed for the nth hole as

$$\hat{p}_n(r) = \left(\frac{j\rho_0 ck\hat{U}_n}{4\pi r} \right) e^{-jkr} \tag{4.37}$$

where $\hat{U}_n$ is the volume velocity of the hole [10]. We can use this expression for the radiated pressure generated from each hole due to the fact that the wavelengths we are interested in are much larger than the radius of the holes.

Since we are assuming that the measurements are taken in the far field of the tube, we can make a simplification in the calculation of r for each hole. We let the acoustic center of the array of holes be defined as the geometric center of the array as shown in Fig. 4.10, where r is the distance from the center of the array to field point P at an angle θ to the normal of the array.

The distance from one element in the array to the field point will be defined as R_n, as shown in Fig. 4.10. This distance can be defined from the law of cosines as

$$R_n^2 = r^2 + l_n^2 + 2rl_n \sin(\theta). \tag{4.38}$$

If we assume that $r \gg l$, this distance can be approximated as

$$R_n \approx r + l_n \sin(\theta) \tag{4.39}$$

for phase terms and

$$R_n \approx r \tag{4.40}$$

for amplitude terms. The latter value is less critical in the superposition process when combining pressures from all sources.
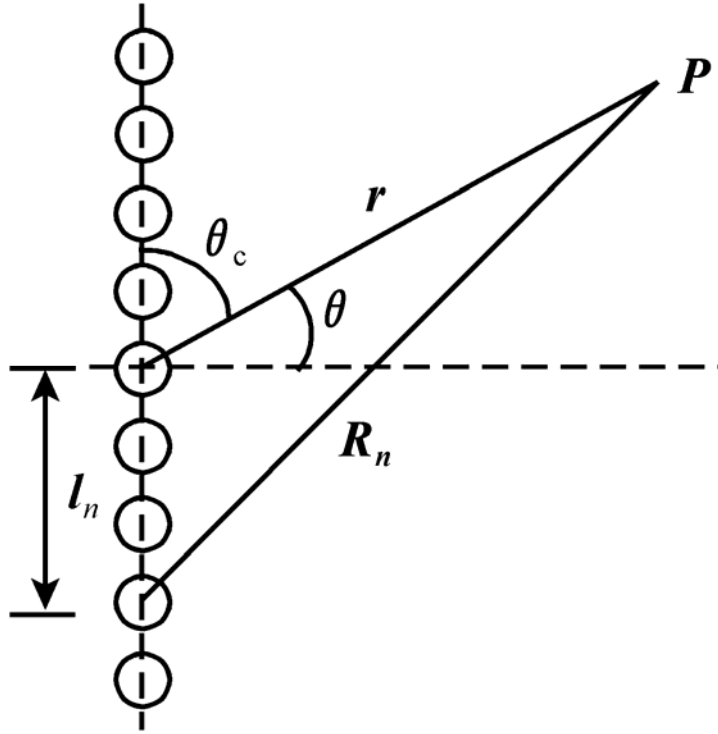
Figure 4.10. Distance approximation for an element in an array to a measurement point in the far-field.

We can now substitute Eqs. (4.39) and (4.40) into Eq. (4.37) to give us a final form for the far-field pressure, which is now a function of r and θ.

$$\hat{p}_n(r,\theta) = \left(\frac{j\rho_0 ck\hat{U}_n}{4\pi r} \right) e^{-jk(r+l_n \sin(\theta))}. \qquad (4.41)$$

By the principle of superposition, we can define the total sound field radiated by an array of N holes as the sum of the sound fields radiated by the individual holes. This is finally written as

$$\hat{p}(r,\theta) = \left(\frac{j\rho_0 ck}{4\pi r} \right) e^{-jkr} \sum_{n=1}^{N} \hat{U}_n e^{-jkl_n \sin(\theta)}. \qquad (4.42)$$

Once the final pressure at a distance r from the center of the shotgun tube is found for all angles, the beamwidth for each frequency may be computed. This is done by

finding the points that are 6 dB down on either side from $\theta_c = 0°$ (see Fig. 4.11). In Figure 4.12, the beamwidth is plotted as a function of frequency in order to evaluate the performance of a given tube model.
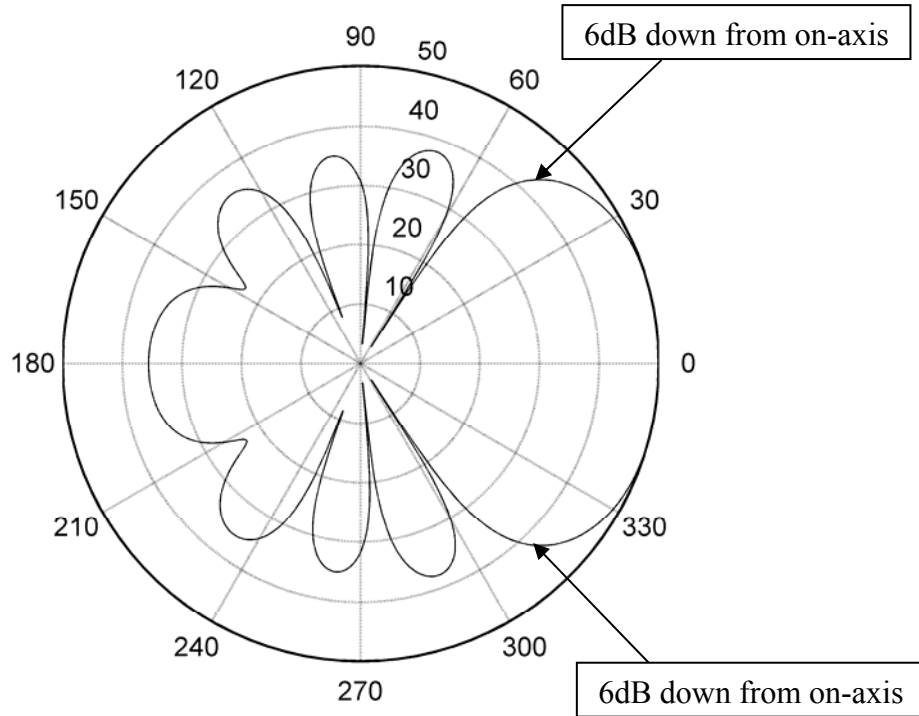
Figure 4.11. Sample polar plot for a shotgun loudspeaker. The polar angle is θ_c, not θ (see Fig. 4.10).

The tube has six holes that are spaced 22 cm apart from each other, a tube radius of 5.08 cm, and hole radii of 1.27 cm. The simulation also assumes an anechoic termination at the end of the tube. This curve offers several pieces of information, such as the point below which the shotgun loudspeaker becomes omnidirectional ($\approx$ 200 Hz in this case). The undulations that occur at tube resonances will be explained in the next chapter.

The following chapter also describes how shotgun tube characteristics, such as hole radii

and overall length of the array, change the performance of a shotgun loudspeaker.
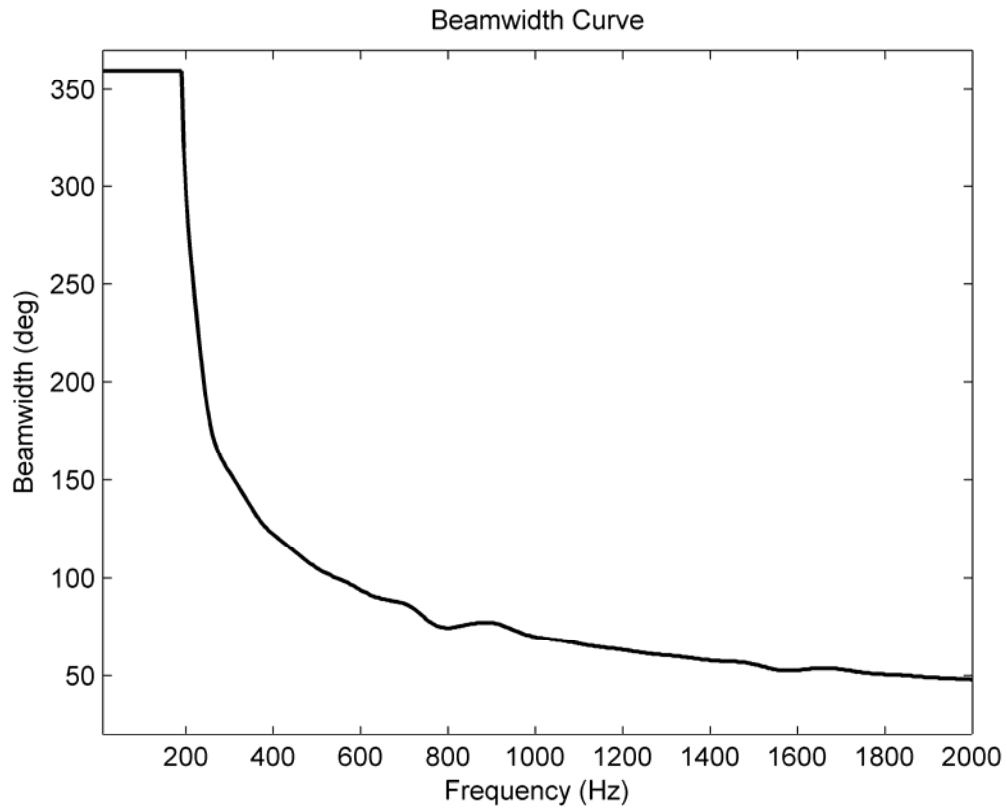
Figure 4.12. Beamwidth curve for a shotgun loudspeaker with an anechoic termination, 5.08 cm tube radius, 1.27 cm holes radius, and 6 holes spaced at 22 cm.

CHAPTER 5

PRELIMINARY MODEL RESULTS AND ANALYSIS

In order to look at the effect that each physical characteristic of the shotgun tube has on its beamwidth, the preliminary computational model was used to compute multiple iterations for a given tube, while only varying a single parameter from one run to the next. The simulations initially assumed an anechoic termination and a constant volume velocity input. They then involved a rigid termination, open termination, and a passive radiator termination. Individual figures present overlapped beamwidth curve plots for each group of runs. The comparisons afforded by the plots reveal the dominant impact of each physical characteristic.

5.1 Varying the Spacing Between the Holes

Figure 5.1 shows the beamwidth curves for five different shotgun loudspeakers with anechoic terminations. All physical characteristics of the tube (e.g., hole radius, tube radius, wall thickness, and the number of elements) were held constant except for the spacing between the holes and the overall length. The number of holes in the tube was held constant at six and the spacing of the holes was varied from 10 to 30 cm at 5 cm increments which also incrementally increased the length of the shotgun tube.

Two key effects that the spacing of the holes has on the beamwidth can be drawn from this figure. First, the larger the spacing between holes, the longer the array becomes, which increases the directivity – especially at low frequencies above the omnidirectional cutoff [9]. For example, the dotted trace, which is the simulation for a

spacing of 10 cm, shows that the design becomes omnidirectional at approximately 300 Hz. Remarkably, if the spacing is increased by only a factor of two, the beamwidth at 300 Hz becomes 150° which is a 60% beamwidth reduction. However, reduction comes at a cost of doubling the length of the array.
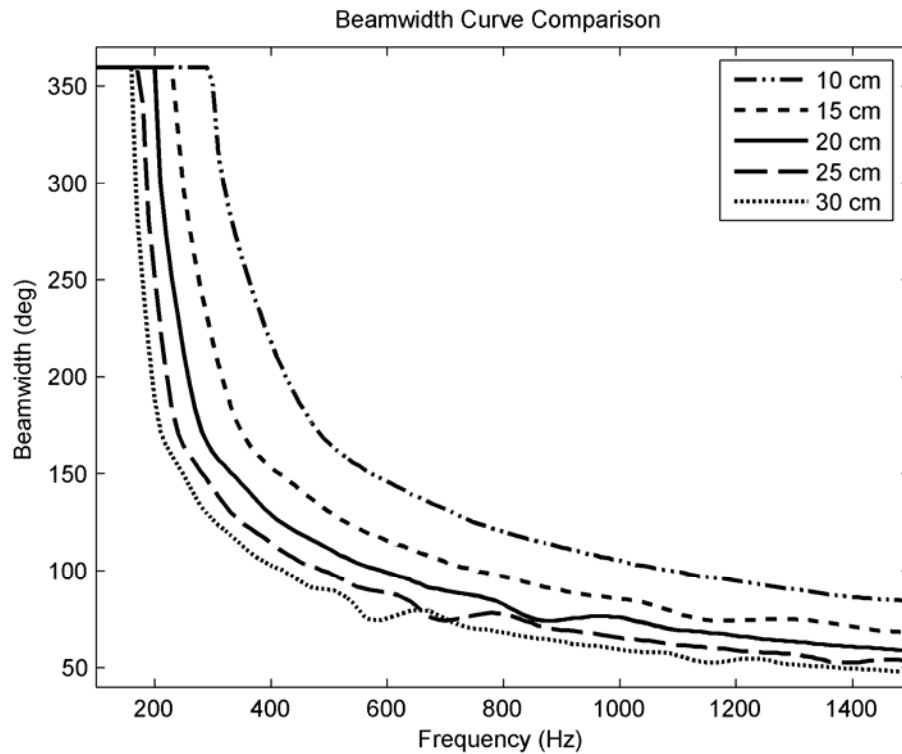
Figure 5.1. Beamwidth curve for shotgun loudspeakers, wherein the spacing between the holes in the tube was varied from 10 to 30 cm at 5 cm increments. All other variables were held constant except the overall tube length.

Another effect that can be seen in Fig. 5.1 is the small undulations or dips that appear on each trace. These undulations occur at the primary resonance frequencies associated with the spacing between adjacent holes inside the tube, i.e., at the frequencies whose half-wavelengths are equal to the spacing between the holes and their subsequent harmonics. For example, in the lowest trace of Fig. 5.1 (30 cm spacing), the spacing corresponds to a half-wavelength frequency of 571 Hz, which is where the first

undulation in the trace occurs. The next harmonic is at 1143 Hz. The corresponding

undulation is a bit harder to see, but is nevertheless present.

5.2   Varying the Number of Holes

Figure 5.2 shows the beamwidth curves for another parameter variation. In this

case, all physical characteristics of the tube were held constant except for the number of

holes (e.g., hole radius, tube radius, wall thickness, and the tube length). The length of

the tube was held at a constant 1.5 m and the number of equally spaced holes over that

length was varied from three to nine, at two hole increments. Of course, this also

changed the spacing between holes, so the effects of only adding radiating elements to

the array were more difficult to extract.
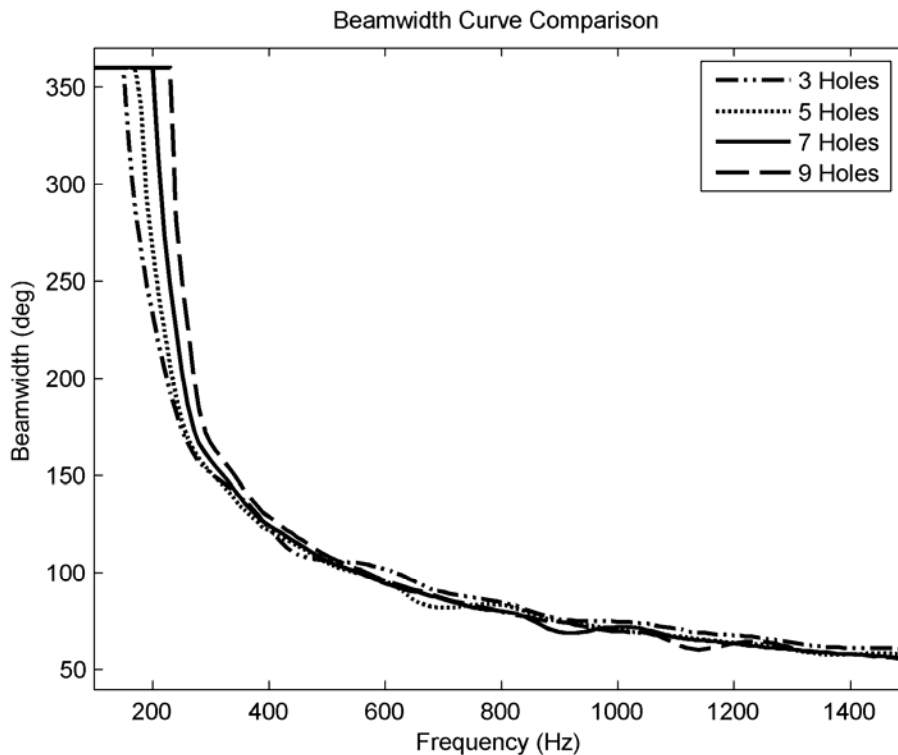
Figure 5.2. Beamwidth Curve for shotgun loudspeakers with a constant tube length. The number of holes
in the tube was varied from three to nine at increments of two. All other variables were held constant
except the hole spacing.

Although the beamwidth curves do not change significantly from run to run, there are subtle differences that are noteworthy. First, the shotgun tube performs better at low frequencies with fewer holes (which also corresponds to a larger spacing between holes). It is well understood in array theory that as the spacing of the elements in the array increases, the directivity control achieved in the low-frequency region increases [9]. However, the behavior at higher frequencies essentially converges to the same result for all cases and thus does not seem to be affected by the changes.

Another difference between the iterations is the movement of the small undulations that are defined by the previously discussed spacing between the holes of the tube. This is simply an artifact of the spacing when holes are added but the overall length of the tube is held constant.

While interesting, the interaction of hole spacing and number of elements made it difficult to differentiate between the effects of each. Consequently, another simulation was run, as shown in Fig. 5.3. In this simulation, the spacing between elements was held constant and the overall tube length was allowed to grow as the number of elements increased. The fact that the hole spacing was held constant is validated by the static ripple seen in each run at 779 Hz.

In this figure, it is clear that adding holes to the tube (and consequently increasing the overall length) improves the performance above 200 Hz at all frequencies. However, the points at which the devices become omnidirectional does not change a great deal. The slopes of the curves above the omnidirectional cutoff frequencies notably increase with increasing numbers of elements in the array.
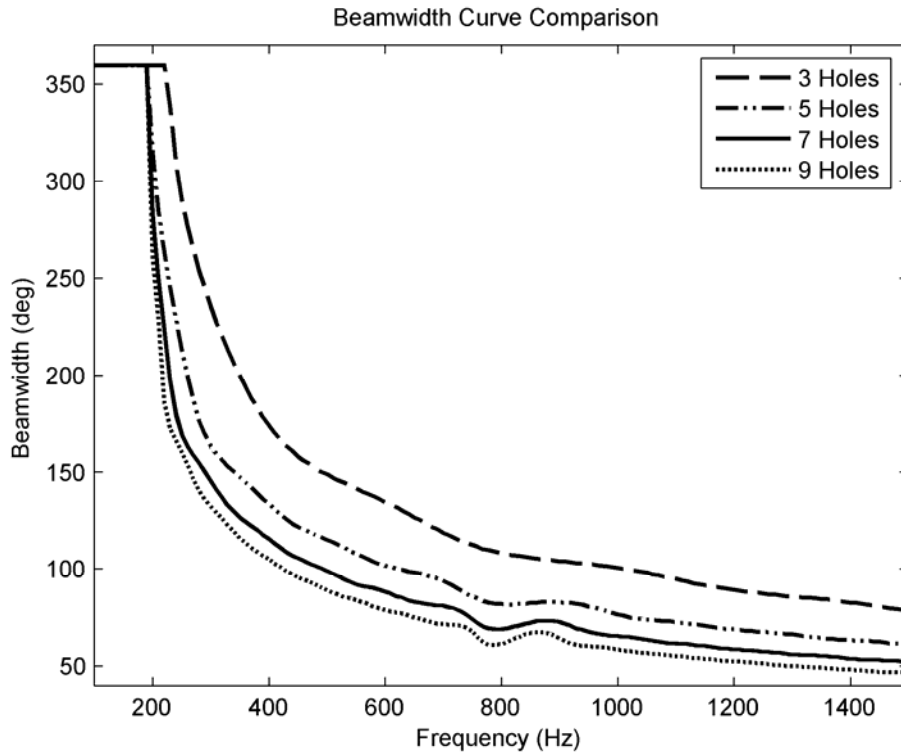
Figure 5.3. Beamwidth curve for shotgun loudspeakers with a constant hole spacing. The number of holes in the tube was varied from three to nine at two hole increments. All other variables were held constant except the overall tube length.

These two sets of simulations suggest that the spacing of elements primarily determines the performance at lower frequencies while the overall length of the array primarily determines the performance at higher frequencies.

5.3   Varying the Tube Radius

Figure 5.4 shows the beamwidth curves for cases in which all physical characteristics of the tube were held constant except for the radius of the tube (e.g., hole radius, tube length, wall thickness, and the number of elements). The tube radius was varied from 4 to 8 cm at 1 cm increments.

It is quite clear from the figure that all simulations converge at higher frequencies, where the tube radius apparently has no effect on the performance of the system. At low frequencies, however, the beamwidth curve continuously moves downward and decreases the frequency at which the tube becomes omnidirectional.
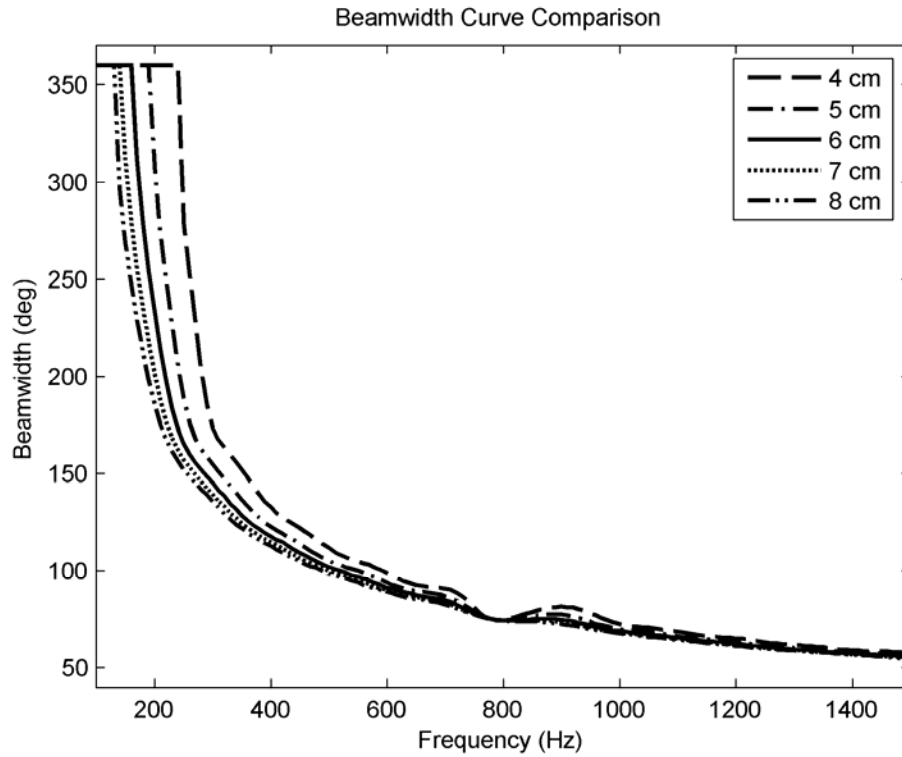
Figure 5.4. Beamwidth curve for shotgun loudspeakers, wherein the radius of the tube was varied from 4 to 8 cm at 1 cm increments. All other variables were held constant.

The most important effect that varying the tube radius has on the model is the cutoff frequency for the first cross mode of the shotgun tube, or the frequency above which the tube no longer behaves as a plane-wave tube. This cutoff frequency is inversely proportional to the tube radius, a_t:

$$f_c = \frac{j_{mn} c}{2\pi a_t},$$

(5.1)

where c is the speed of sound and $j_{mn} = 1.84$ is the first zero of the derivative of the first-order cylindrical Bessel function [10].

Figure 5.4 shows these cutoff frequencies for each run by vertical lines plotted at each cutoff frequency. However, only two of these values fall within the range of the x-axis limits. The larger the tube radius, the lower the cutoff frequency becomes [which can be deduced from Eq. (5.1)]; therefore the line at approximately 1250 Hz is the cutoff for the largest tube in the simulation (8 cm radius).

It should be noted that the cutoff frequency for the first cross-mode creates a limit for our model as well as the shotgun loudspeaker prototypes. Above this frequency, the device will no longer perform as a well-behaved end-fire array and is therefore unpredictable by the analytical model.

5.4 Varying the Hole Radius

Figure 5.5 shows the beamwidth curves for five different shotgun loudspeakers. All physical characteristics of the tube were held constant (e.g., tube length, hole spacing, wall thickness, and the number of elements) except for the radius of the holes. The hole radius varied from 0.5 to 2.5 cm in 0.5 cm increments.

The general trend of this simulation is that as the hole radius increases, the directional performance of the shotgun loudspeaker decreases. Not only does the point at which the device becomes directional increase, but the entire curve is shifted upward. The key reason for this change is the effect that varying the hole radius has on the acoustic impedance of each hole. Since the hole radii remain small compared to

wavelength themselves, they individually combine to produce monopole-like radiation at all frequencies of interest.
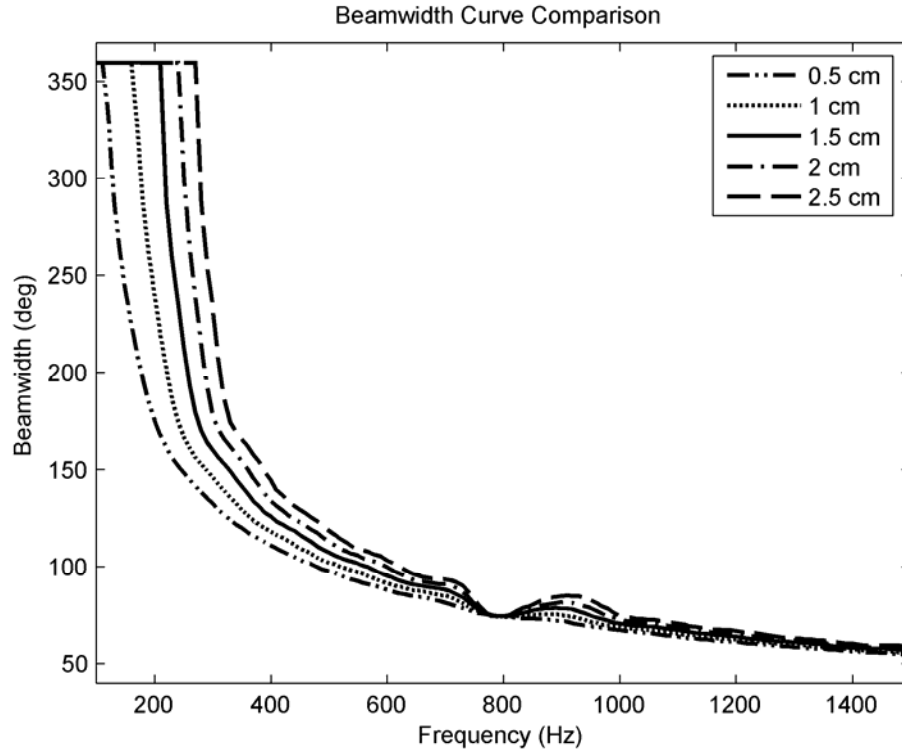
Figure 5.5. Beamwidth curve for shotgun loudspeakers, wherein the radius of the holes in the tube was varied from 0.5 to 2.5 cm in 0.5 cm increments. All other variables were held constant.

In Chapter 4, we found that the acoustic impedance of a single hole in the tube can be expressed as

$$Z_{AH} = \frac{\rho_0 c k^2}{2\pi} + j\frac{\omega\rho_0}{\pi a^2}\left(\frac{8a}{3\pi} + t\right),$$ (5.2)

where a is the hole radius. As a increases, the value of the reactive terms decreases, which ultimately increases the volume velocity $\hat{U}$ produced at each hole.

Figure 5.6 plots the values of $\hat{U}$ at 1200 Hz for each hole and all five hole diameters in the Fig. 5.5 simulation. As a progressively increases, the volume velocity

increments upward by approximately 0.5 m³/s and remains relatively constant for all holes. Small fluctuations correspond to the small changes between traces at 1200 Hz in Fig. 5.5. A uniform value of $\hat{U}$ across all the holes allows for a more efficient interaction in the far-field.
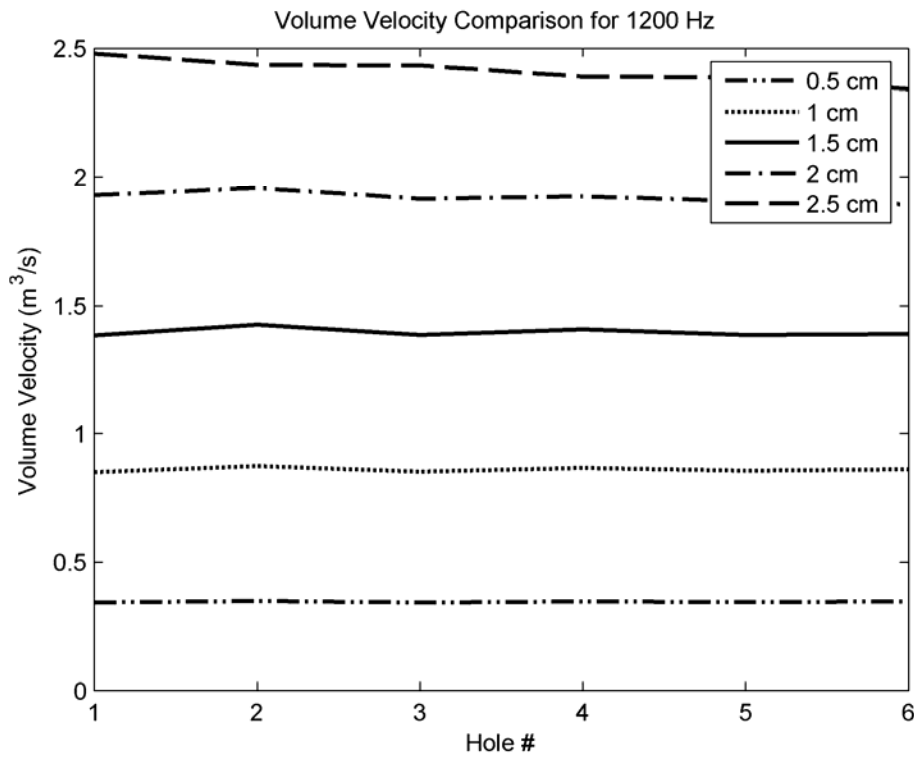
Figure 5.6. Volume velocity for each hole at 1200 Hz. The five traces correspond to the five traces shown in the Fig. 5.5 simulation.

Figure 5.7 plots the value of $\hat{U}$ at 400 Hz for each hole and the same set of simulations. At this lower frequency, the volume velocity can increase in jumps of 2 or 3 m³/s for each increment in a and it begins to fluctuate widely over the holes. These variations correspond to the larger changes between traces at low frequencies in Fig. 5.5,

64

where the increased variation in amplitudes radiating out of the holes decreases the efficiency of the far-field interactions.
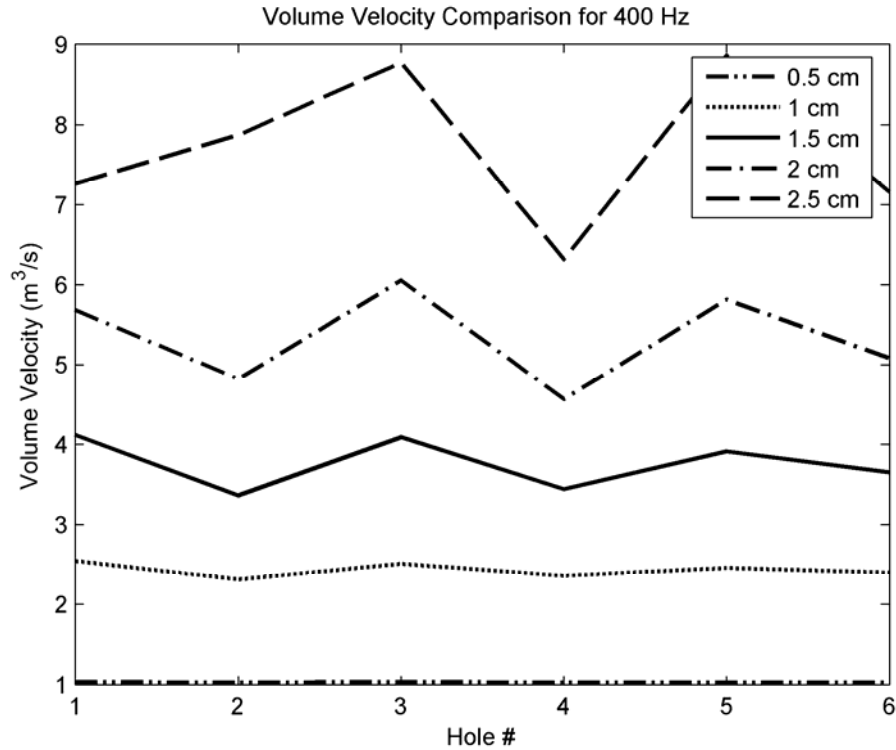
Figure 5.7. Volume velocity for each hole at 400 Hz. The five traces correspond to the five traces shown in the Fig. 5.5 simulation.

5.5   Varying the Termination Impedance

All of the previous simulations in this chapter have assumed that the shotgun tube was terminated with an anechoic wedge, that allows no reflections from the end of the tube. The effect of changing the termination impedance will now be explored in detail.

5.5.1 Anechoic Termination

An anechoic termination requires the reflection coefficient R to be 0 for all frequencies. In general, the acoustic impedance Z_A of a termination is related to R by the following equation [18]:

$$Z_A = \left(\frac{\rho_0 c}{S}\right)\left[\frac{1+R}{1-R}\right].$$ (5.3)

where S is the tube cross-sectional area. If R is set to 0, the acoustic impedance for an anechoic termination can be written as

$$Z_{ATA} = \frac{\rho_0 c}{S}.$$ (5.4)

An anechoic termination is then simply the characteristic impedance of the plane wave propagating down the tube. As the plane wave encounters the termination, it "sees" it as an infinitely long tube so no reflections are produced.

Figure 5.8 shows the normalized input impedance magnitude $\dfrac{|Z_{in}|}{\left(\rho_0 c \middle/ S\right)}$ for the tube with 6 holes spaced at 22 cm, a 1.27 cm hole radius, a 5.08 cm tube radius, and an anechoic termination. As discussed in Chapter 4, the large spike just under 200 Hz is due to the small masses of air resonating with the volume of air inside the tube. The smaller undulations at approximately 800 and 1600 Hz are due to resonances inside the tube between holes, resulting from the impedance discontinuities at each opening.

This input impedance was coupled to a constant volume velocity source and the volume velocities produced at each hole were calculated. The radiated pressures were then found and summed in the farfield using the procedure described in Chapter 4. Figure 5.9 provides the resulting beamwidth curve for the configuration.
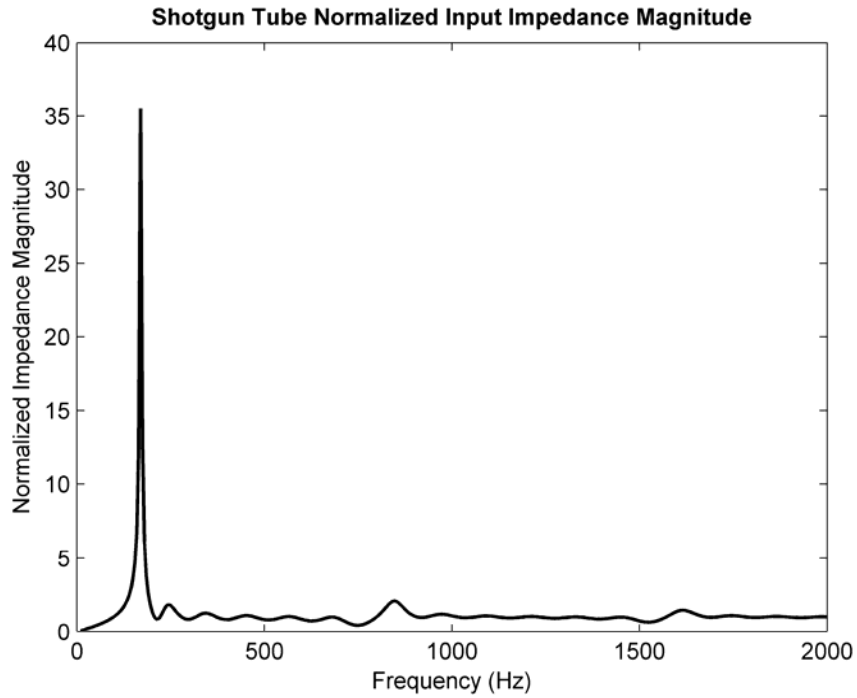
Figure 5.8. Normalized input impedance magnitude for a tube with an anechoic termination. This model has 6 holes spaced at 22 cm, a 1.27 cm hole radius, and a 5.08 cm tube radius.
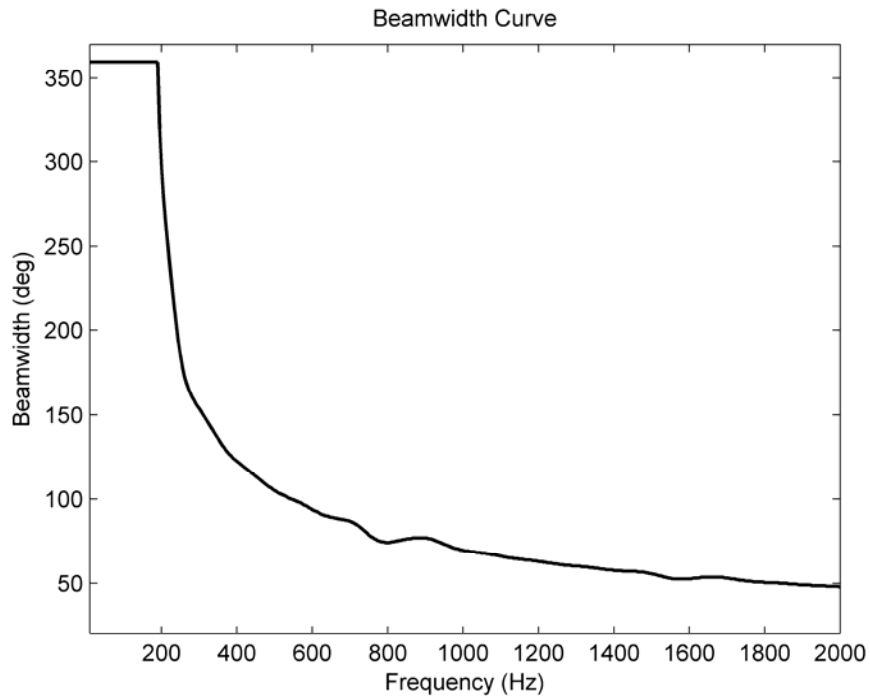
Figure 5.9. Beamwidth curve for a tube with an anechoic termination. This model has 6 holes spaced at 22 cm, a 1.27 cm hole radius, and a 5.08 cm tube radius.

The curve shows the same small undulations at 800 and 1600 Hz that were present in the impedance plot. Figures 5.10, 5.11, and 5.12 are polar plots from this same simulation that help visualize what is happening at these small ripples in the beamwidth curve. Figure 5.10 is the polar pattern at 600 Hz. The level of the rear lobe is approximately 13 dB lower than that of the single front lobe and oriented along the axis of the tube. This is characteristic of an end-fire configuration.
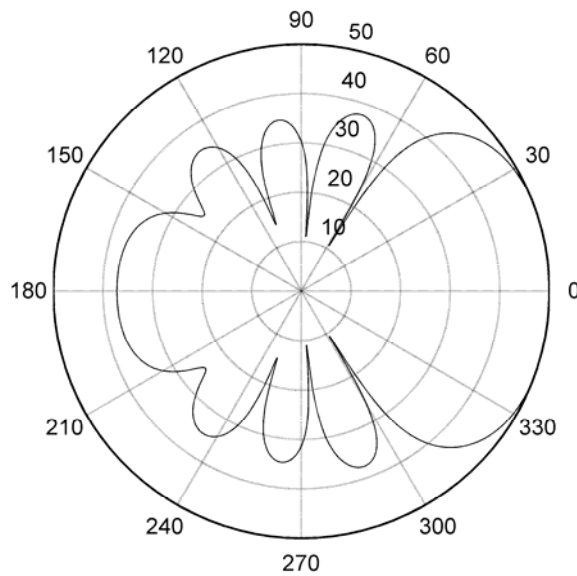
Figure 5.10. Polar pattern for a shotgun tube with an anechoic termination at 600 Hz.

Figure 5.11 is the polar pattern at 800 Hz which is near the region where undulations are found on the beamwidth curve. In this plot, there is an increased level in the rear lobe and the polar response becomes much more symmetric from front to rear. The increase in the rear lobe is due to spatial aliasing. Chapter 2 explained that when the delay between elements in an end-fire array is equal to the time it takes the acoustic wave to propagate to the next element, this results in a well defined front lobe pointing in the direction of the delay. In the shotgun tube design, as the frequency increases to where the

wavelength is twice the hole spacing, the "sampled" points along that shotgun tube where the holes are located look as though there have been two opposite delays (summing to zero) superimposed at each hole. This effective delay in both directions consequently produces a rear lobe with the same magnitude as the front lobe, as seen in Fig. 5.11.
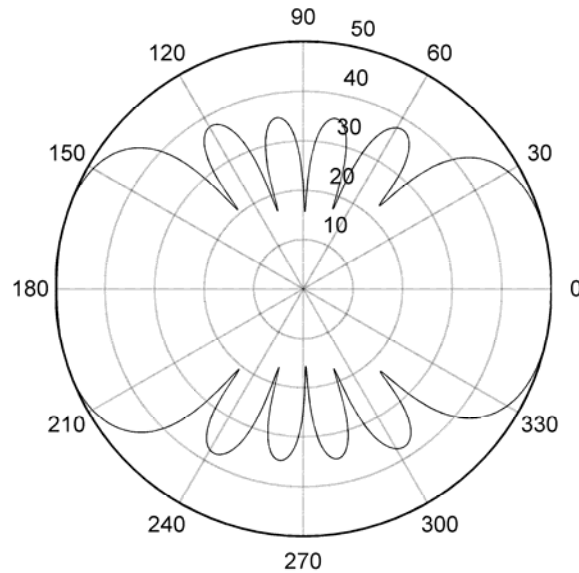
Figure 5.11. Polar pattern for a shotgun tube with an anechoic termination at 800 Hz.

As the frequency continues to increase, the effective delay to the rear begins to alias into a larger and larger delay which steers a split set of mirrored rear lobes away from 180˚, as seen in Fig. 5.12.
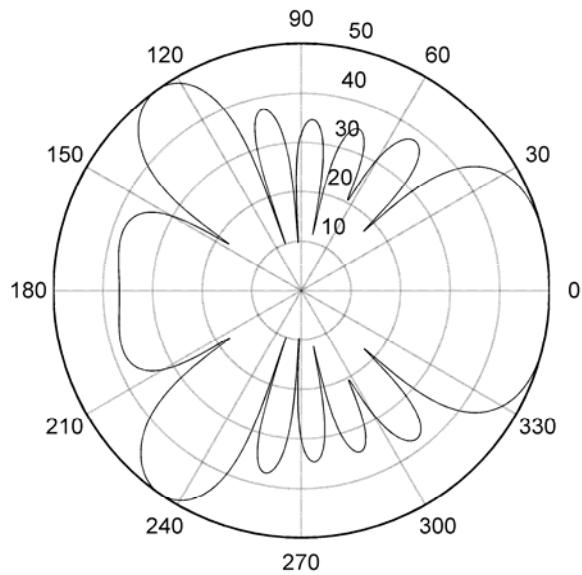
Figure 5.12. Polar pattern for a shotgun tube with an anechoic termination at 1000 Hz.

This spatial aliasing occurs at the frequency whose half-wavelength is equal to the spacing between the holes, as well as integer multiples of this frequency. If the polar pattern is animated over frequency, the increased rear lobes splitting into mirrored side lobes (as seen in Fig. 5.12) occurs at each of these frequencies and is an artifact that cannot be avoided.

Returning to Fig. 5.9, another piece of information that can be gathered from the beamwidth curve is the point of "omnidirectionality" at approximately 200 Hz. This curve will be used as our benchmark for comparison with other tube terminations.

5.5.2 Rigid Termination

A rigid termination to the tube has a reflection coefficient of 1 for all frequencies. The acoustic impedance of such a condition approaches an infinite value. For the numerical simulations of this work, the rigid impedance was approximated as

70

$$Z_{ATC} = 1000 \frac{\rho_0 c}{S}.$$ (5.5)

Figure 5.13 shows the input impedance for a tube with 6 holes spaced at 22 cm (giving an overall tube length of 1.54 m), a 1.27 cm hole radius, a 5.08 cm tube radius, and a rigid termination given by Eq. (5.5). This figure shows the same Helmholtz resonance just below 200 Hz as seen in Fig. 5.8 with the anechoic termination, but the resonances between holes inside the tube are much more exaggerated now. This is due to the large reflections from the end of the tube, which then continue to build on each other.

Note that all resonance peaks (with the exception of the first peak) are harmonically related because the holes are all equally spaced and the length of tube from the last hole to the termination is also equal to the hole spacing. Many harmonics are seen which are not only interactions between neighboring holes, but interactions of holes all along the tube and interactions with the termination as well.

Figure 5.14 is the resulting beamwidth curve for the rigid termination configuration. The undulations that occurred in the anechoic terminated case are still present, but they are much more exaggerated. A great disadvantage to the rigidly terminated case is that the reflections coming from the end of the tube create a superposition of an end-fire array with the delays reversed at all frequencies and therefore pointing in the opposite direction. The result (which occurs at all frequencies) can be seen in Fig. 5.15, where the level of the rear lobe is much larger and symmetric for the rigidly terminated case.
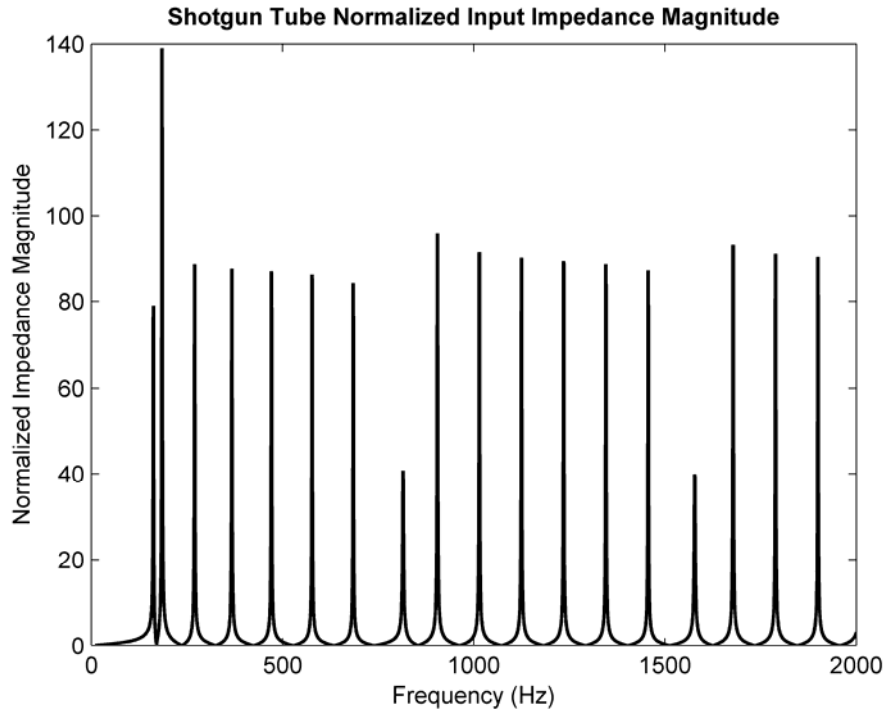
Figure 5.13. Normalized input impedance magnitude for a tube with a rigid termination. This model has 6 holes spaced at 22 cm, a 1.27 cm hole radius, and a 5.08 cm tube radius.
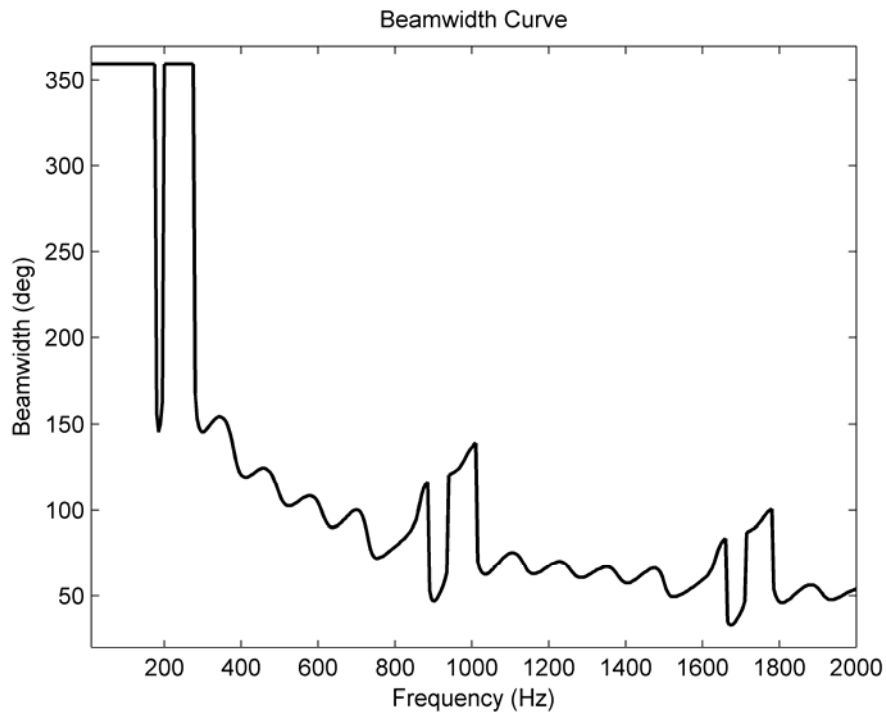
Figure 5.14. Beamwidth curve for a tube with a rigid termination. This model has 6 holes spaced at 22 cm, a 1.27 cm hole radius, and a 5.08 cm tube radius.

72
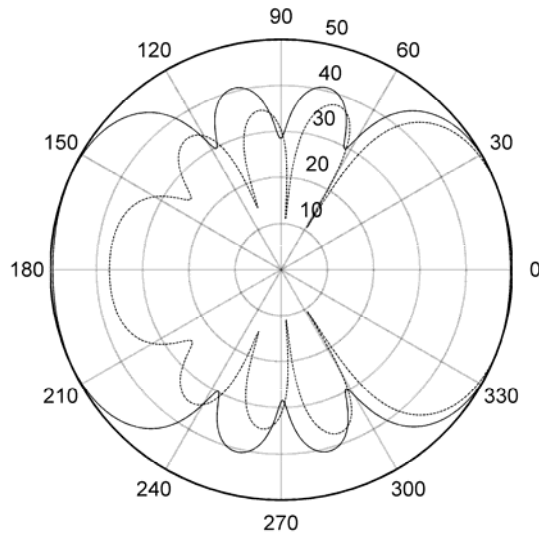
Figure 5.15. Polar pattern for the rigid termination (solid trace), in comparison to the anechoic termination (dashed trace) at 600 Hz.

5.5.3 Open Termination

The representation for an open end of a tube is a bit more complicated than the previous two cases. In the low-frequency approximation, the acoustic impedance of this condition can be written as [18]

$$Z_{ATO} \approx \frac{\rho_0 c}{S}\left[\frac{(ka)^2}{4} + j(0.61ka)\right]. \tag{5.6}$$

For a 5.08 cm tube radius, this expression is strictly valid up to about 1100 Hz, but may be used as a rough approximation above that frequency. Figure 5.16 shows the normalized real and imaginary parts of the acoustic impedance for an open-ended tube of radius 5.08 cm radiating into free space. The positive imaginary term indicates that there is an effective mass of air at the end of the tube interacting with the sound field, as opposed to a compliant volume of air, which would have a negative value.

73
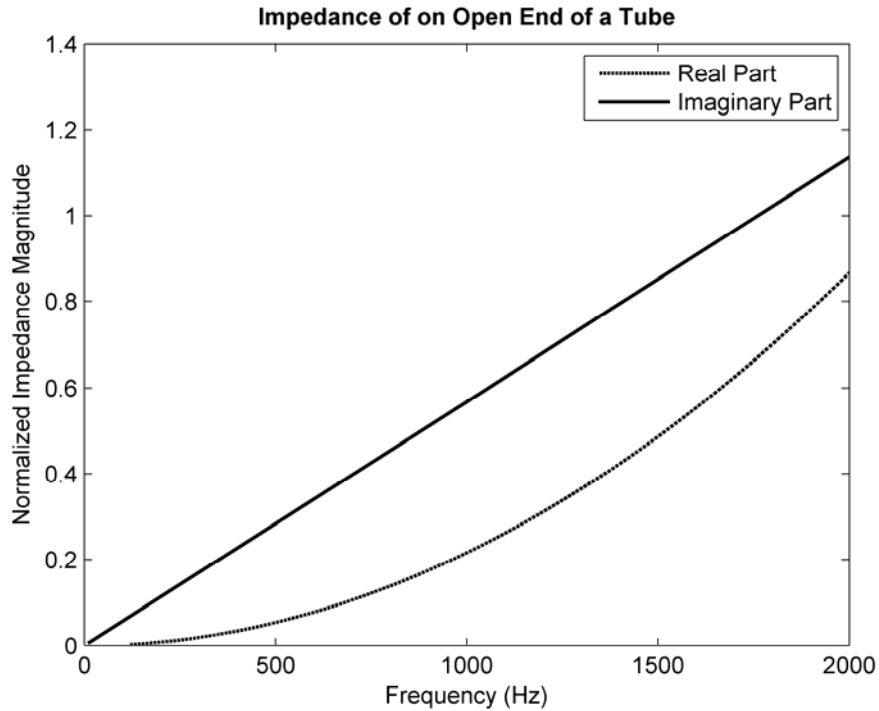
Figure 5.16. Normalized radiation impedance magnitude plot for an open termination. The solid trace is the imaginary part and the dotted trace is the real part.

Figure 5.17 shows the normalized input impedance magnitude for the tube with the open end. This is very similar to the rigid condition but the resonance peak heights are not quite as strong. The peaks are also shifted significantly in frequency. This is due to the change in boundary condition at the end of the tube, where in the low frequency approximation an open end of a tube acts as a pressure release termination.

Figure 5.18 is the resulting beamwidth curve for the open tube configuration. It is clear that the tube is omnidirectional at virtually every frequency. The only dip in the curve occurs at the frequency whose half-wavelength is equal to the hole spacing. The polar pattern shown in Fig. 5.19 is for 815 Hz, the frequency at which the beamwidth curve has its lowest value. This is the "best case scenario."

74
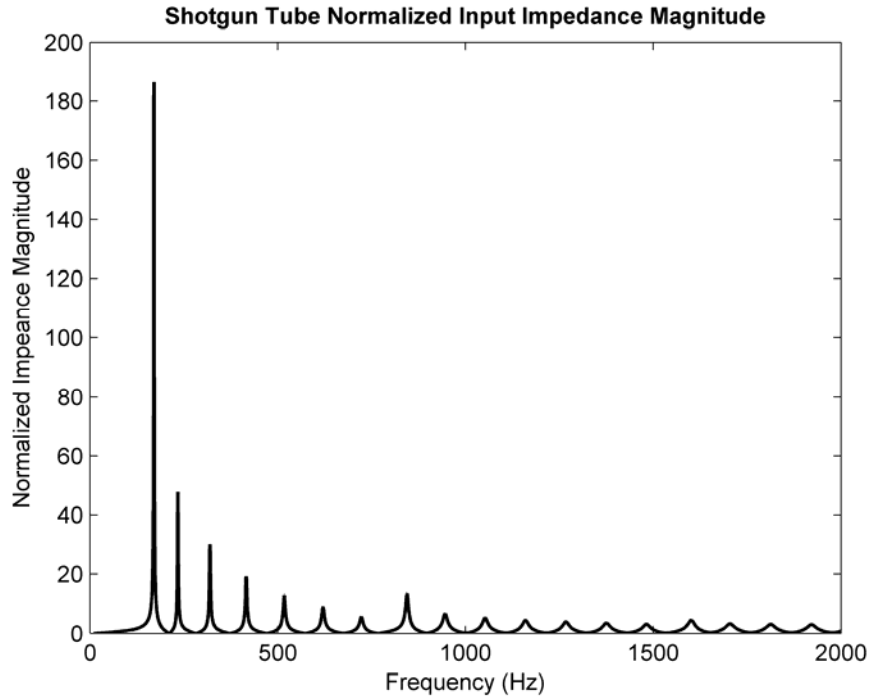
Figure 5.17. Input impedance for a tube with an open termination. This model has 6 holes spaced at 22 cm, a 1.27 cm hole radius, and a 5.08 cm tube radius.
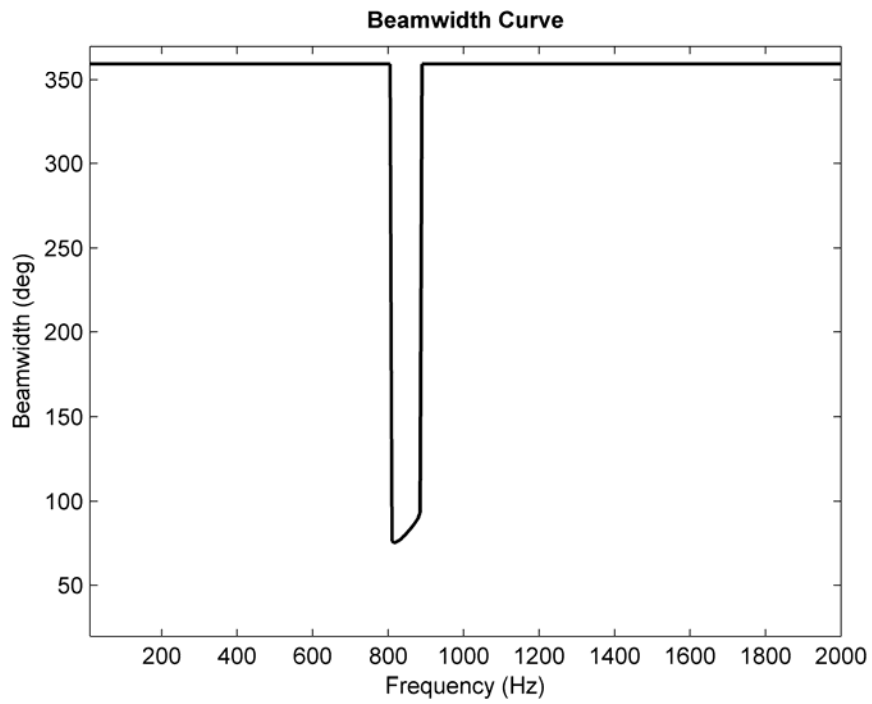
Figure 5.18. Beamwidth curve for a tube with an open termination. This model has 6 holes spaced at 22 cm, a 1.27 cm hole radius, and a 5.08 cm tube radius.

75
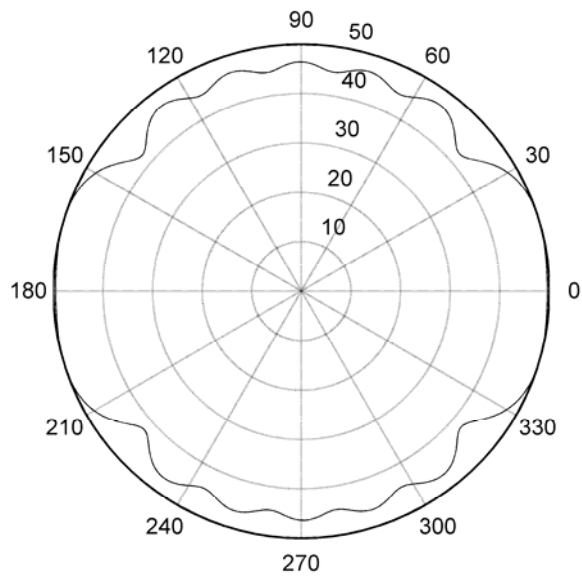
Figure 5.19. Polar pattern for the shotgun loudspeaker with an open end at 815 Hz.

In order to investigate why the open ended tube performs so poorly, the volume velocity was plotted for all the tube holes and the end of the tube. This is shown in Fig. 5.20 for all 6 holes where hole number seven is the open end. It is clear that the radiated pressure is much higher for the open end than any of the smaller holes along the axis of the tube. Consequently, the smaller holes do not have the acoustic output to sufficiently interact with the radiation from the open end to create a well defined beam in any direction. This mismatch between radiators in this system is a clear reason why the open tube termination is not an optimal choice for our design.
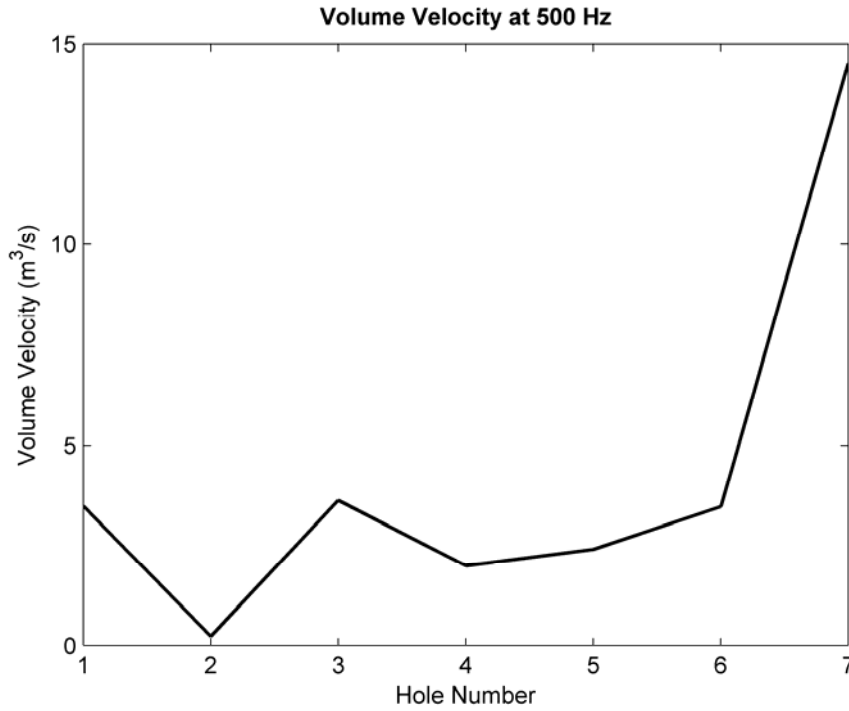
Figure 5.20. Volume velocity for the shotgun tube holes and open termination at 500 Hz.

5.5.4 Drone Cone Termination

The final termination condition that was investigated was a mounted drone cone (passive radiator) at the end of the tube. A drone cone is simply a loudspeaker without its motor (magnet, voice coil, etc.) attached to the rear of the basket. Figure 5.21 shows a photograph of a typical drone cone and Fig. 5.22 is a diagram of how the unit would be mounted to the shotgun tube.

Figure 5.21. Photograph of sample drone cone. Tymphany's Peerless 830547 XLS passive radiator. Copyright © Tymphany Corporation.
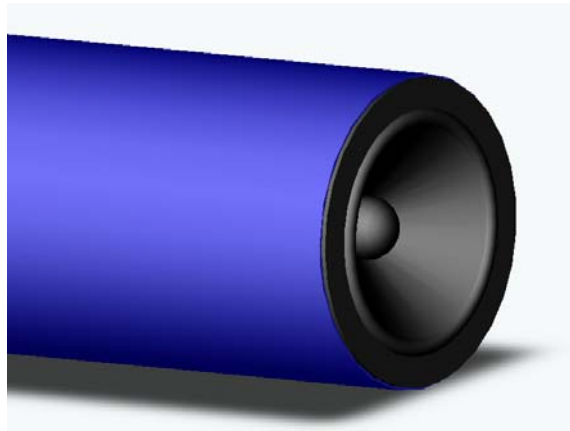
Figure 5.22. Diagram of the drone cone mounted at the end of a shotgun tube.

It is fairly easy to model a drone cone with an equivalent circuit which can then be placed directly into the shotgun tube circuit. A drone cone has a moving mass (M_{MD}) which includes moving components such as the diaphragm and portions of the surround, a compliance (C_{MS}) created by the surround and the spider, and a suspension resistance (R_{MS}) due to lossy mechanisms [13]. Figure 5.23 shows the simple equivalent circuit for this system.

78

$$M_{MD} \quad C_{MS} \quad R_{MS}$$
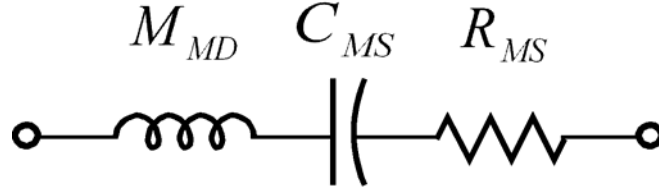
Figure 5.23. Equivalent mechanical impedance circuit for a drone cone termination.

Using this circuit, the loudspeaker acoustic impedance may be represented by

$$Z_{ATD} = R_{AS} + \frac{1}{j\omega C_{AS}} + j\omega M_{AD} \qquad (5.7)$$

$$= \frac{R_{MS}}{S_D^2} + \frac{1}{j\omega C_{MS} S_D^2} + \frac{j\omega M_{MD}}{S_D^2}, \qquad (5.8)$$

where a is the radius and S_D is the surface area of the diaphragm (πa_D^2) [12]. Table 5.1 is

a list of parameters used in the simulation of a drone cone termination.

Parameter	Value	Units
R_{MS}	0.5	kg/s
C_{MS}	750	μm/N
M_{MS}	75	g
S_D	0.0194	m^2

Table 5.1. Parameters used to model the drone cone termination.

Figure 5.24 shows the normalized real and imaginary parts of the acoustic impedance using the values from the table. The amplitude of the impedance above and below the passive radiator's resonance frequency (approximately 21 Hz) is controlled primarily by two separate mechanisms. Below this frequency, the impedance is stiffness-controlled. Above this frequency, and consequently for most of the audio bandwidth in this configuration, the impedance is mass-controlled. In this mass-controlled region (well

above the resonance frequency of 21 Hz) the imaginary part increases in proportion to frequency, while the real part remains very small.
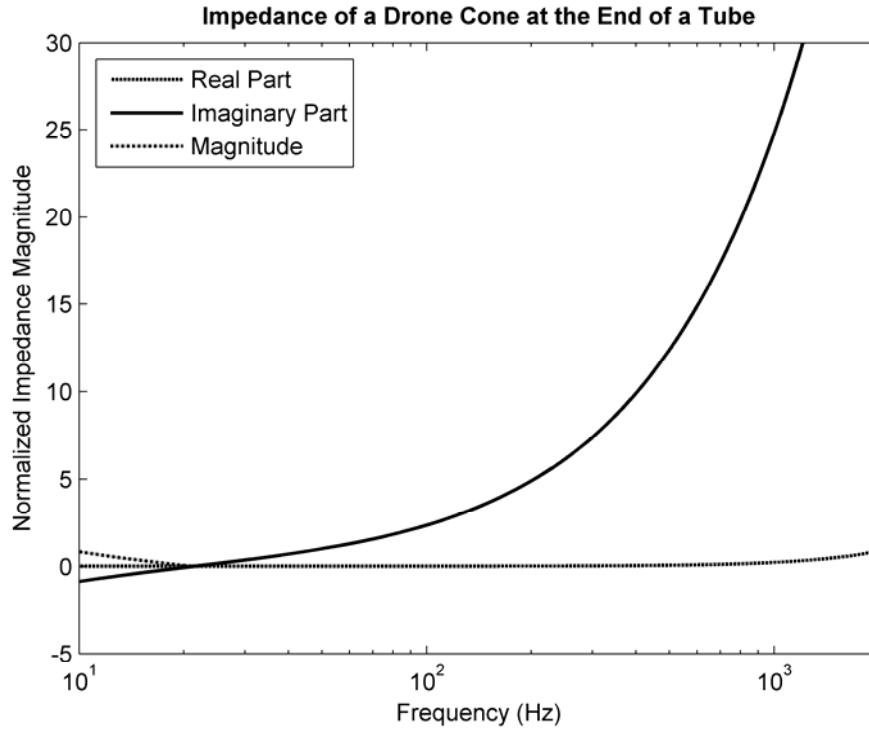
Figure 5.24. Normalized impedance plot for a drone cone termination. The solid trace is the imaginary part and the dotted trace is the real part.

To get a better idea of what this impedance plot means, it is useful to explore the characteristics of the reflection coefficient R produced by the drone cone [18]:

$$R = \frac{Z_{ATD} - \dfrac{\rho_0 c}{S}}{Z_{ATD} + \dfrac{\rho_0 c}{S}}. \tag{5.9}$$

The result is plotted in Fig. 5.25. It is clear that at most frequencies, the drone cone acts much like a rigid termination. This makes sense, seeing that at high

frequencies, the mass of the diaphragm would present a large impedance barrier to the wave front.

Reflection Coefficient for the Drone Termination
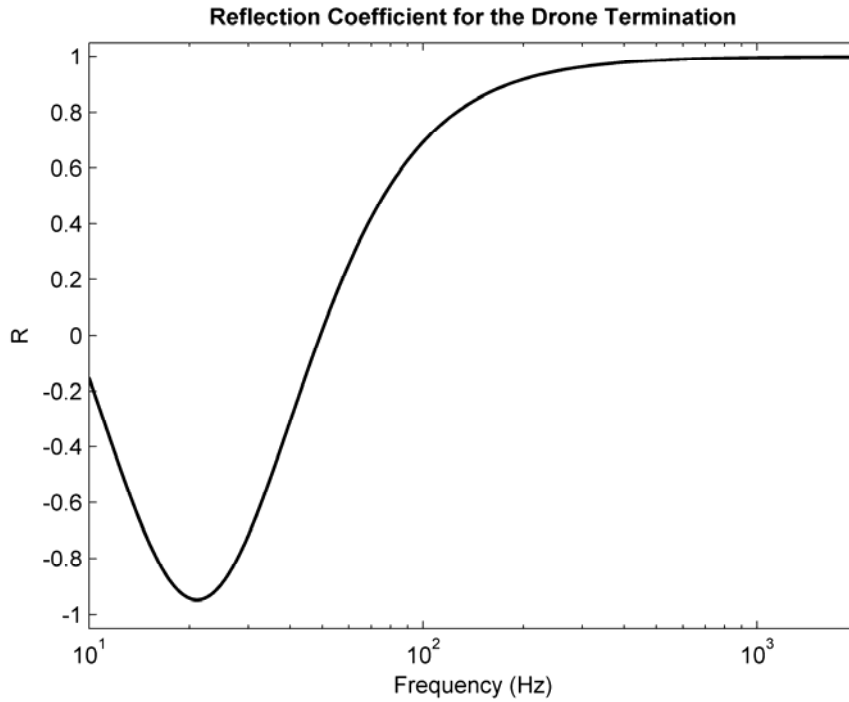
Figure 5.25. Reflection coefficient for a drone cone termination.

On the other hand, the driver is a damped mass-spring system and therefore has a well-defined resonance frequency at 21 Hz. At that frequency, the diaphragm will be set in motion and a portion of the impinging wave front will be readily absorbed. This resonance can be seen as a small dip in the reflection coefficient.

The input impedance and beamwidth curve of the shotgun tube terminated with the drone cone described in Table 5.1 are shown in Figs. 5.26 and 5.27, respectively. Both of these figures look very similar to those for the rigidly terminated model. This is to be expected since the reflection coefficient for the drone cone is nearly 1 at all frequencies, corresponding to a nearly rigid termination.

81
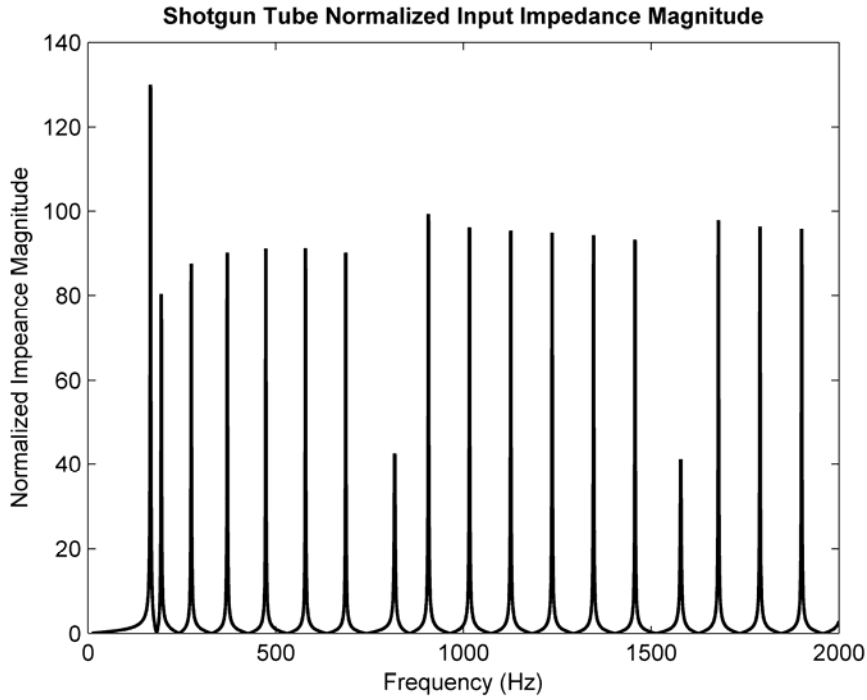
Figure 5.26. Normalized input impedance magnitude for a tube with a drone cone termination. This model has 6 holes spaced at 22 cm, a 1.27 cm hole radius, and a 5.08 cm tube radius.
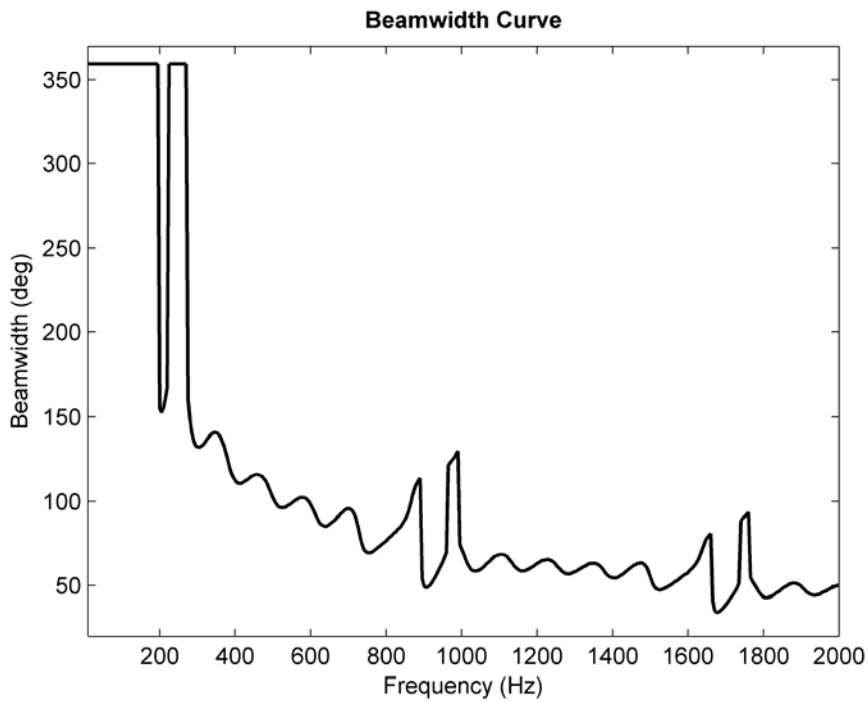
Figure 5.27. Beamwidth curve for a tube with an drone cone termination. This model has 6 holes spaced at 22 cm, a 1.27 cm hole radius, and a 5.08 cm tube radius.

Figure 5.28 shows the volume velocity produced by each hole and at the drone cone. Since the diaphragm is free to vibrate, the radiation from it cannot be ignored. In the case of the open-ended tube, the volume velocity at the end was much higher than at any single hole, which significantly degraded the performance. The volume velocity produced by the drone cone (hole #7 in the plot), is on the order of that produced at the holes along the tube. This does not degrade the overall control of the polar pattern and the length of the array has been effectively increased. It therefore produces a small improvement in the beamwidth performance, as shown in Fig. 5.29.
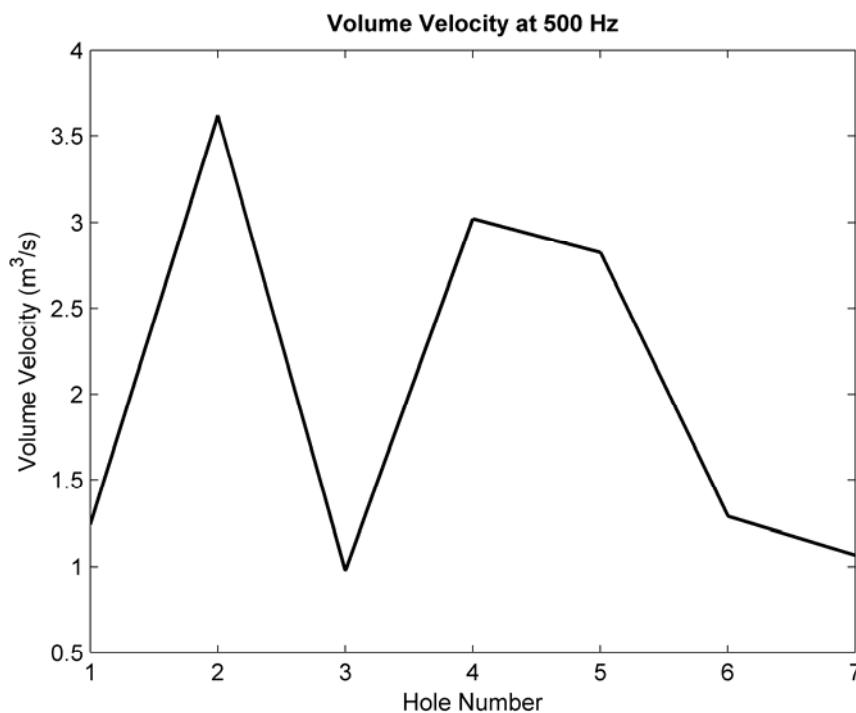
Figure 5.28. Volume velocity for the shotgun tube holes and drone cone termination at 500 Hz.
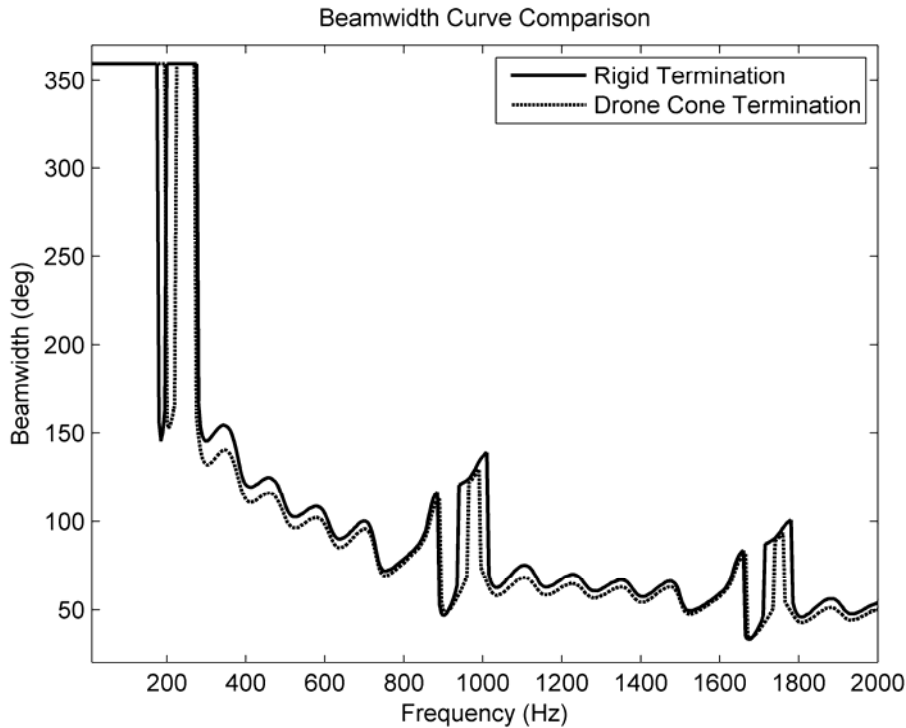
Figure 5.29. Beamwidth comparison between a rigid termination (solid trace) and drone cone termination (dashed trace).

5.6   Conclusions to be Drawn from this Analysis

We can conclude from Figs. 5.1 and 5.3 that the overall length of the array is the single most influential factor in the performance of the shotgun loudspeaker. The longer the tube, the better the performance (as evaluated by the beamwidth curves).   Other factors that improve performance were (1) an increased number of holes in the tube, (2) increased spacing between holes, (3) increased tube radius, and (4) decreased hole radii. In the practical sense, the latter two points have limits. As the tube radius increases, the cutoff frequency above which the first cross mode propagates decreases [as given in Eq. (5.1)]. A balance between desired bandwidth and directivity performance must be found in the design process.   Second, as the hole radius decreases, the particle velocity

84

increases. If the velocity is increased too much, vent noise will rise, which causes undesirable distortion. In addition to increased vent noise, a small hole radius will also reduce the efficiency of the device due to reduced radiated sound power from each hole. This will be discussed further in Chapter 8.

Finally, an anechoic termination clearly delivers the best performance when compared with other possible terminations discussed in this chapter. The tradeoff is that an anechoic wedge needs to be on the order of ¼ the largest wavelength of interest. In other words, in order for the termination to be completely anechoic down to 200 Hz, the wedge must be approximately 0.46 m long. This can prove to be a problem for many commercial applications where space is at a premium.

CHAPTER 6

PROTOTYPE DESIGN AND MEASUREMENT RESULTS

In order to validate the results from the computational model, two prototypes with different properties were made for the purpose of comparison. This chapter discusses their design, measurement procedures and basic measurement results.

6.1   Physical Characteristics of the Prototypes

The characteristics of the two prototypes were chosen for reasonable variation of the tube parameters. Table 6.1 provides their key properties.

Variable	Tube #1	Tube #2
Hole Radius	1.27 cm	0.635 cm
Tube Radius	5.08 cm	5.08 cm
Number of Holes	6	8
Hole Spacing	22 cm	11.85 cm
Tube Length	1.54 m	1.07 m

Table 6.1. List of tube parameters for each prototype.

The tube radius was the only parameter that was shared between the two prototypes. It allowed a convenient sharing of the same terminations and sources. Each tube was made from ABS tubing. The holes were drilled along one side according to the parameters given in the table.

6.2   Source

The source for the tubes was a small loudspeaker driver mounted in a damped sealed box (see Fig. 6.1). The driver was measured by a MLSSA system to extract the Theile/Small (T/S) parameters given in Table 6.2. The parameters describe the electrical and mechanical behavior of the driver and allow complete loudspeaker systems to be modeled using equivalent circuit techniques.
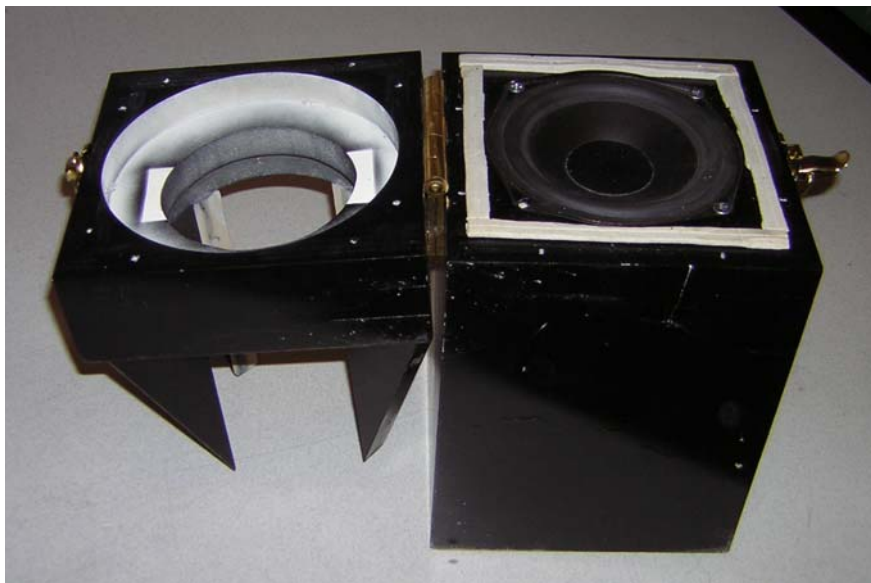
Figure 6.1. Shotgun tube source.

Parameter	Value	Units
R_e	5.42	Ohms
L_1	0.152	mH
L_2	0.488	mH
R_2	16.5	Ohms
Q_{MS}	3.03	--
C_{MS}	482.8	μm/N
M_{MS}	9.66	g
F_s	73.7	Hz
Bl	6.59	Tm

Table 6.2. List of T/S parameters for the loudspeaker model.

6.3   Terminations

Two termination conditions were tested in the prototypes. An ABS cap was used at the end of the tubes to act as a rigid termination. A small foam wedge was also placed at the end of the tube in front of the cap to approximate an anechoic condition at higher frequencies. The foam wedge is shown in Fig. 6.2.

Figure 6.2. Foam wedge placed in the end of the tubes to give an anechoic termination. The ruler at the bottom of the figure is marked in centimeters.

The ABS cap and the foam wedge were each placed at the end of an impedance tube and the reflection and absorption coefficients were measured. The absorption coefficients are shown in Figs. 6.3 and 6.4. Appendix A discusses in detail how these measurements were performed and how the variables were extracted from the measured data.

88
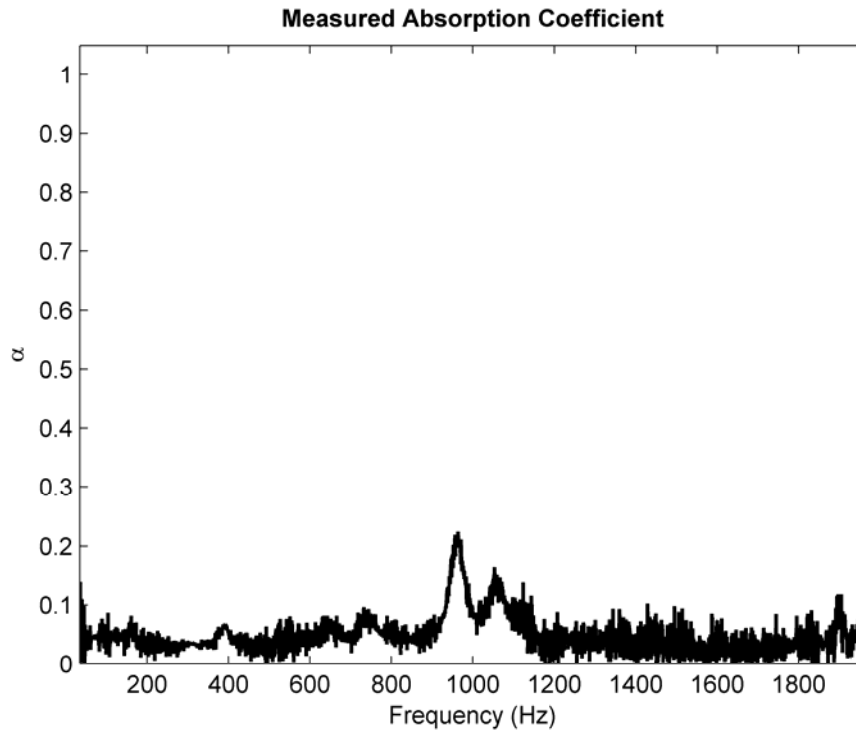
Figure 6.3. Absorption coefficient for the rigid termination.
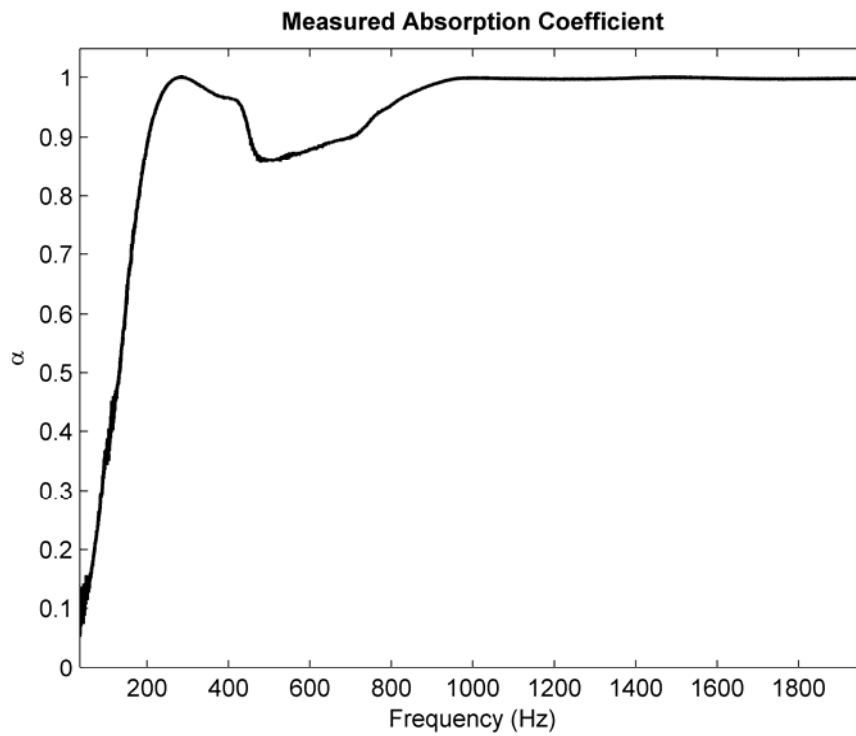
Figure 6.4. Absorption coefficient for the anechoic termination.

As is clear from these figures, neither the wedge nor the ABS cap performs perfectly. Ideally, the rigid cap would have an absorption coefficient of zero and the wedge would be equal to one. To a first approximation, the terminations suffice. In Chapter 7 their imperfections are taken into account in the numerical model.

6.4   Measurement Setup and Procedure

Figures 6.5 and 6.6 show the fully assembled long and short prototypes, respectively. Once completed, each device was placed on a stand made specifically for the tubes, which was then mounted on a computer-controlled turntable and placed in an anechoic chamber, as shown in Fig. 6.7. As can be seen in this figure, the geometric center of the tube coincides with the center of the turntable. This point on the tube was taken as the acoustic center of rotation of the system as defined in previous related work [7, 8, 11].

Figure 6.5. Fully assembled long prototype (tube #1 from Table 6.1).
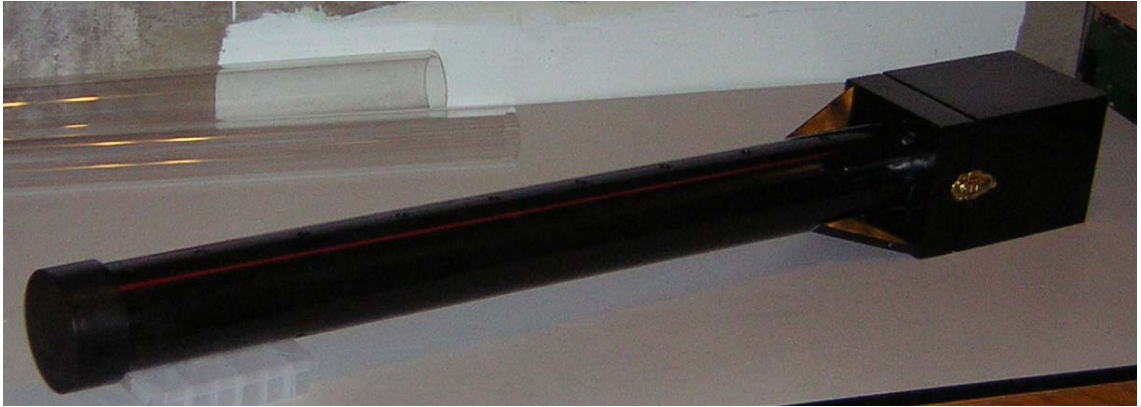
Figure 6.6. Fully assembled short prototype (tube #2 from Table 6.1).
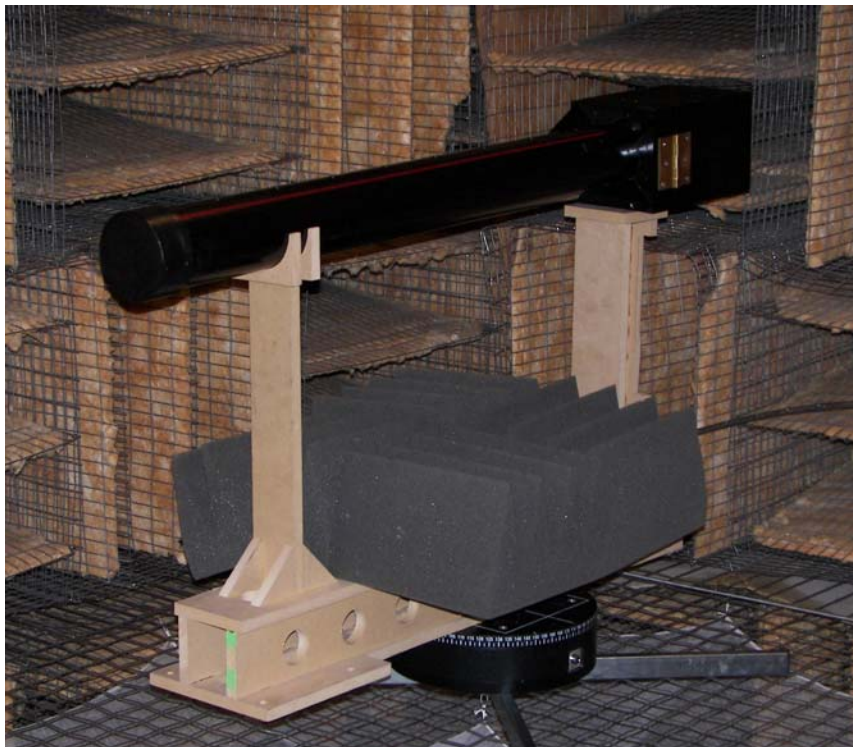
Figure 6.7. Measurement setup in the anechoic chamber.

A type 1 PCB 377A02 microphone and Larson Davis PRM426 ICP preamplifier were placed approximately four meters away from the center of the turntable at a height that was equal to the height of the holes in the tube. The tube was rotated in angular steps of 5 degrees and excited with pseudorandom broadband noise. At each position, the Data Physics dynamic signal analyzer shown in Fig. 6.8 calculated the transfer function between the input signal to the loudspeaker and the output signal from the microphone.

Figure 6.8. Data Physics dynamic signal analyzer.

This same measurement procedure was performed on both the short and long prototypes, with both the rigid and anechoic termination conditions. The data was saved and post-processed in MATLAB where the beamwidth and frequency response of each prototype was calculated. The results are given in the following section.

6.5   Measurement Results and Comparison

Once the data was collected, the beamwidth was calculated for all frequencies over the measurement bandwidth from 10 Hz to 2 kHz in 5 Hz increments. Figures 6.9 through 6.12 show the measured beamwidth curves, along with their numerical predictions.
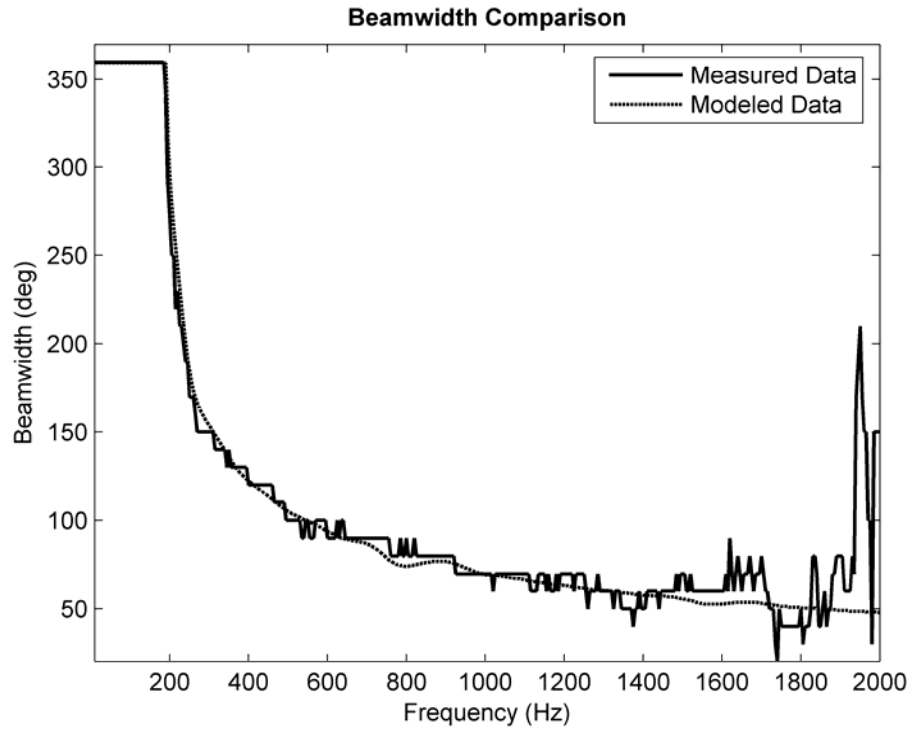
Figure 6.9. Beamwidth curve comparison for the long prototype and an anechoic termination. The solid trace is the measured data and the dashed trace is the predicted data.
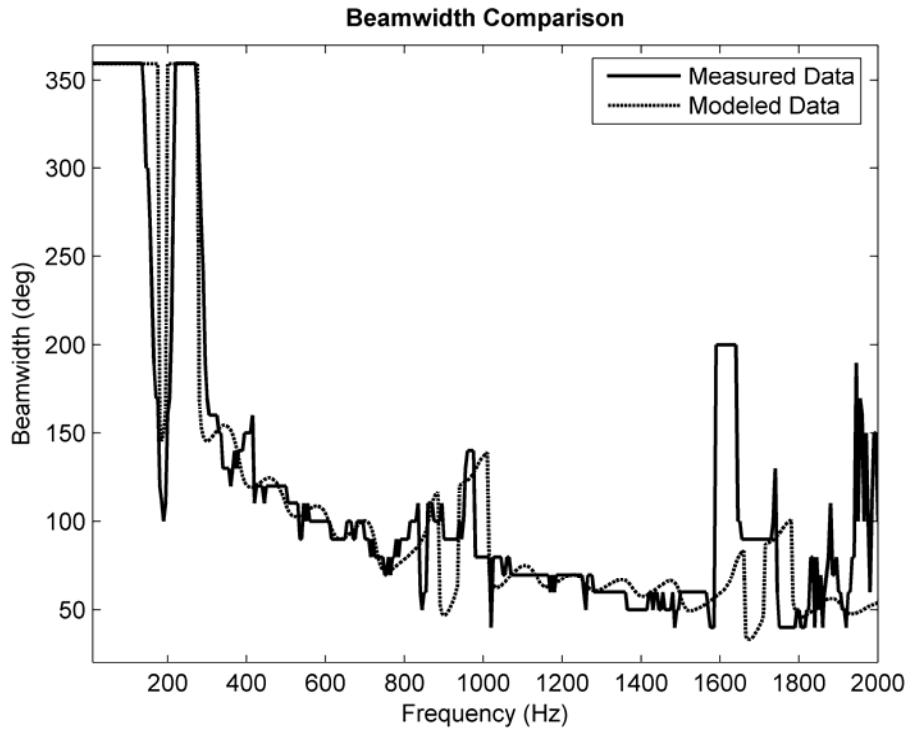
Figure 6.10. Beamwidth curve comparison for the long prototype and a rigid termination. The solid trace is the measured data and the dashed trace is the predicted data.
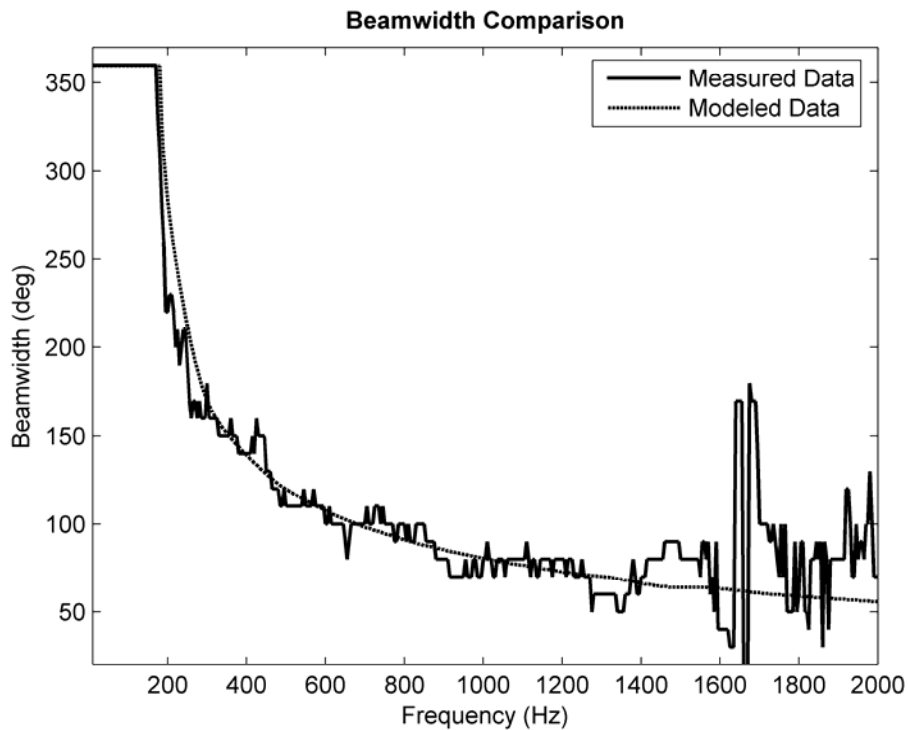
Figure 6.11. Beamwidth curve comparison for the short prototype and an anechoic termination. The solid trace is the measured data and the dashed trace is the predicted data.
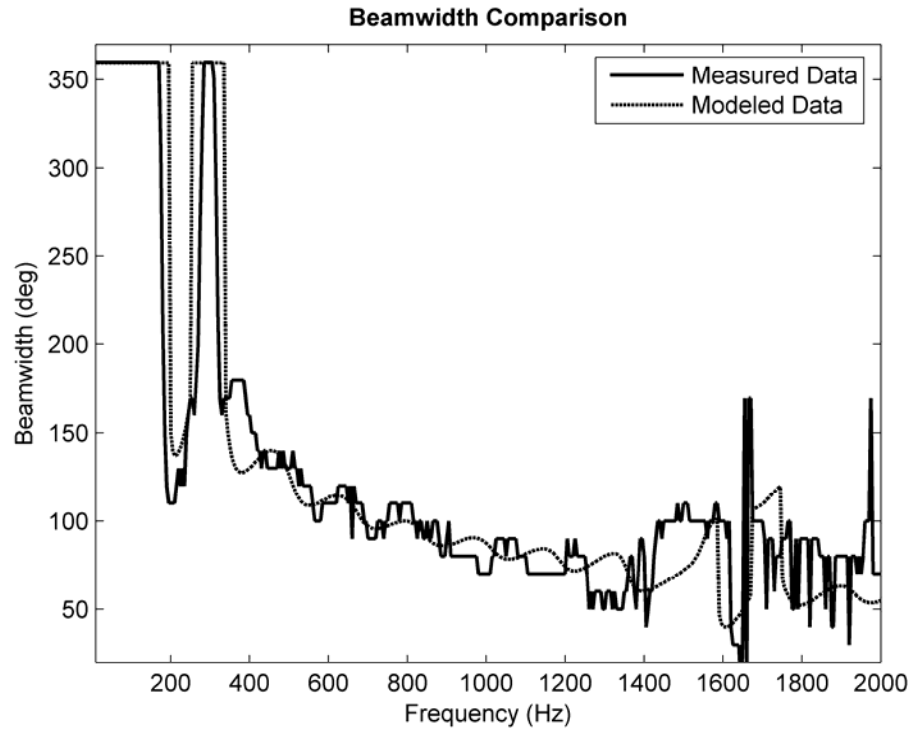
Figure 6.12. Beamwidth curve comparison for the short prototype and a rigid termination. The solid trace is the measured data and the dashed trace is the predicted data.

It is clear from the figures that there is good agreement between the measured and the modeled data. The discussion in Chapter 5 indicated that the plane wave assumption in the tube would break down at approximately 1950 Hz. This is supported by the divergence from the modeled data in all four plots near this frequency.

To look more closely at the radiated sound fields, a few polar patterns for each termination condition are plotted in Figs. 6.13 through 6.18. The frequencies 200, 800, and 1200 Hz were selected to show a wide range of radiation patterns. The first is in the omnidirectional frequency range, the second is where the rear lobe begins to grow due to the spatial aliasing discussed in the previous chapter, and the last shows the mirrored rear lobes that are being slowly steered away from the back of the tube. The amplitude of the

95

modeled data is not valid given that the source in this model is simply a constant value over frequency assigned to a volume velocity input. In the figures, the amplitude was chosen to be comparable to that seen in the measured data. The shape of the polar patterns is the important thing to notice. It is again clear that there is good agreement between the modeled and measured data.
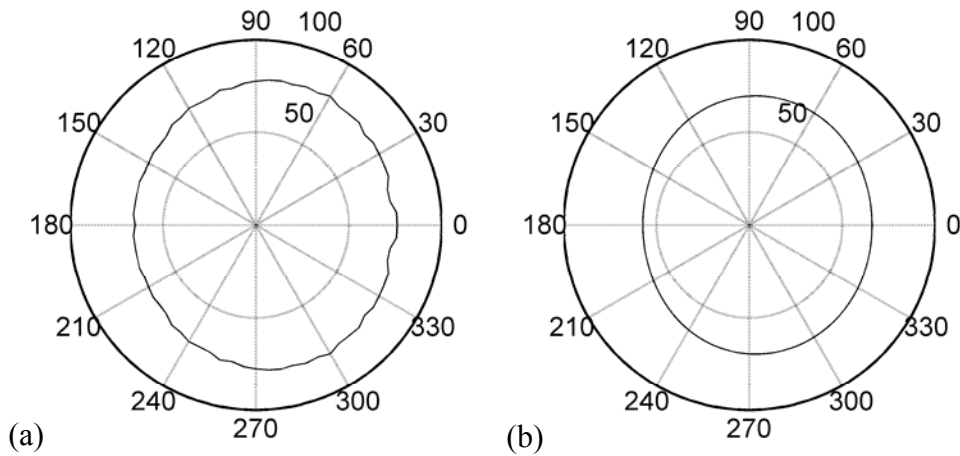
Figure 6.13. Polar pattern comparison for the long tube with an anechoic termination at 200 Hz. (a) Measured data. (b) Modeled data.
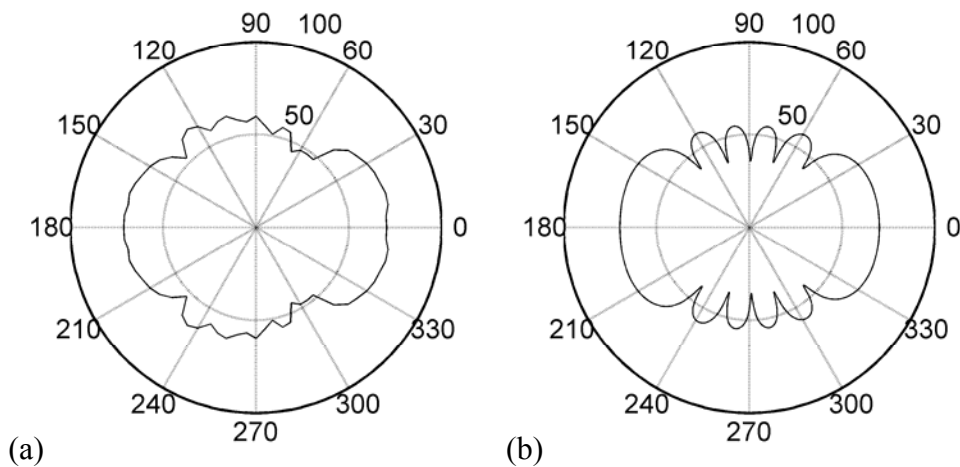
Figure 6.14. Polar pattern comparison for the long tube with an anechoic termination at 800 Hz. (a) Measured data. (b) Modeled data.
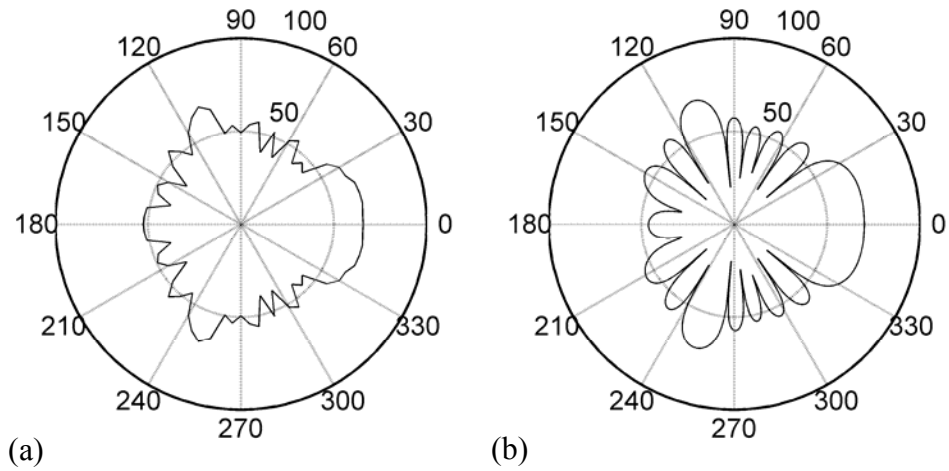
Figure 6.15. Polar pattern comparison for the long tube with an anechoic termination at 1200 Hz. (a) Measured data. (b) Modeled data.
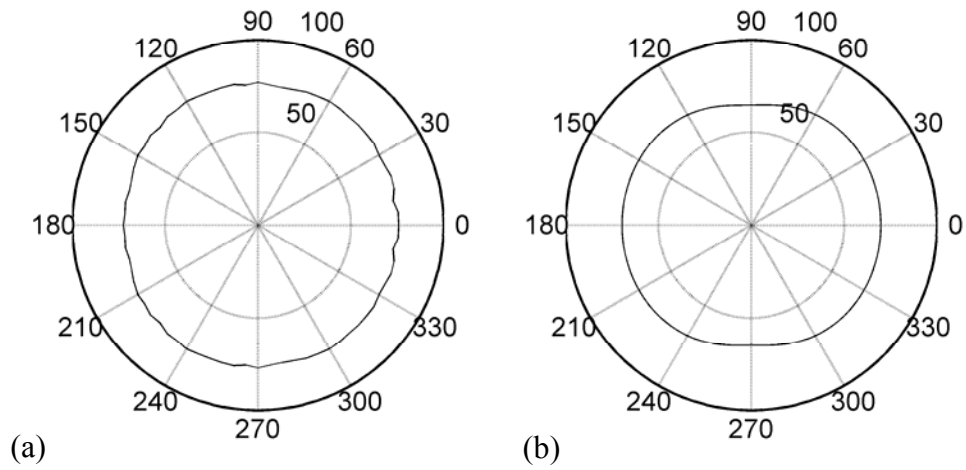
Figure 6.16. Polar pattern comparison for the long tube with a rigid termination at 200 Hz. (a) Measured data. (b) Modeled data.
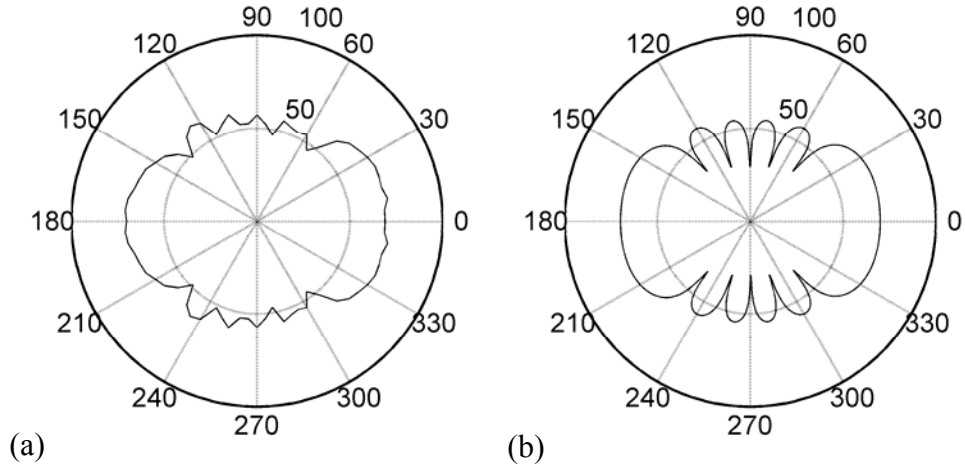
Figure 6.17. Polar pattern comparison for the long tube with a rigid termination at 800 Hz. (a) Measured data. (b) Modeled data.
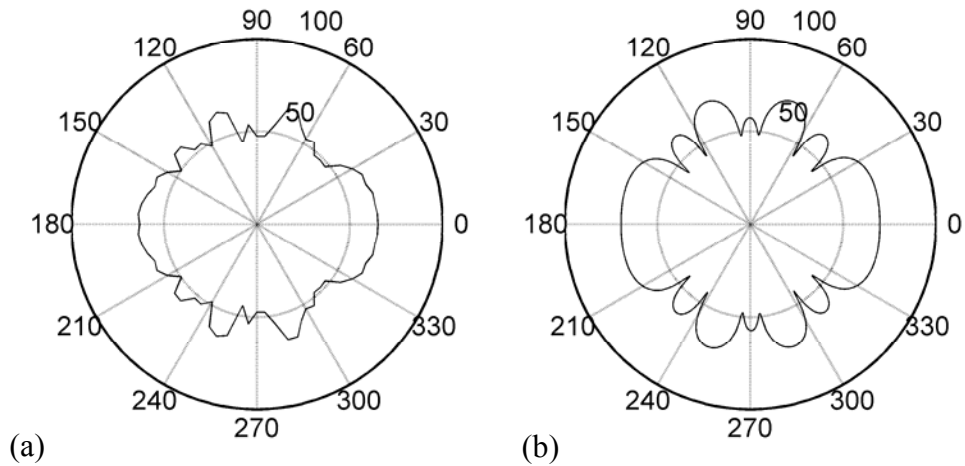
Figure 6.18. Polar pattern comparison for the long tube with a rigid termination at 1200 Hz. (a) Measured data. (b) Modeled data.

Another noteworthy point is the on-axis frequency response of the shotgun loudspeaker in the far field. In Figures 6.19 and 6.20, the on-axis response is shown for the long prototype with the anechoic and rigid terminations, respectively. Again, the

modeled amplitude is ambiguous and is merely the result of using a constant for the volume velocity input to the system. However, the shape of the curves can still be compared.

In the measured data, there seems to be a downward slope at the higher frequencies that is not accounted for in the model. Many of the peaks in the measured results appear to show up in the model, but they are shifted slightly in frequency, which gives us confidence that our model is performing reasonably well for the limited information it has to work with. In the next chapter, many improvements to the numerical model are suggested, their effects discussed, and a comparison to the measured data is again carried out.
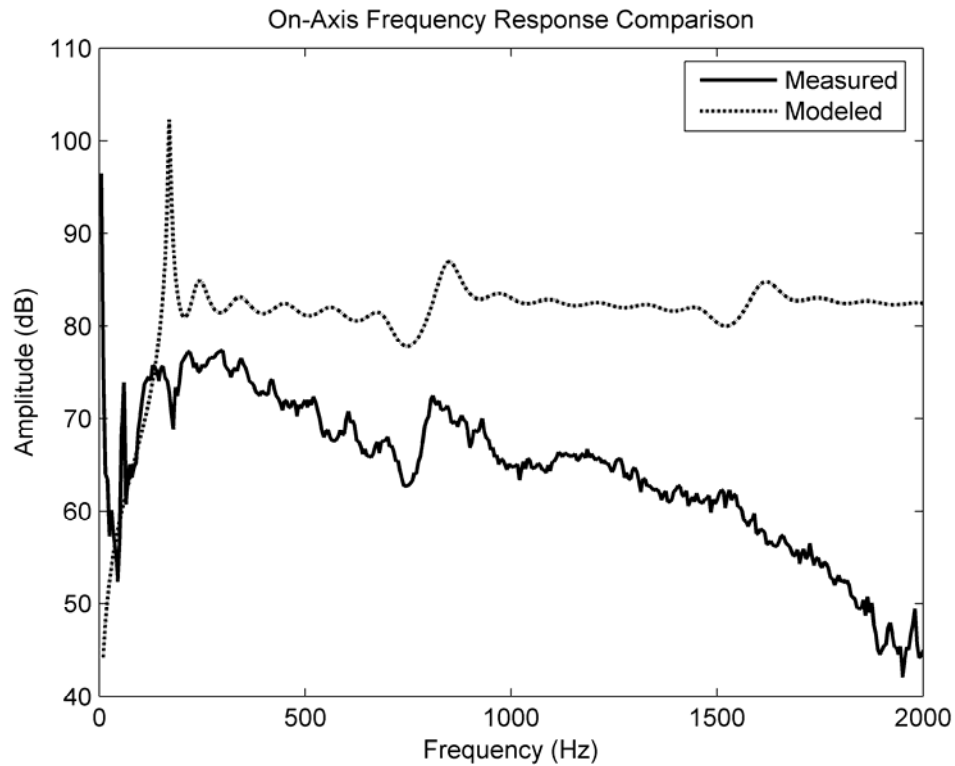
Figure 6.19. On-axis frequency response of the long prototype with an anechoic termination. The solid trace is the measured response and the dashed trace is the modeled response.
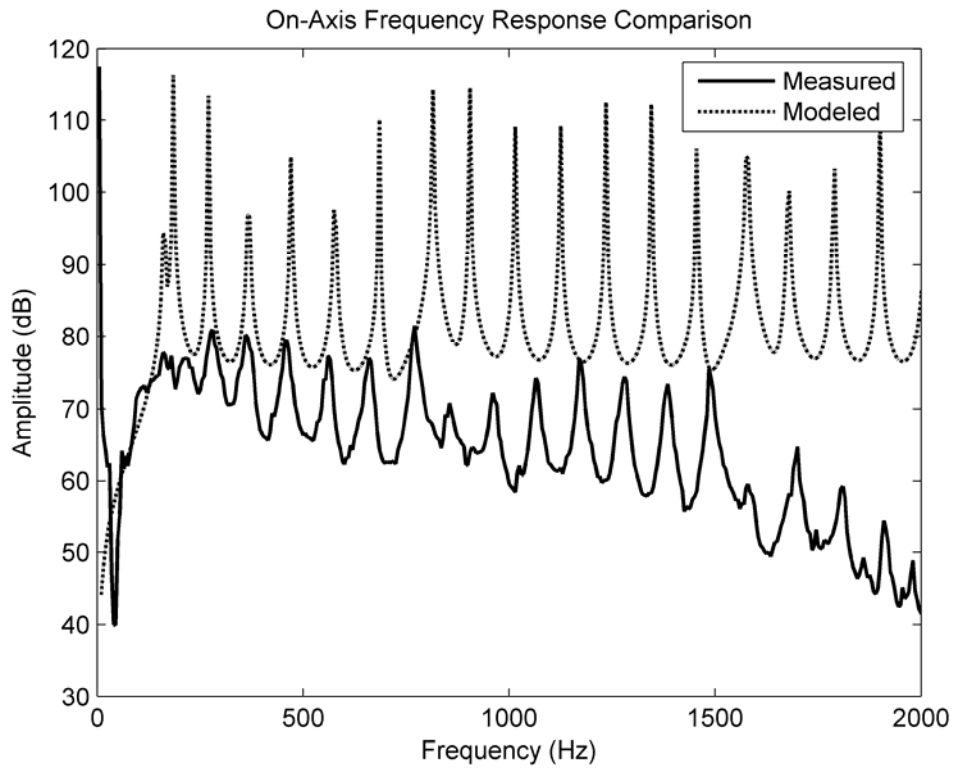
Figure 6.20. On-axis frequency response of the long prototype with a rigid termination. The solid trace is the measured response and the dashed trace is the modeled response.

CHAPTER 7

NUMERICAL MODEL IMPROVEMENTS

While Chapter 6 showed that the original computational model provided reasonable agreement with the prototype measurements, several improvements to the model could increase its accuracy so as to represent the system even better. This chapter describes these improvements, showing how they affect the model results, then compares the newly modeled data to the measured data.

7.1   Losses in the Tube

The classical absorption coefficient for propagation, which is the sum of the viscous and thermal absorption coefficients, can be written as [10]

$$\alpha_c = \frac{\omega^2 \eta}{2\rho_0 c^3}\left(\frac{4}{3} + \frac{\gamma - 1}{P_r}\right),$$
(7.1)

where η is the coefficient of shear viscosity, γ is the ratio of specific heats, and P_r is the Prandtl number. The latter defined as

$$P_r = \frac{\eta c_p}{\kappa},$$
(7.2)

where c_p is the specific heat for constant pressure and κ is the thermal conductivity. It can also be shown that losses at the tube wall due to boundary layer viscosity and thermal conduction can be given as [10]

$$\alpha_w = \frac{1}{a_t c}\sqrt{\frac{\eta \omega}{2\rho_0}}\left(1 + \frac{\gamma - 1}{\sqrt{P_r}}\right),$$
(7.3)

where a_t is the radius of the tube. These expressions can be summed simultaneously to account for both types of losses in the tube:

$$\alpha_T = \alpha_c + \alpha_w \qquad (7.4)$$

The constants used in the calculations are given in Table 7.1.

Parameter	Value	Units
η	$1.85\text{x}10^{-5}$	Pa*s
κ	0.0263	W/m*K
c_p	$1.01\text{x}10^3$	J/kg*K
γ	1.402	--
c	343	m/s
ρ_o	1.21	kg/m^3

Table 7.1. Values for absorption loss calculations.

The wavenumber can then be written in complex form to account for the losses:

$$\tilde{k} = k - j\alpha_T . \qquad (7.5)$$

A complex sound speed $\tilde{c}$ then follows as

$$\tilde{c} = \frac{\omega}{\tilde{k}} . \qquad (7.6)$$

Figure 7.1 shows how the magnitude of the speed of sound changes over frequency. The x-axis is shown here on a log scale to exaggerate the curve. As frequency increases, the value for $\tilde{c}$ asymptotically reaches the standard value of 343 *m/s* used in the original model. A close look at the y-axis shows that even at the lowest frequencies, $\tilde{c}$ does not vary too far from its value of 343 *m/s*, so the effect on the resulting beamwidth curve is expected to be minimal.
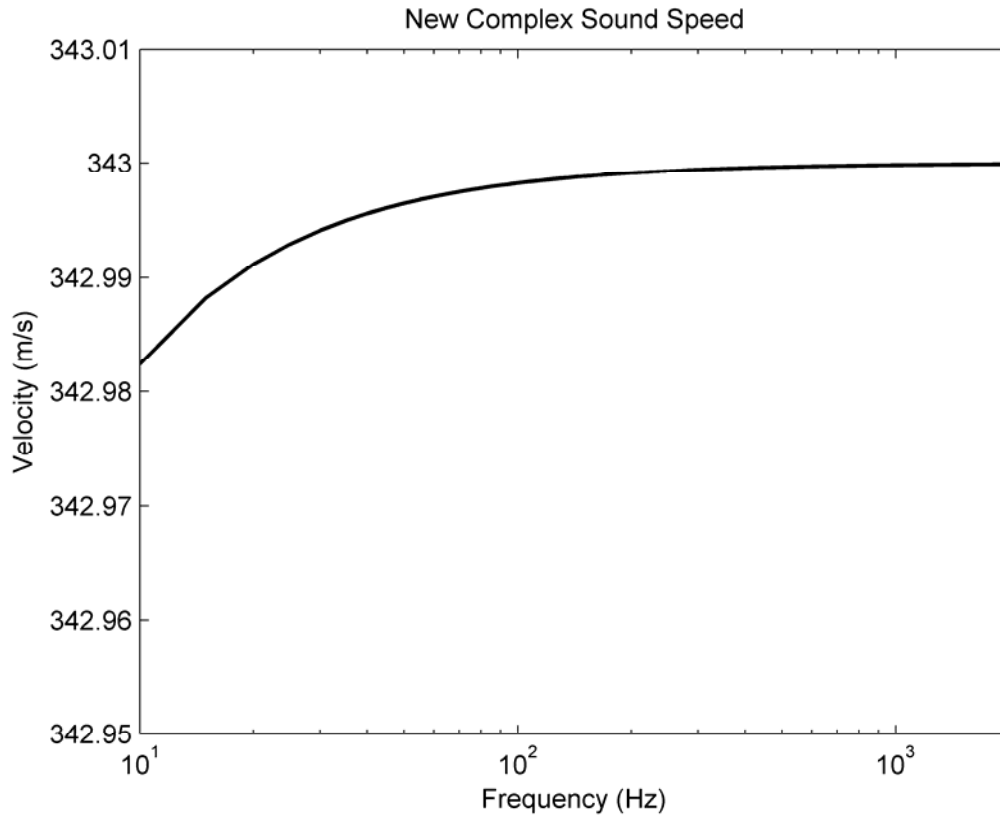
Figure 7.1. Magnitude of the new complex speed of sound, $\widetilde{c}$.

Figure 7.2 shows the beamwidth curve for the model revised for propagation losses, in comparison to the preliminary model. As anticipated, the two curves lie directly on top of each other and therefore no change is observed in the beamwidth curves. However, there is a small change in the on-axis frequency response as seen in Fig. 7.3. The losses result in a small downward trend as frequency increases.
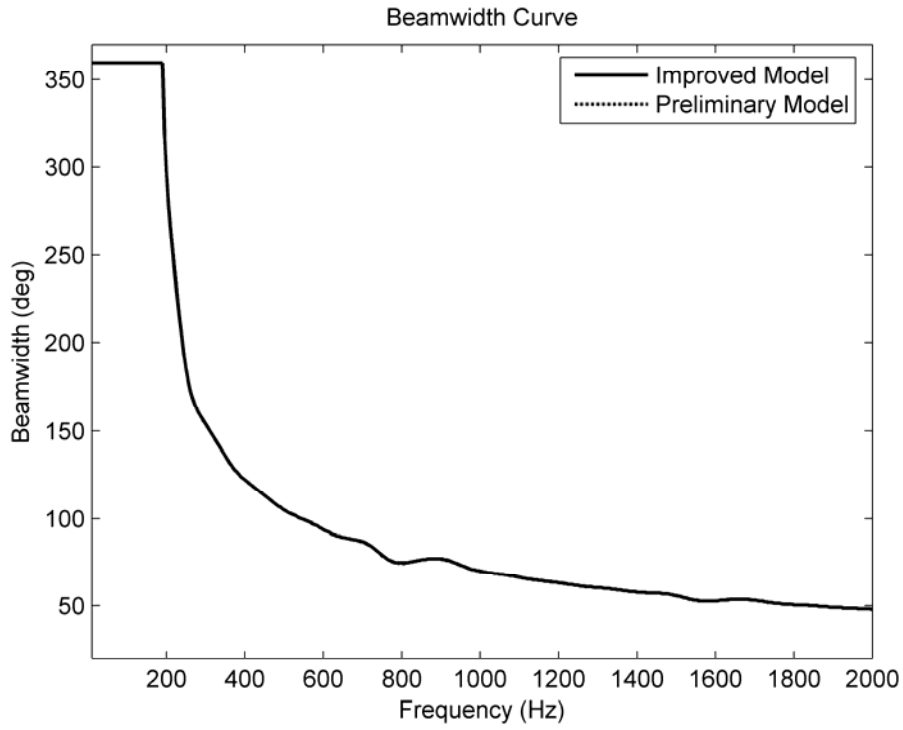
Figure 7.2. Beamwidth curve comparison to preliminary model.
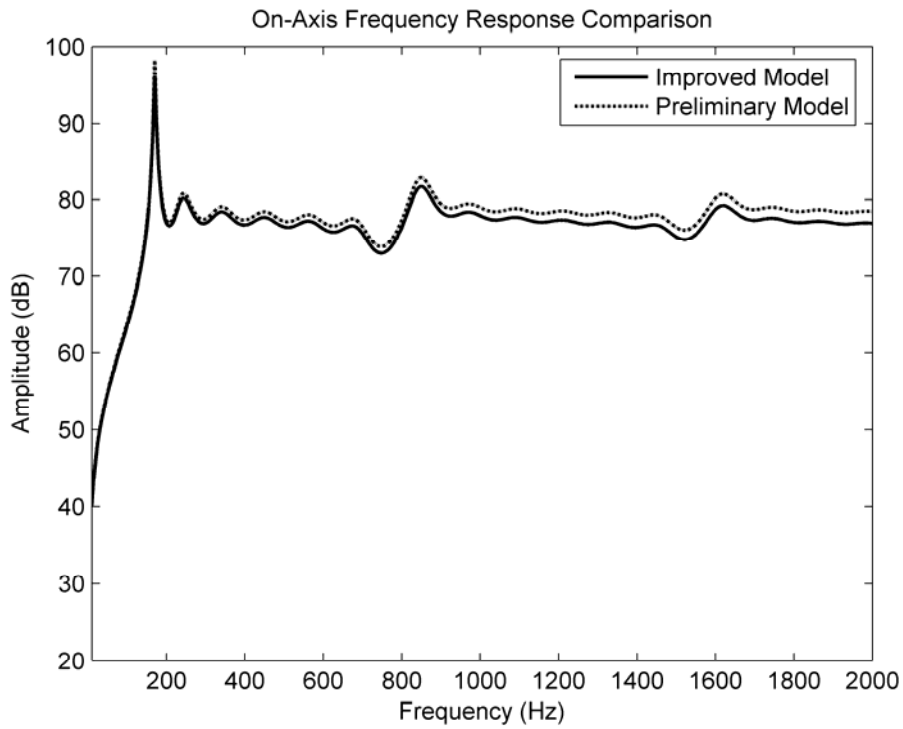
Figure 7.3. On-axis frequency response comparison to preliminary model.

7.2   New Source Model

Another improvement to the model results by representing the source loudspeaker with a complete equivalent circuit instead of as a constant volume velocity source. Figure 7.4 shows a low-frequency equivalent circuit for a loudspeaker in a sealed box radiating into free space [13]. It is represented in the acoustic impedance domain. The radiation terms, M_{AR} and R_{AR}, are the imaginary and real parts, respectively, of Z_{AR} (the acoustic radiation impedance seen by the driver diaphragm). The other elements of the circuit can be connected to the shotgun tube circuit to represent the loudspeaker coupled to the shotgun tube (see Fig. 7.5).
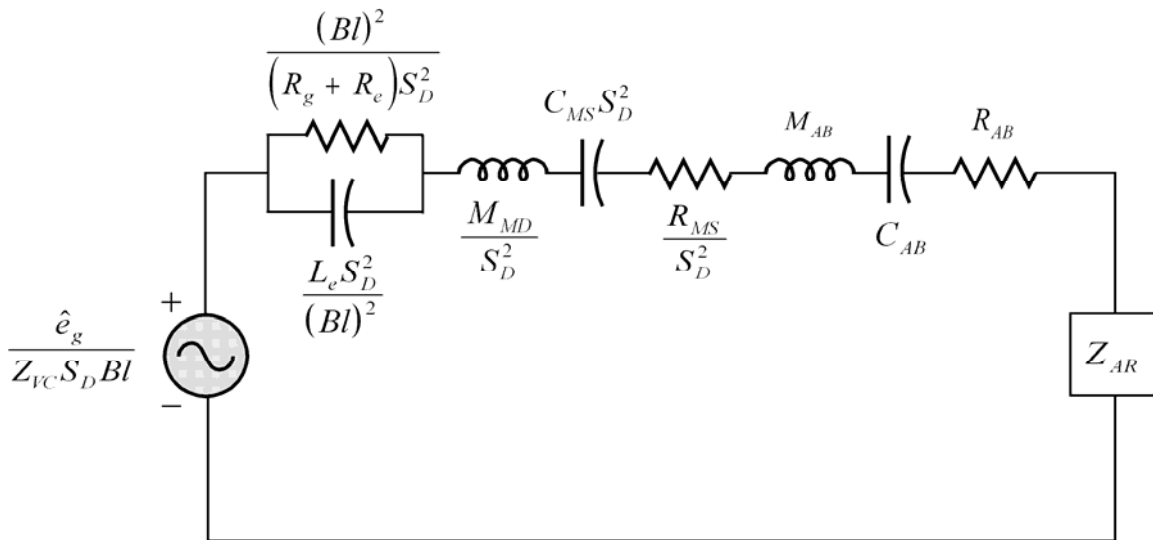
Figure 7.4. Equivalent acoustic impedance circuit for a loudspeaker.
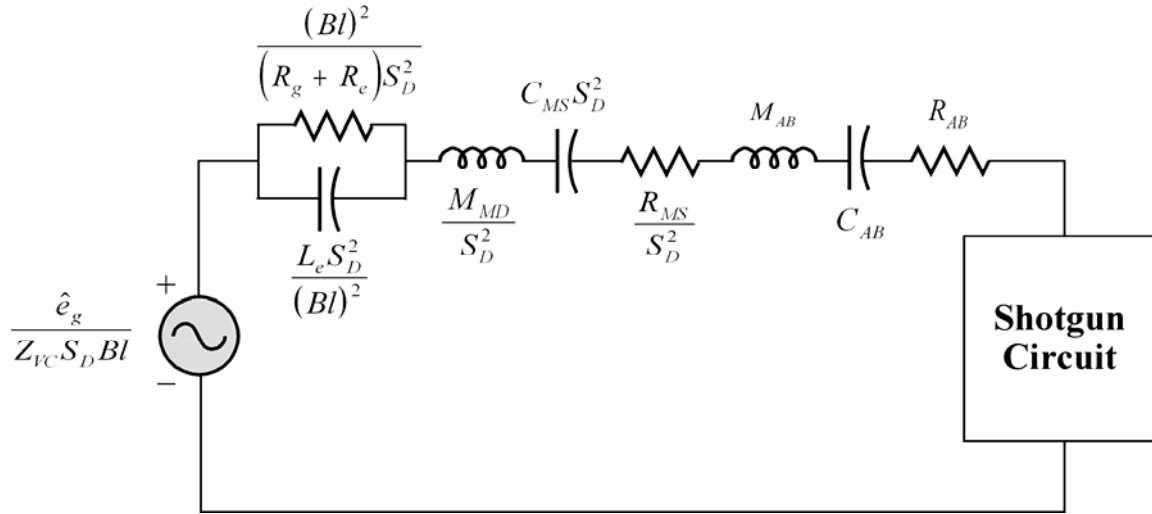
Figure 7.5. Equivalent acoustic impedance circuit for the loudspeaker coupled to a shotgun tube.

This type of circuit is typically only valid to approximately $10\omega_0$ (where ω_0 is the 3 dB down point as the low frequency response begins to roll off), or $\approx 1000 Hz$ in our case, but can give a good approximation to the acoustic system beyond this limit [12].

Table 7.2 is a list of the T/S parameters for the driver used in the prototypes and were measured using the MLSSA system. A value of 0.1 Ω for R_g is a common output impedance for many signal generators and power amplifiers.

Parameter	Value	Units
R_e	5.42	Ohms
L_e	0.152	mH
Q_{MS}	3.03	--
C_{MS}	482.8	μm/N
M_{MS}	9.66	g
F_S	73.7	Hz
Bl	6.59	Tm

Table 7.2. List of the T/S parameters used in the loudspeaker model. The driver was supplied by Soundtube Entertainment.

Using this circuit, we can solve for the acoustic input impedance at the loudspeaker terminals and use the following relation to find the electric input impedance Z_{EI}:

$$Z_{IE} = Z_{VC}(Bl)^2 + \frac{(BL)^2}{S_D^2 (Z_{AI} - Z_{A,VC})} - R_g, \tag{7.7}$$

where Z_{VC} is electric impedance of the voice coil elements, $Z_{A,VC}$ is the acoustic impedance of the voice coil element, and Z_{AI} is the acoustic input impedance.

Figure 7.6 shows the modeled electric input impedance of the loudspeaker radiating into free-space as the dashed trace. It has the characteristic single peak for a sealed enclosure system and shows a slowly rising impedance in the high frequency region due to the inductance of the voice coil.
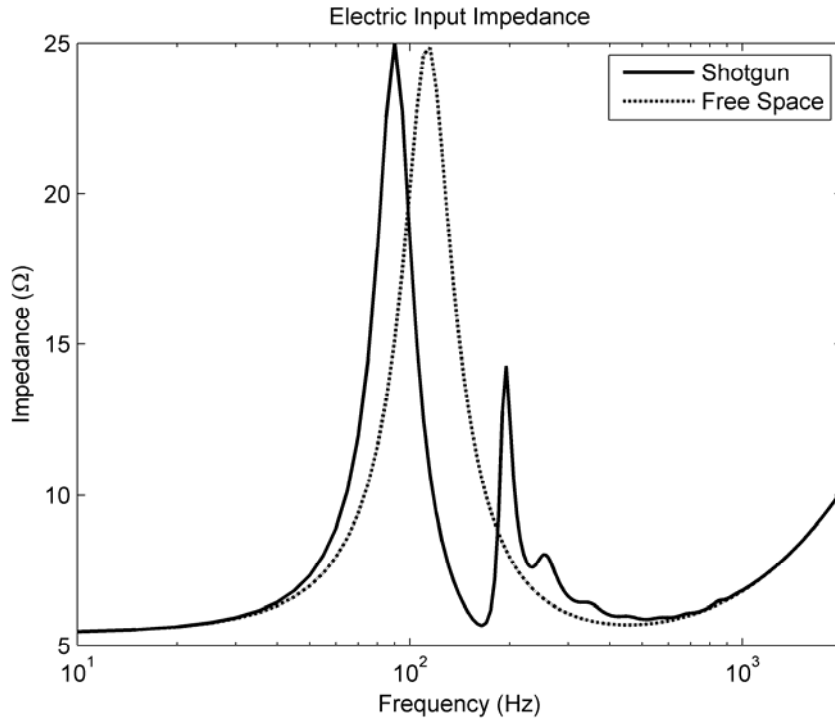
Figure 7.6. Electric input impedance comparison for the loudspeaker radiating into free space (dashed trace) and into a shotgun tube (solid trace).

The solid trace is the modeled electric input impedance for the same loudspeaker radiating into a shotgun tube with 6 holes, 5.08 cm tube radius, 22 cm hole spacing, 1.27 cm hole radius, and an anechoic termination. The main peak has been shifted down due to mass loading on the driver and an additional peak shows up at approximately 200 Hz. The latter corresponds to the resonance frequency found for the hole air masses resonating with the volume of air inside the tube per hole. The smaller peaks above this are due to other tube resonances as seen in previous tube acoustic input impedance plots.

Using the circuit, we can solve for the volume velocity into the tube assuming a given voltage as an input to the loudspeaker terminals. To simplify the derivation, we split the circuit into sections and find the acoustic impedance of each portion. First, the acoustic impedance associated with the loudspeaker motor (voice coil) is

$$Z_{A,VC} = \left[\frac{S_D^2 (R_g + R_e)}{Bl^2} + \frac{S_D^2 Bl^2}{j\omega L_e} \right]^{-1}. \tag{7.8}$$

The loudspeaker's mechanical system may be represented by

$$Z_{A,D} = R_{AS} + \frac{1}{j\omega C_{AS}} + j\omega M_{AD}, \tag{7.9}$$

$$= \frac{R_{MS}}{S_D^2} + \frac{1}{j\omega C_{MS} S_D^2} + \frac{j\omega M_{MD}}{S_D^2}. \tag{7.10}$$

where M_{MD} is defined as

$$M_{MS} - \frac{8}{3}\rho_0 a^3. \tag{7.11}$$

Finally, the acoustic impedance of the enclosure may be expressed as [13]

$$Z_{A,B} = R_{AB} + \frac{1}{j\omega C_{AB}} + j\omega M_{AB}, \tag{7.12}$$

$$\approx R_{AB} + \frac{\rho_0 c^2}{j\omega V} + 0.3\left(\frac{j\omega\rho_0 a}{S_D}\right). \tag{7.13}$$

The total acoustic impedance of the system is simply the sum of all terms.

$$Z_A = Z_{A,VC} + Z_{A,D} + Z_{A,B} + Z_{AR}, \tag{7.14}$$

where Z_{AR} is the acoustic input impedance of the shotgun circuit developed earlier, as shown in Fig. 7.5. Finally, the volume velocity through the circuit can be represented by

$$\hat{U} = \left[\frac{\hat{e}_g}{S_d Z_{VC} Bl}\right]\left(\frac{1}{Z_A}\right), \tag{7.15}$$

where Z_{VC} is the electric impedance of the voice coil given as

$$Z_{VC} = \frac{R_g + R_e + j\omega L_e}{Bl^2}, \tag{7.16}$$

and $\hat{e}_g$ is the input voltage applied to the loudspeaker terminals.

Figure 7.7 shows the resulting volume velocity output from the loudspeaker model. The trace looks similar to the electric input impedance, which is common in loudspeaker design. The volume velocity was then imported into the shotgun tube model and the beamwidth curve was computed.

Figure 7.8 shows the results and compares it to the benchmark curve. Once again, the curve does not change at all. To explore why no change was observed, each hole was examined more closely. The individual volume velocities were of particular interest, seeing that $\hat{U}$ was the variable changed between models.
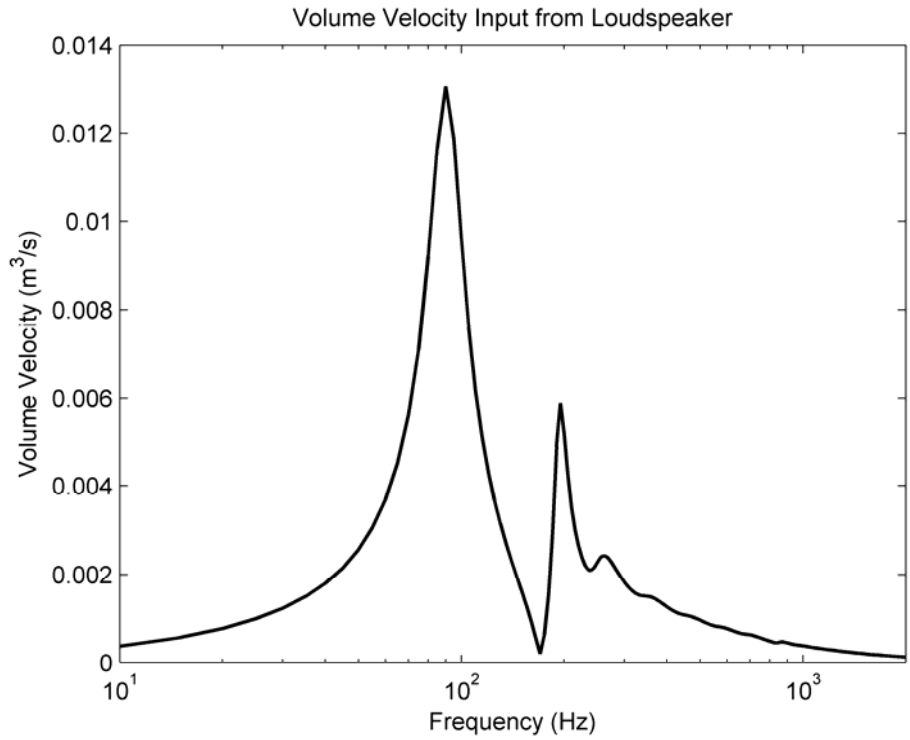
Figure 7.7. Volume velocity output from the loudspeaker into the shotgun tube.
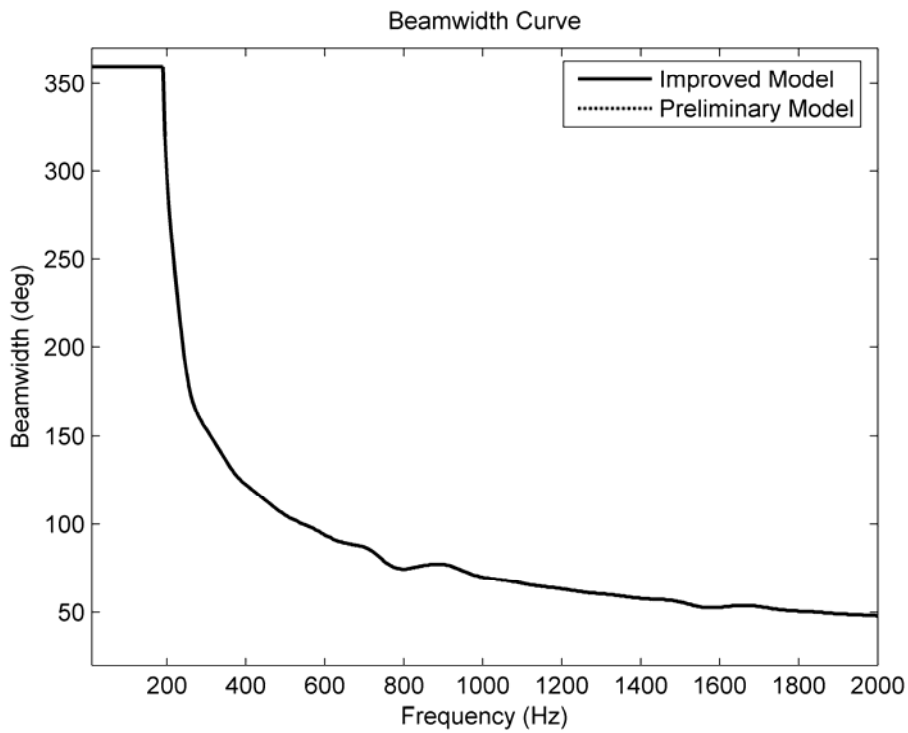
Figure 7.8. Beamwidth curve comparison to preliminary model.

110

Figure 7.9 shows the volume velocities at each hole for the two different simulations where a constant value was used for the input, as opposed to calculating the volume velocity directly through the loudspeaker model. The curves appear to be quite different, but if the ratio of the velocities at each hole is calculated, it is a constant 13.5 for all holes. A simple scale factor was found for any and all inputs. In other words, no matter what the input, the ratio of velocities along the tube (or the shape of the curve as shown in Fig. 7.9) stays constant. This results in the same beamwidth curve for all simulations within reasonable limitations.
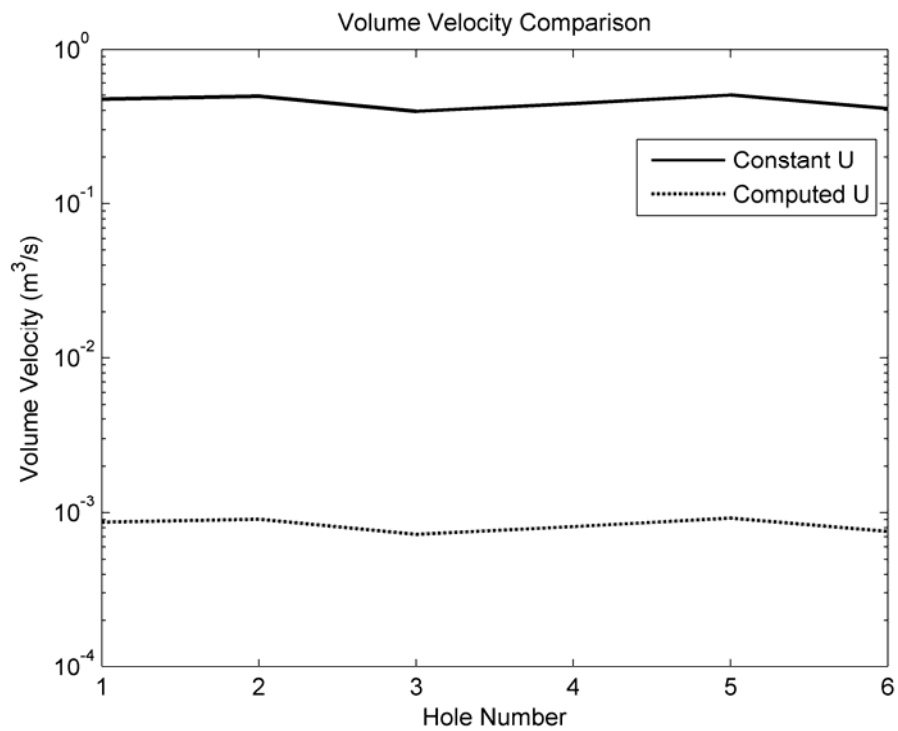
Figure 7.9. Volume velocity comparison to preliminary model.

A more promising improvement in its new analytical model is the ability to better predict the on-axis frequency response of the device. Figure 7.10 shows the comparison between the preliminary model and the improved model. There is a well-defined downward slope to the new modeled response that looks very similar to that seen in the measured data of Chapter 6.
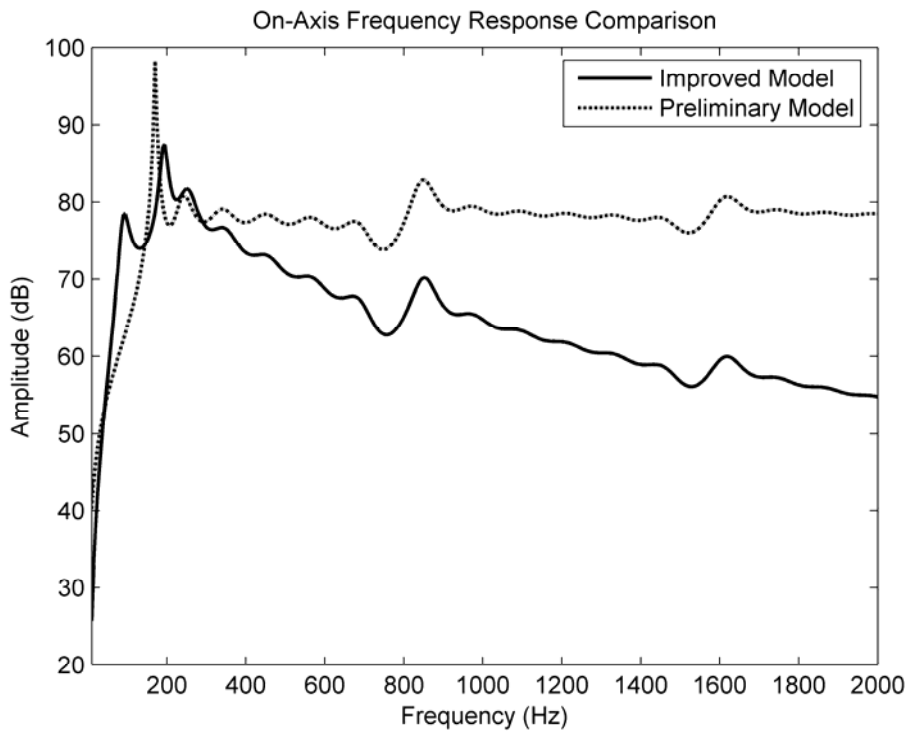
Figure 7.10. On-axis frequency response comparison to preliminary model.

7.3 Air Gap Compensation

Mounting the loudspeaker directly to the shotgun tube presented a minor problem when fabricating the prototypes. The final design had a small gap between the driver diaphragm and the beginning of the tube. Figure 7.11 provides a diagram of the design.

As previously mentioned, a waveguide circuit can be used to model a section of tube with a constant cross-sectional area. As shown in Fig. 7.12, an additional waveguide can then be added to the existing shotgun tube circuit between the source and the tube to compensate for the small expansion.
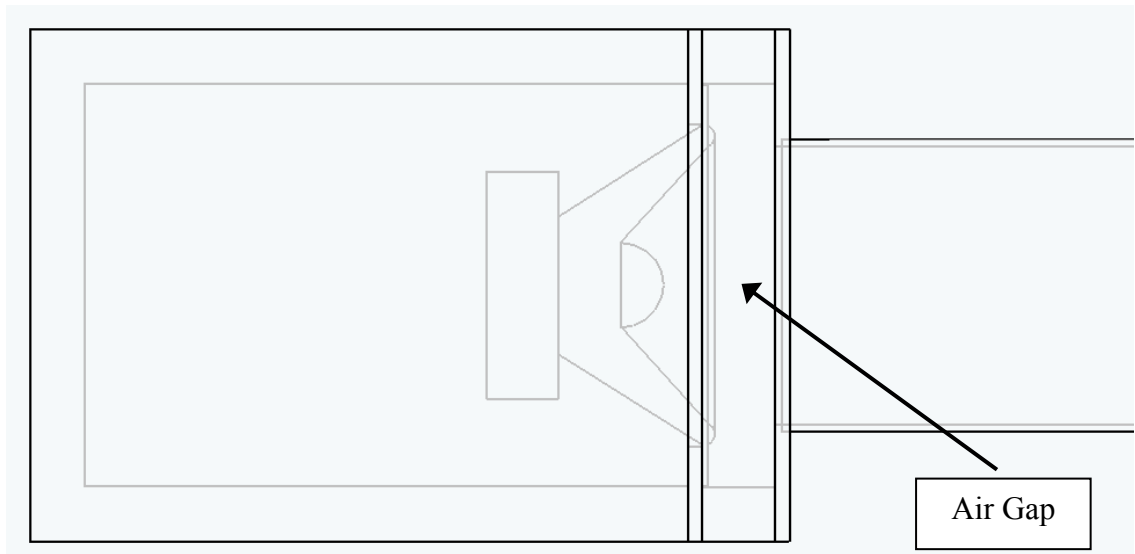
Figure 7.11. Diagram of the air gap between the loudspeaker and the tube.
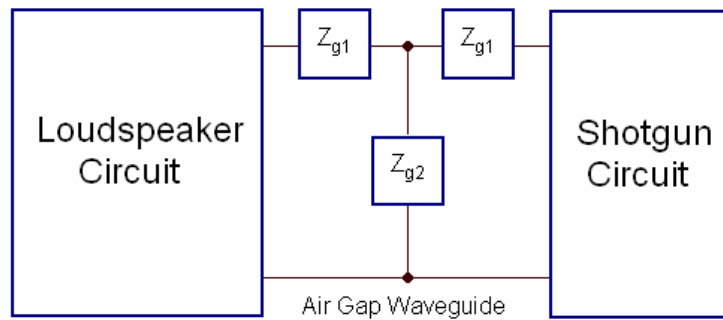
Figure 7.12. Simplified circuit to show placement of compensating air-gap waveguide.

As discussed in Chapter 4, the values of Z_{g1} and Z_{g2} are,

$$Z_{g1} = j\left(\frac{\rho_0 c}{S_g}\right)\tan\left(\frac{kL_g}{2}\right) \tag{7.17}$$

$$Z_{g2} = -j\left(\frac{\rho_0 c}{S_g}\right)\csc\left(kL_g\right) \tag{7.18}$$

where S_g is the cross-sectional area of the air gap and L_g is the width of the gap.

Again, no change in the polar response of the tube results from this modification. However, the on-axis frequency response should show a slight downward slope at the high-frequency end of the spectrum due to the first order low-pass filtering effects of the gap. This can be seen in Fig. 7.13 where a constant volume velocity source has been reintroduced into the model to isolate the effects of the air-gap only.
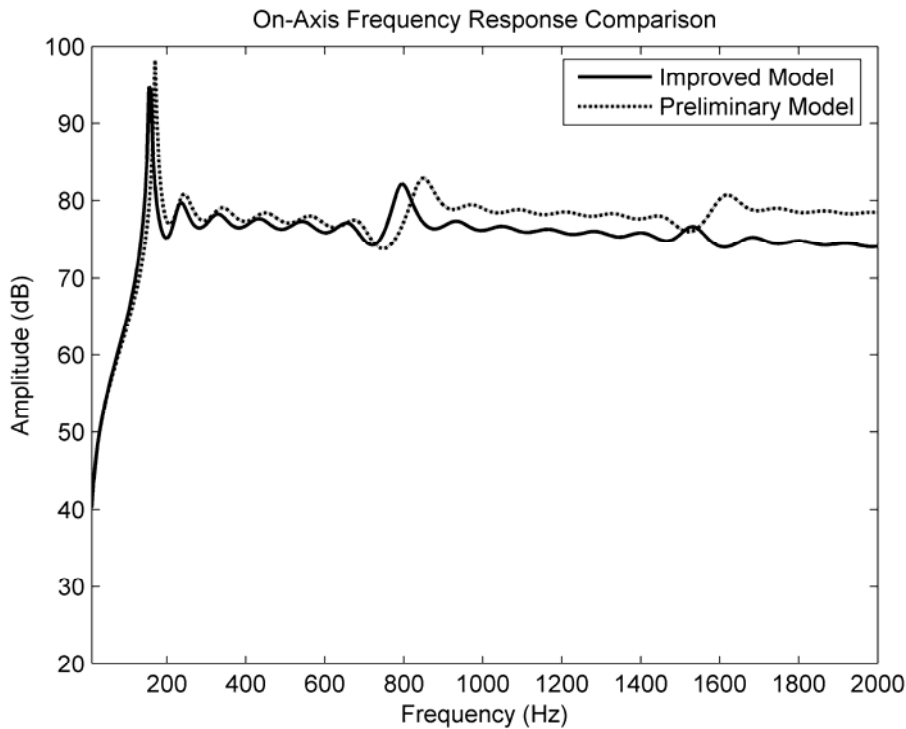
Figure 7.13. On-axis frequency response comparison to preliminary model.

114

7.4   Termination Impedance Values

The modification to the model that was expected to make the most noticeable change to the radiation patterns of the tube was the use of actual measured termination impedances for the anechoic and rigid terminations of the prototypes. The values were used in the model to calculate the new beamwidth curves. The absorption coefficient α and termination impedance Z_{AT} of a given termination are determined from the relationships [18],

$$\alpha = 1 - |R|^2 \tag{7.19}$$

and

$$Z_{AT} = \left(\frac{\rho_0 c}{S} \right) \left[\frac{1+R}{1-R} \right] \tag{7.20}$$

where R is the complex pressure-amplitude reflection coefficient evaluated at the termination.

Figure 7.14 shows the measured absorption coefficient for the anechoic termination used in the prototype measurements. Between 400 and 900 Hz the performance of the wedge begins to break down. Below 200 Hz, it is clearly not anechoic at all. Figure 7.15 shows the normalized real and imaginary parts of the acoustic impedance for the anechoic wedge. The real part behaves well for much of the bandwidth, where it has a value of approximately 1, and the imaginary part goes to 0. Given that these values are normalized, this means that the wedge presents an acoustic impedance of $\rho_0 c / S$ at most frequencies, which is the characteristic impedance for a plane wave. It therefore acts as a truly anechoic termination at these frequencies, so we would expect little change in the originally predicted beamwidth curve.
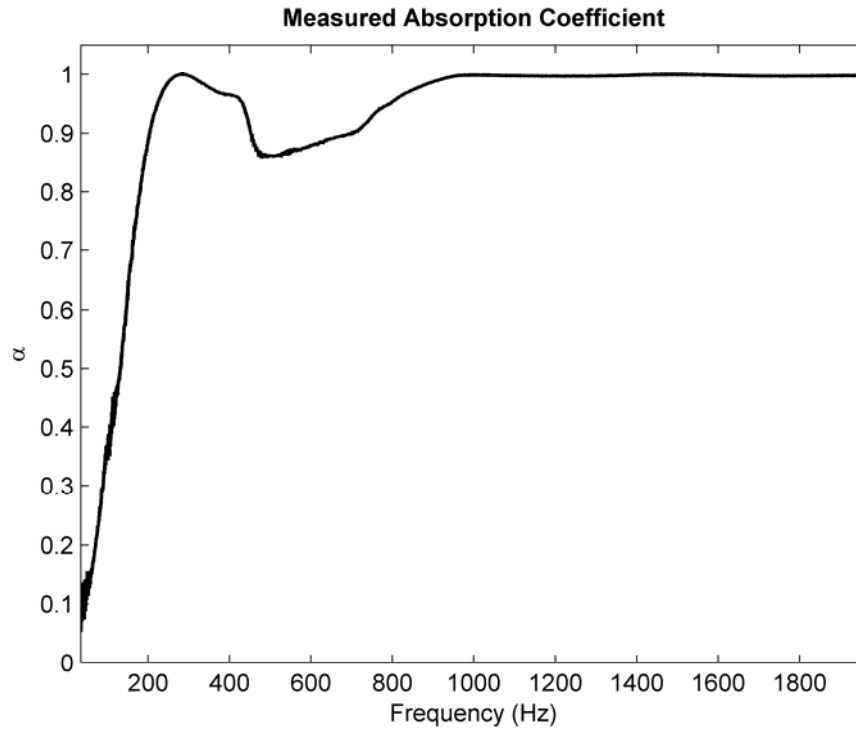
Figure 7.14. Absorption coefficient for the anechoic termination.
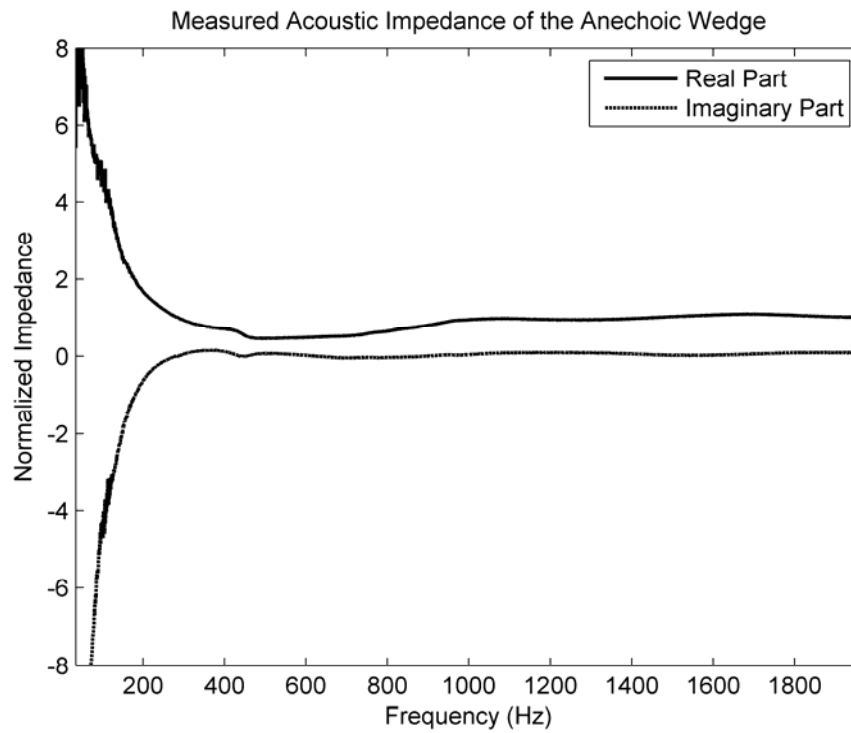
Figure 7.15. Normalized real and imaginary parts of Z_{AT} for the prototype anechoic termination.

116

Conversely, at low frequencies the imaginary part of the impedance is negative. This corresponds to an acoustic compliance and does not behave in the same manner as an anechoic wedge. Consequently, the original model may differ more significantly at these frequencies when compared to the new model.

Figure 7.16 is the beamwidth curve comparison between the models with and without the measured reflection coefficient built into the code. Again, all previously discussed improvements to the model were removed to isolate the effects of the termination impedances only. As expected, the curves show disagreement in the very low frequencies and in the 400 to 900 Hz regions where deviations from $\alpha \approx 1$ were seen in Fig. 7.14. The performance is actually improved at low frequencies, but larger undulations in the mid-band region begin to show up, indicating the nonanechoic nature of the termination.
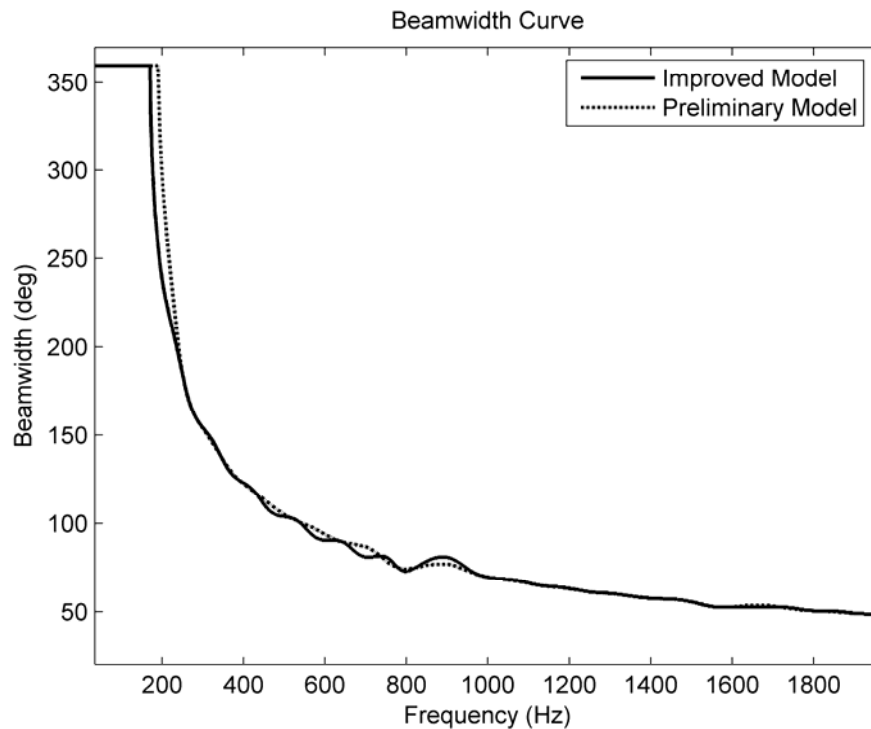
Figure 7.16. Beamwidth curve comparison to the preliminary model for the anechoic termination.

Figure 7.17 shows the change in the on-axis frequency response when using the measured value for the termination impedance. Notice that the only significant areas of change are where the wedge does not have anechoic properties (see Fig. 7.14).
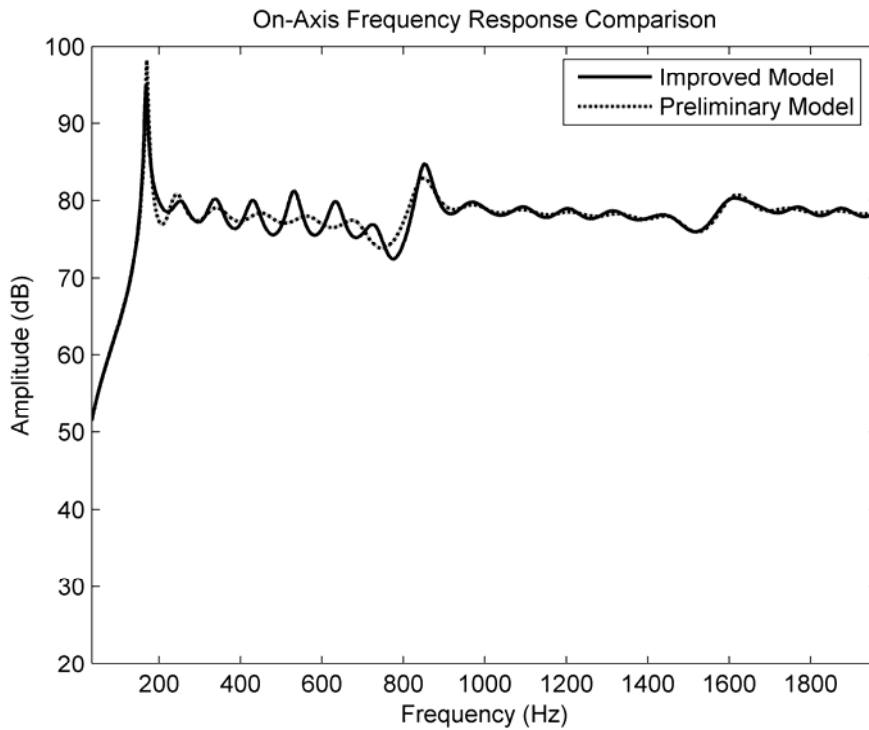
Figure 7.17. On-axis frequency response comparison to preliminary model with the anechoic termination.

The reflection coefficient was also measured for the rigid termination consisting of a plastic end cap. Using Eqs. (7.19) and (7.20), the absorption coefficient and the acoustic impedance were calculated, as well. Figure 7.18 shows the absorption coefficient for this condition, which is very small at all measurement frequencies.

Looking at the normalized real and imaginary parts of the acoustic impedance shown in Fig. 7.19, it is clear that the termination is acting as an acoustic compliance as a first-order approximation. This occurs at all frequencies, as shown by the negative value

of the imaginary part in the plot, as opposed to only the lowest frequencies as was the case for the anechoic wedge.

The beamwidth curves (Fig. 7.20) and the on-axis frequency response curves (Fig. 7.21) show almost no difference between the original and modified models for the rigidly terminated tube. Some of the resonance peaks are sharpened a bit when using the measured value of the reflection coefficient, but there is still overall agreement between the two results.
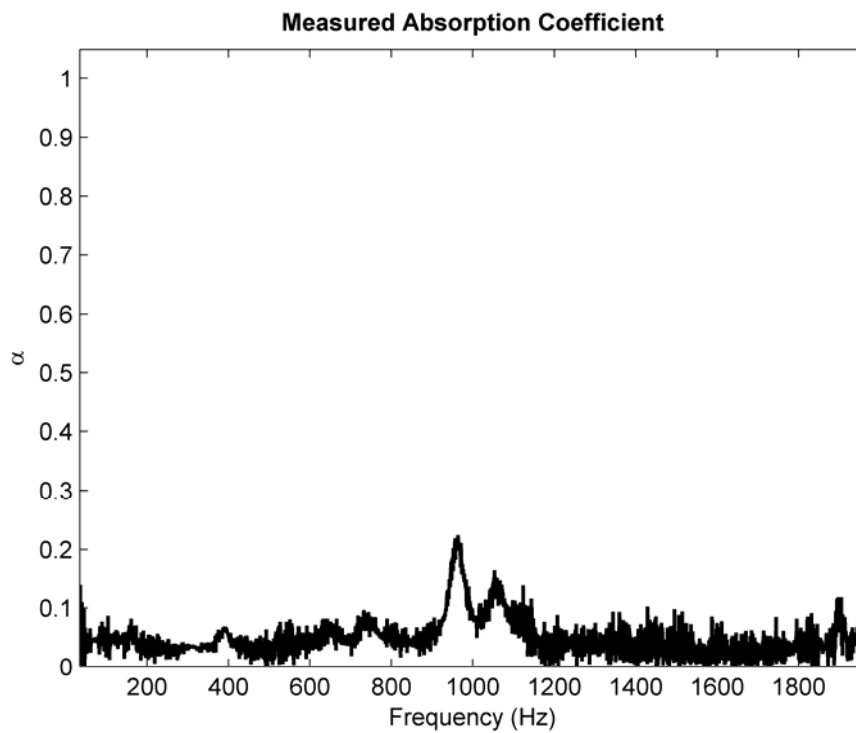
Figure 7.18. Absorption coefficient for the rigid termination.
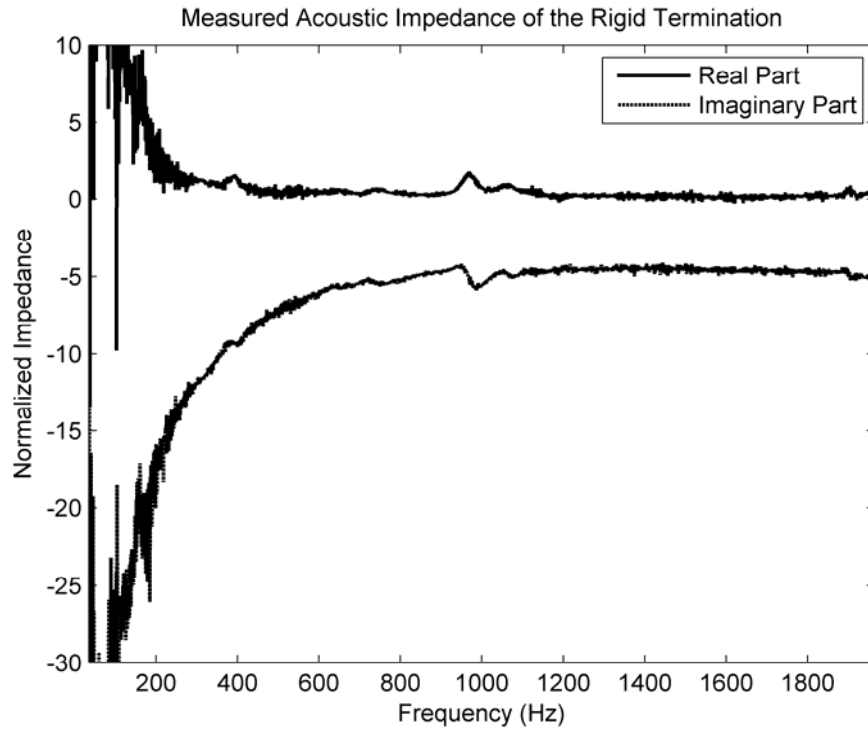
Figure 7.19. Normalized real and imaginary parts of Z_{AT} for the prototype rigid termination.
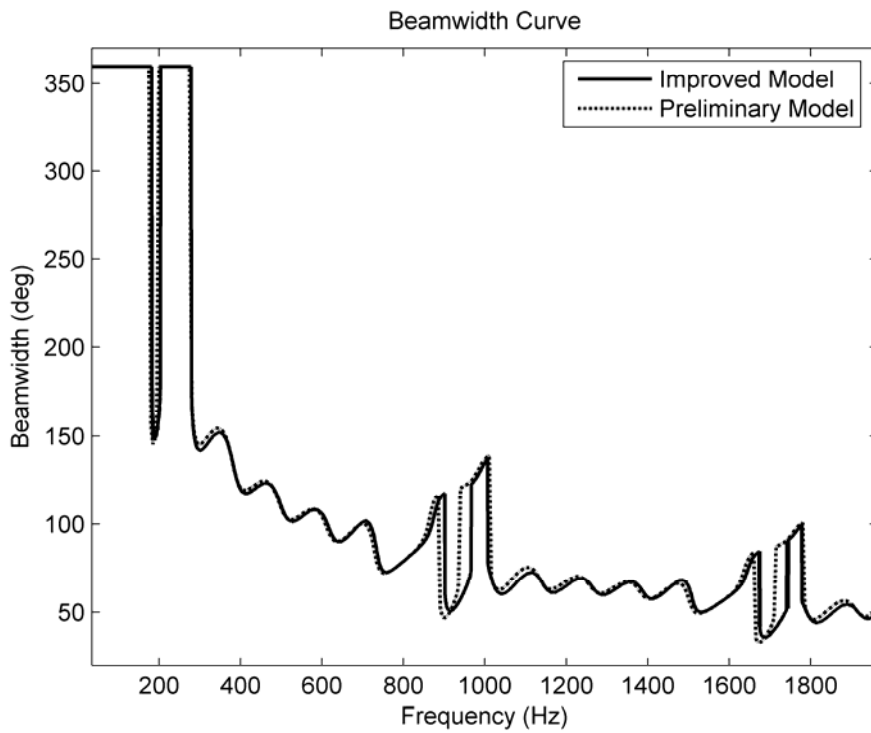
Figure 7.20. Beamwidth curve comparison to the preliminary model for the rigid termination.

120
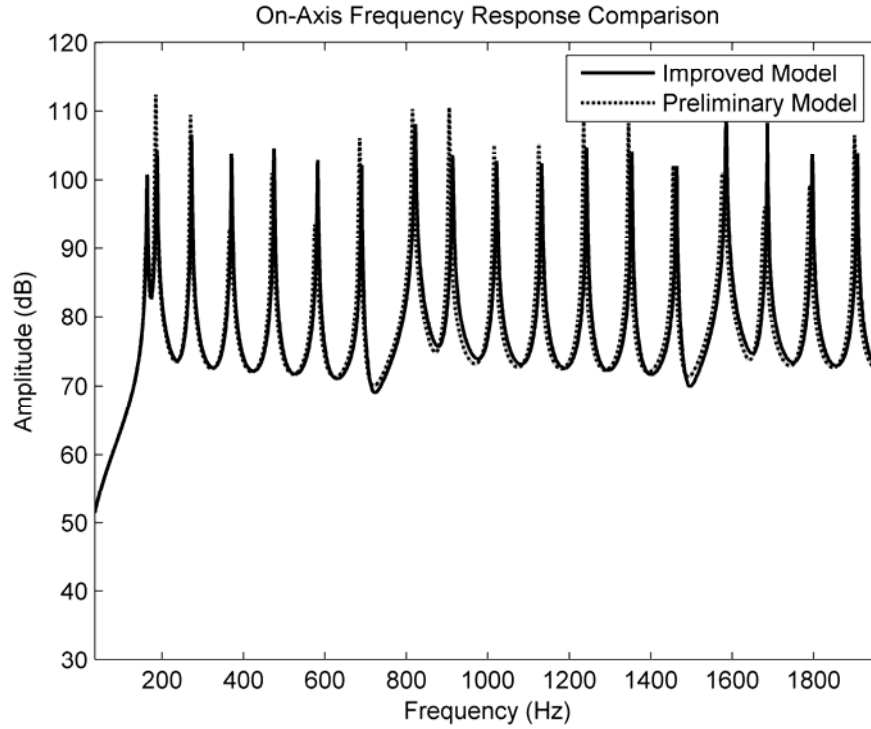
Figure 7.21. On-axis frequency response comparison to the preliminary model for the rigid termination.

7.5   Mutual Radiation Impedances

Yet another improvement to the analytical model was to account for mutual radiation impedances between holes. Originally, we assumed that the only interaction between holes was inside the tube because it was thought that the mutual radiation impedances would be quite small compared to internal and self radiation impedances.

Several references were found on mutual impedances of circular discs mounted in an infinite rigid baffle, but H.P. Neff's paper was the most straightforward [19]. Neff gives an expression for the real and imaginary parts of the mutual impedance as

$$Z_{12} = \pi\, a_1 a_2 \rho_0 c \left(R_{12} + j X_{12} \right), \tag{7.21}$$

where

$$R_{12} = 2J_1(ka_1)J_1(ka_2)\frac{\sin(kd)}{kd},$$ (7.22)

$$X_{12} = 2J_1(ka_1)J_1(ka_2)\frac{\cos(kd)}{kd},$$ (7.23)

and where a_1 and a_2 are the radii of the holes and d is the center-to-center spacing between them.

The standard simulation was run for the shotgun tube with six holes, 22 cm hole spacing, 1.27 cm hole radii, and a 5.08 cm tube radius, but in this case the Z_{12} term for each pair of holes was added to the expression for the hole radiation impedance given in Eq. (4.27) to account for hole coupling outside the tube.

Figure 7.22 plots the real and imaginary parts of the mutual radiation impedance for first hole (closest to the loudspeaker) due to the other five holes. As was expected, the amplitudes in this plot are approximately six orders of magnitude lower than the hole self radiation impedances, which leads us to expect no appreciable change in the beamwidth curve. The two curves were plotted and no apparent change could be seen. The on-axis frequency response was also unaffected.
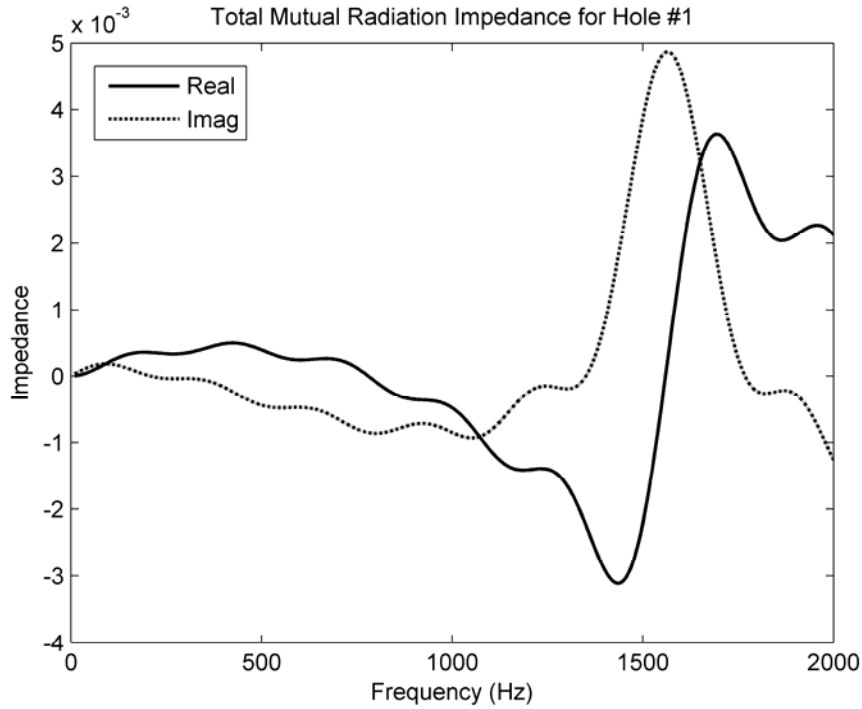
Figure 7.22. Real and imaginary parts of the total mutual radiation impedance for hole #1.

7.6   Improved Model vs. Measurement Comparison

Figures 7.23 and 7.24 show the beamwidth comparisons for the preliminary and the improved numerical model (which incorporates all refinements described in this chapter) of the long prototype with both the anechoic (Fig. 7.23) and rigid (Fig. 7.24) end conditions. The improved model curves in these plots incorporate all improvements to the numerical model discussed in this chapter.

Figures 7.25 and 7.26, on the other hand, plot the beamwidth curve of the improved numerical model against the measured data. When compared to the figures seen in Chapter 6, there is not a large change from one model to the other. The small changes are attributed primarily to the measured reflection coefficients of the terminations, as previously discussed.
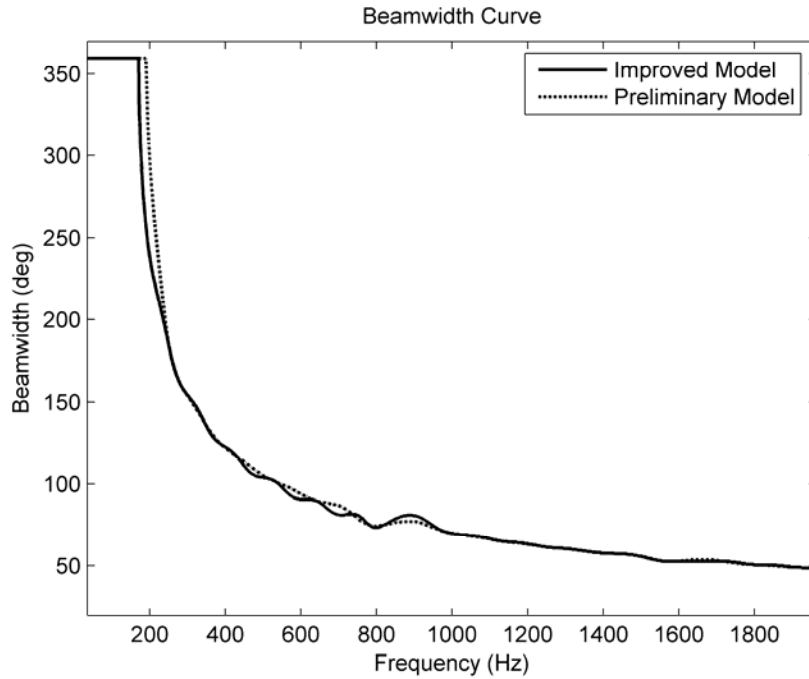
Figure 7.23. Beamwidth curve comparison for the improved and preliminary numerical model of the long prototype with the anechoic termination. The improved model incorporates all model refinements discussed in this chapter.
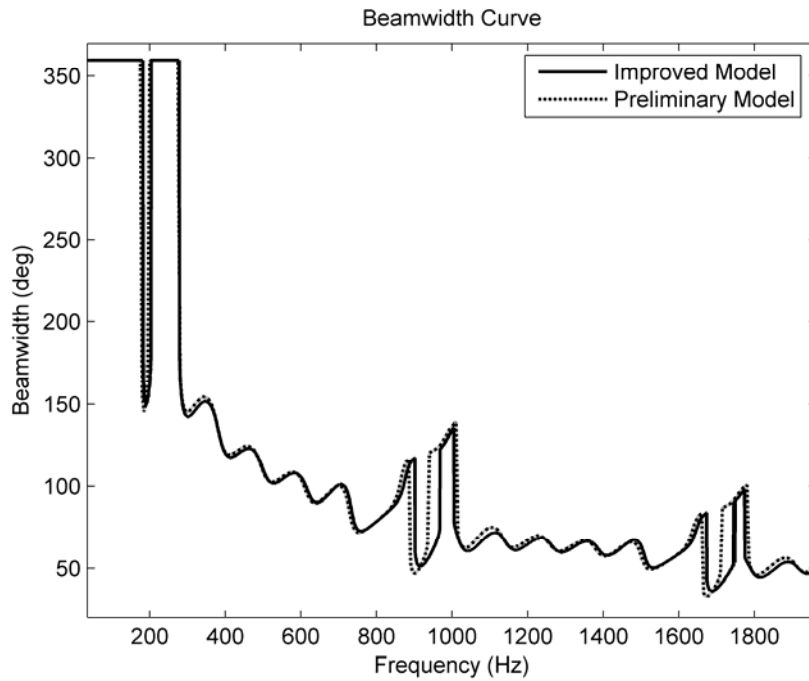
Figure 7.24. Beamwidth curve comparison for the improved and preliminary numerical model of the long prototype with the rigid termination. The improved model incorporates all model refinements discussed in this chapter.
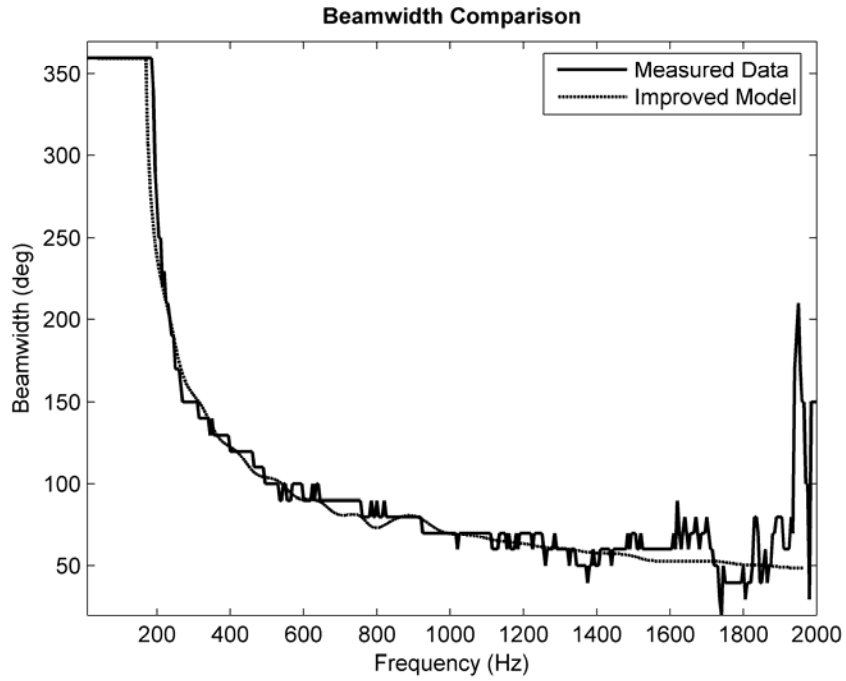
Figure 7.25. Beamwidth curve comparison for the long prototype with an anechoic termination. The solid trace is the measured data and the dashed trace is the predicted data from the improved numerical model.
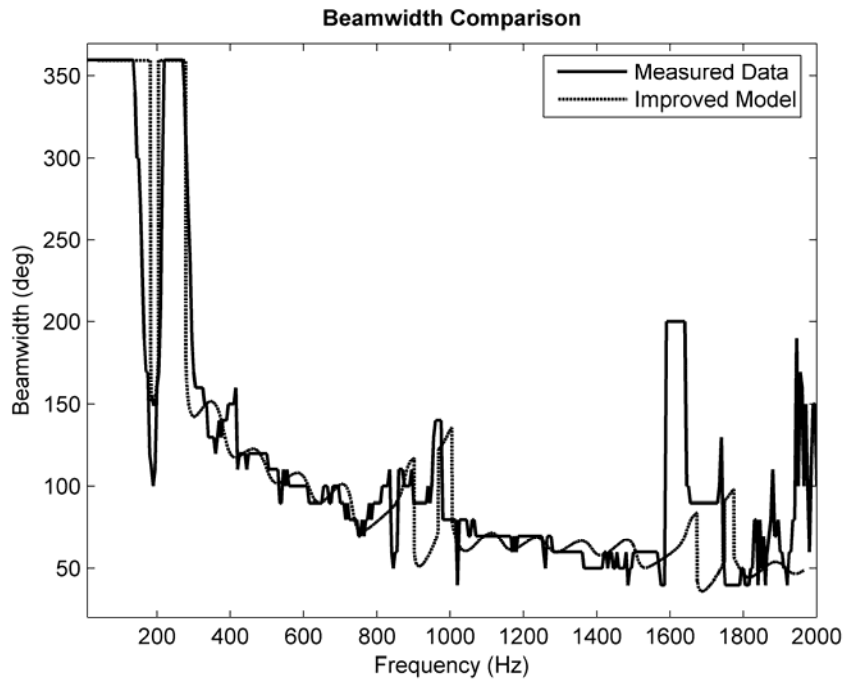
Figure 7.26. Beamwidth curve comparison for the long prototype with a rigid termination. The solid trace is the measured data and the dashed trace is the predicted data from the improved numerical model.

There are several other important changes that come out of the new model. First, the amplitude of the polar patterns is now a calculated value from the input voltage applied to the loudspeaker terminals. Both the measured data and the modeled data in the following figures have an input voltage of 5 volts. Figures 7.29 through 7.31 are polar patterns for the long prototype with an anechoic termination and Figs. 7.32 through 7.34 are for the same prototype with a rigid termination. These plots are for the same frequencies presented in Chapter 6. As expected from the beamwidth curves shown previously, there is not a large change in the shape of the polar patterns for either of the conditions.

(a)   (b)
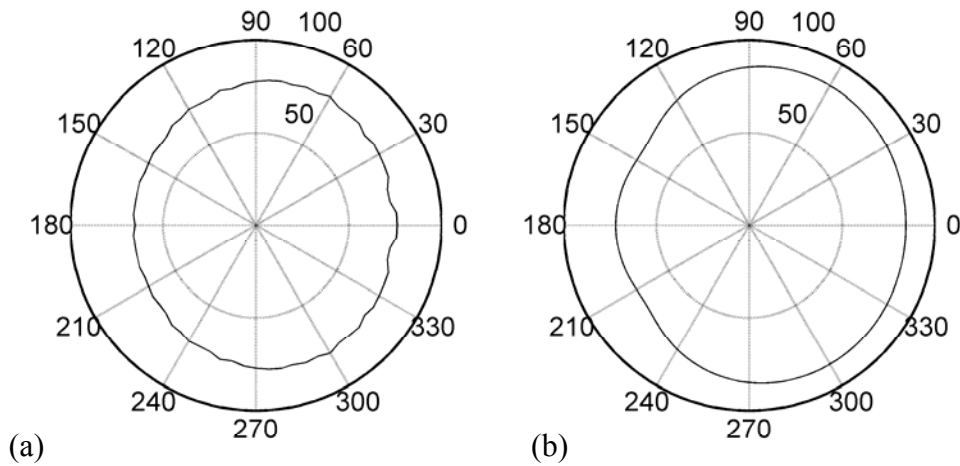
Figure 7.27. Polar pattern comparison for the long tube with an anechoic termination at 200 Hz. (a) Measured data. (b) Modeled data.

126
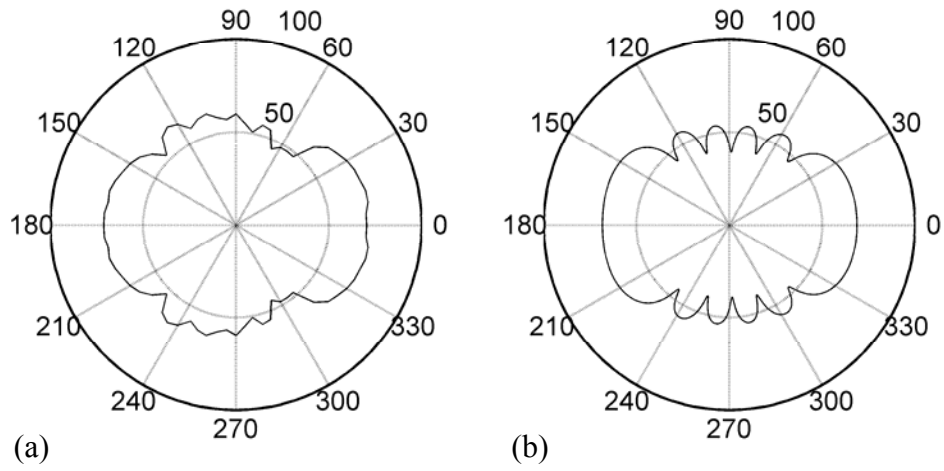
Figure 7.28. Polar pattern comparison for the long tube with an anechoic termination at 800 Hz. (a) Measured data. (b) Modeled data.
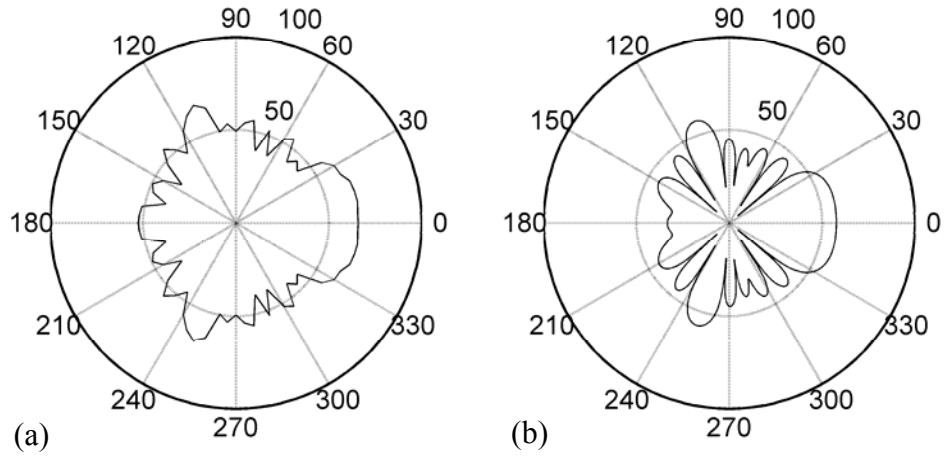
Figure 7.29. Polar pattern comparison for the long tube with an anechoic termination at 1200 Hz. (a) Measured data. (b) Modeled data.
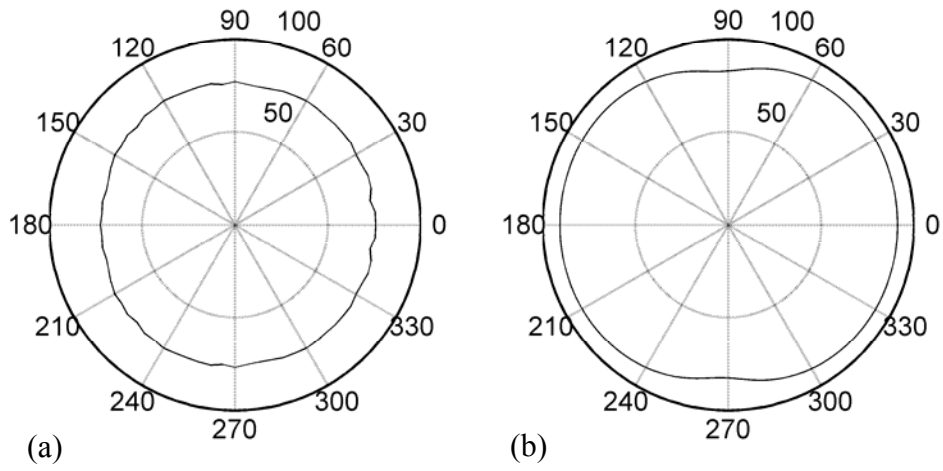
Figure 7.30. Polar pattern comparison for the long tube with a rigid termination at 200 Hz. (a) Measured data. (b) Modeled data.
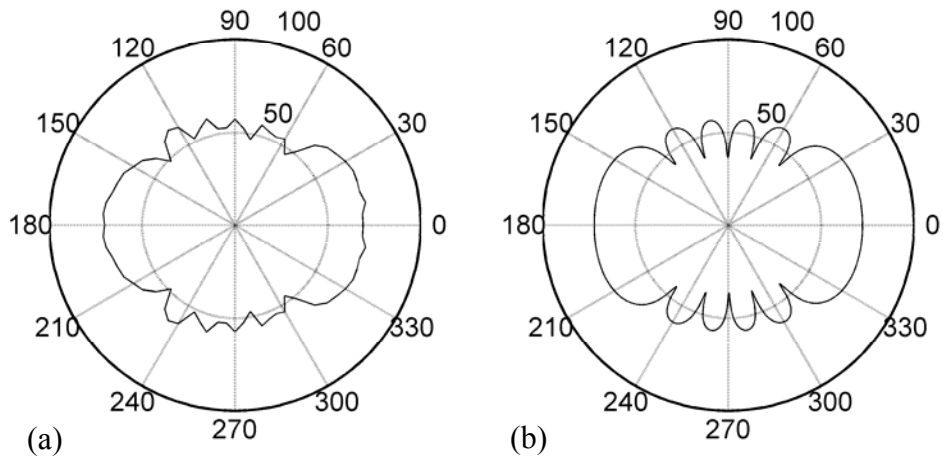
Figure 7.31. Polar pattern comparison for the long tube with a rigid termination at 800 Hz. (a) Measured data. (b) Modeled data.
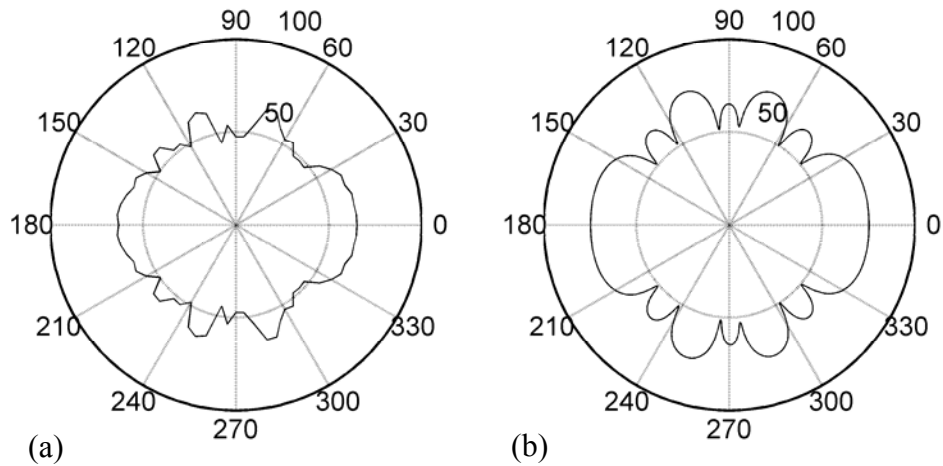
Figure 7.32. Polar pattern comparison for the long tube with a rigid termination at 1200 Hz. (a) Measured data. (b) Modeled data.

The most significant improvements we get from the new models are much more accurate frequency response predictions. Figures 7.35 and 7.36 show on-axis frequency response comparisons for the anechoic termination (Fig. 7.35) and the rigid termination (Fig. 7.36). The amplitudes are much closer than the older models suggest and the shapes of the curves lines up much better with the measured data. Once the frequency reaches the point where the half-wavelength is equal to the spacing between holes (approximately 800 Hz in this case) there is a discrepancy between the modeled and measured results that requires further investigation. It cannot be ignored, however, since it shows up in all frequency response plots.
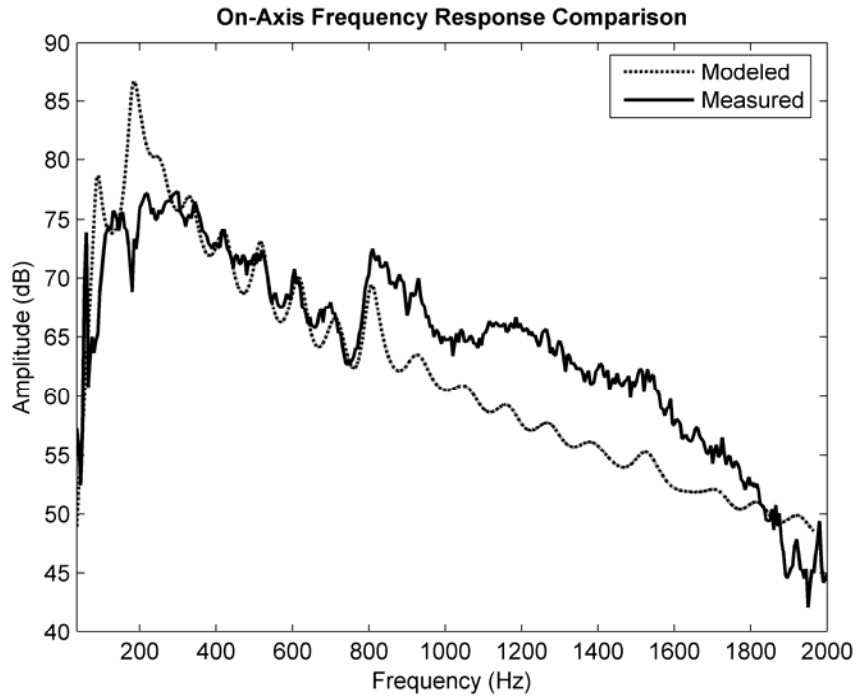
Figure 7.33. Measured on-axis frequency response comparison for the measured data (dashed trace) and the improved model data (solid trace) both with an anechoic termination.
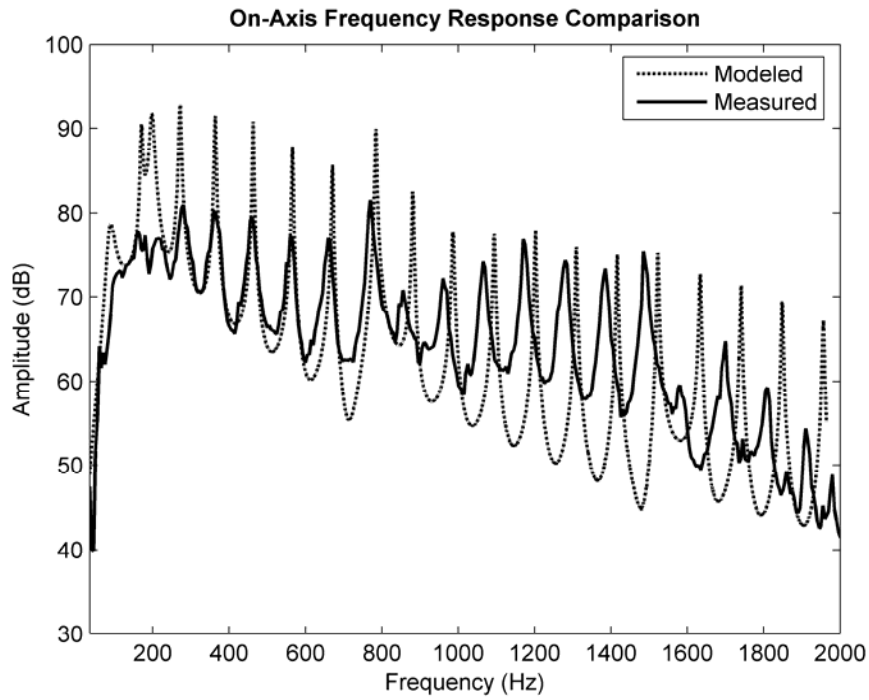
Figure 7.34. Measured on-axis frequency response comparison for the measured data (dashed trace) and the improved model data (solid trace) both with a rigid termination.

130

Finally, the electric input impedance of the system is another value that can be extracted from the new model that was not available in the older model. The electric impedance of the driver mounted in the sealed box radiating into free-space and into the shotgun tube was measured using the MLSSA system. Figure 7.37 shows the *measured* impedance of the two setups and Fig. 7.38 shows the *modeled* impedance of the two configurations. It is clear that there is good agreement between the two cases. The main discrepancy is the height of the peaks resulting from the additional loading the shotgun tube places on the driver. The measured peaks are smaller in amplitude, which may indicate that our model of the losses in the tube and the loudspeaker enclosure are not adequate.
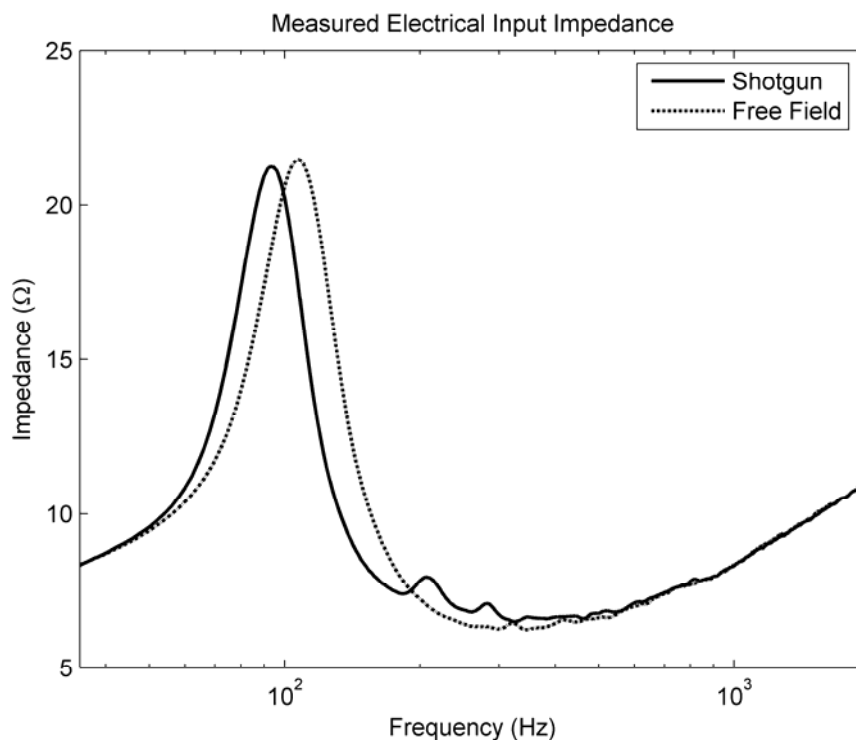
Figure 7.35. Measured input impedance comparison for the loudspeaker radiating into free-field (dashed trace) or into the shotgun tube (solid trace).

131
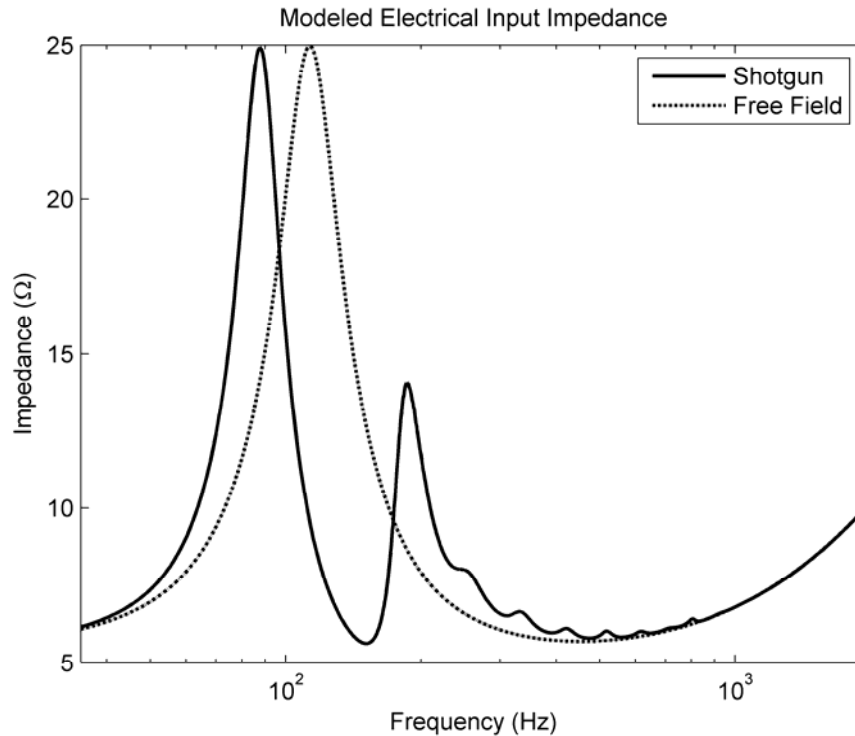
Figure 7.36. Modeled input impedance comparison for the loudspeaker radiating into free-field (dashed trace) or into the shotgun tube (solid trace).

7.7 Improved Model Summation

This chapter has detailed improvements made to the numerical model to enhance the agreement between the predicted and measured data. It is clear that including the losses in the tube, a loudspeaker source model, an air-gap model, and the mutual radiation impedance terms do not have a substantial effect on the predictive capabilities of the analytical model, when looking only at the beamwidth curve. Including measured termination impedances and inserting them into the model, however, does have a noticeable impact that improves the agreement between the predicted and measured results.

However, when considering the on-axis frequency response the loudspeaker driver and air-gap models were quite important. Inserting the loudspeaker representation into the numerical model allowed us to predict the electric input impedance, the on-axis frequency response, and the polar pattern amplitudes for comparison with the measured data. The air-gap model gave us the slope we desired due to the filtering of the expansion cavity near the loudspeaker diaphragm.

CHAPTER 8

FURTHER INVESTIGATIONS

Once the numerical model was proven to be reasonably accurate, there were a few remaining variations of the shotgun tube that were still of interest. Some of the variations, however, involved prototypes that could not presently be fabricated but numerical models were found to offer valuable information. The agreement seen between measured and modeled results in the previous chapters provided a confidence level in the numerical predictions given in this chapter.

8.1 Hole Radius Variations

One variation of the shotgun tube involved varying the hole radius along the tube axis. A benchmark hole radius was chosen to be 1.27 cm (the radius used in the long prototype) and the following variations will be compared to the response found with this hole radius.

Figure 8.1 shows a beamwidth comparison for three types of hole variations. The solid trace is for a hole radius of 1.27 cm for all six holes. The dashed trace is for a tube with a mean hole radius of 1.27 cm, but the hole radii ascend in value along the tube axis from nearest the loudspeaker 0.52 cm to 2.02 cm nearest the termination. The dotted trace has the same mean and range of radii values, but the radii *descend* from 2.02 cm to 0.52 cm. In this comparison, there is a well-defined offset from the original configuration in the positive direction in both cases which is undesirable.
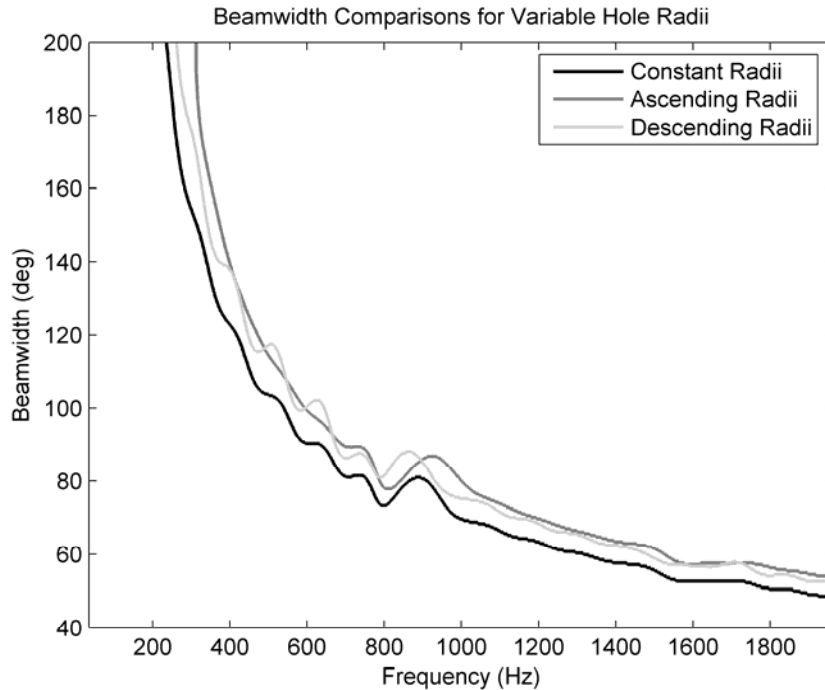
Figure 8.1. Beamwidth comparisons for variable hole radii. The solid trace is for a constant hole radius of 1.27 cm. Both ascending (dashed trace) and descending (dotted trace) radii are also shown with radii ranging from 0.52 to 2.02 cm, with a mean value of 1.27 cm. The beamwidth range has been zoomed in to better show the difference between simulations.

In order to inspect more closely what is happening to the polar pattern, Figs. 8.2, 8.3, and 8.4 were also generated. These plots show the polar angle on the x-axis ($\theta = 0°$ is on-axis) versus frequency on the y-axis. The color corresponds to the pressure amplitude computed at a given angle and frequency. Figure 8.2 is our benchmark of a constant hole radius. The front lobe width can be estimated by doubling the width of the high amplitude sound that starts at 0° and stops at the first dip. In this case it is very well defined and follows a very distinct curve.

Figures 8.3 and 8.4, however, are much less defined. The deep nulls that occur with a constant radius seem to smear across the polar angle which then widens the lobes. This is perhaps more clear in Fig. 8.5, where the polar patterns of all three configurations are plotted side-by-side for 600 Hz, where the smearing effect is quite obvious.

135
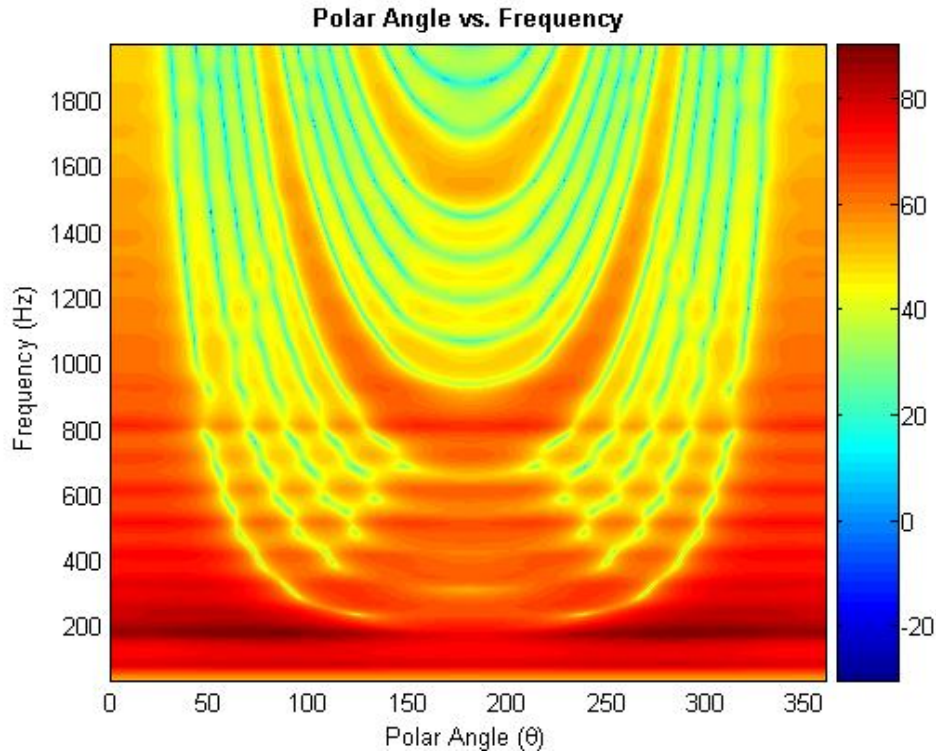
Figure 8.2. Polar angle vs frequency plot for the constant hole radii configuration. Hole radius is 1.27 cm.
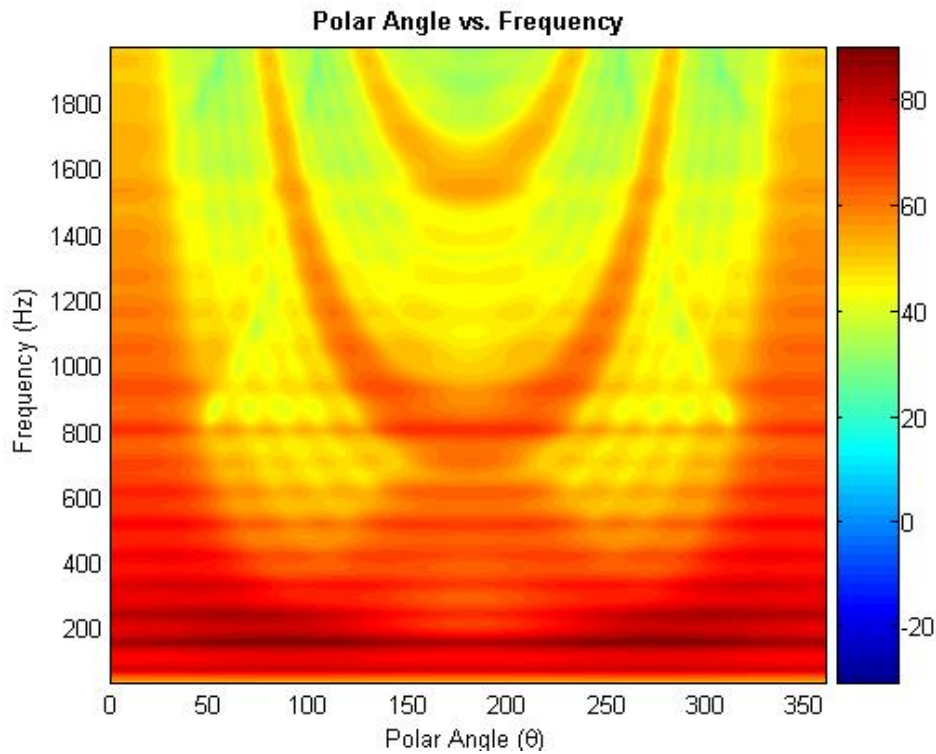
Figure 8.3. Polar angle vs frequency plot for the ascending hole radii configuration. Mean radius is 1.27 cm, minimum radius is 0.52 cm, and maximum radius is 2.02 cm.

136
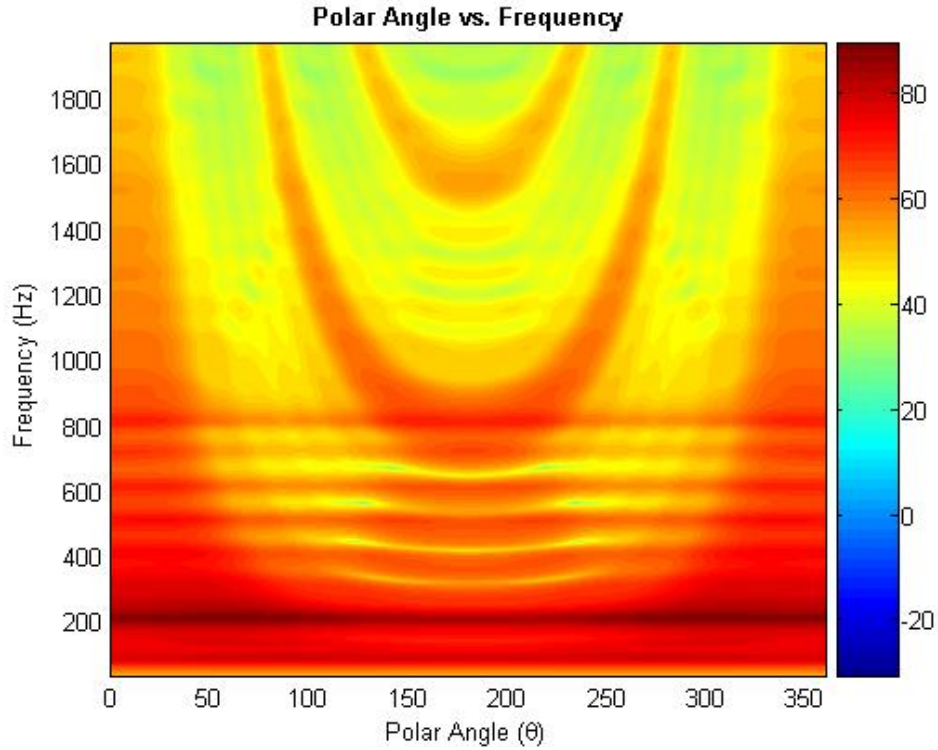
Figure 8.4. Polar angle vs frequency plot for the descending hole radii configuration. Mean radius is 1.27 cm, minimum radius is 0.52 cm, and maximum radius is 2.02 cm.

(a) (b) (c)
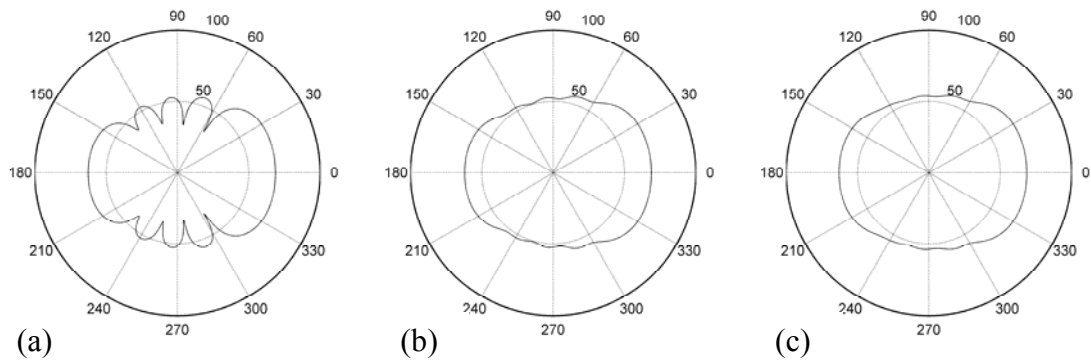
Figure 8.5. Polar plot comparison at 600 Hz. (a) Constant hole radius. (b) Ascending hole radius. (c) Descending hole radius.

Figure 8.6 shows the on-axis frequency responses for same three configurations of the shotgun tube. In this case, all three exhibit the same general trends in behavior and therefore little useful information can be gleaned from the figure.
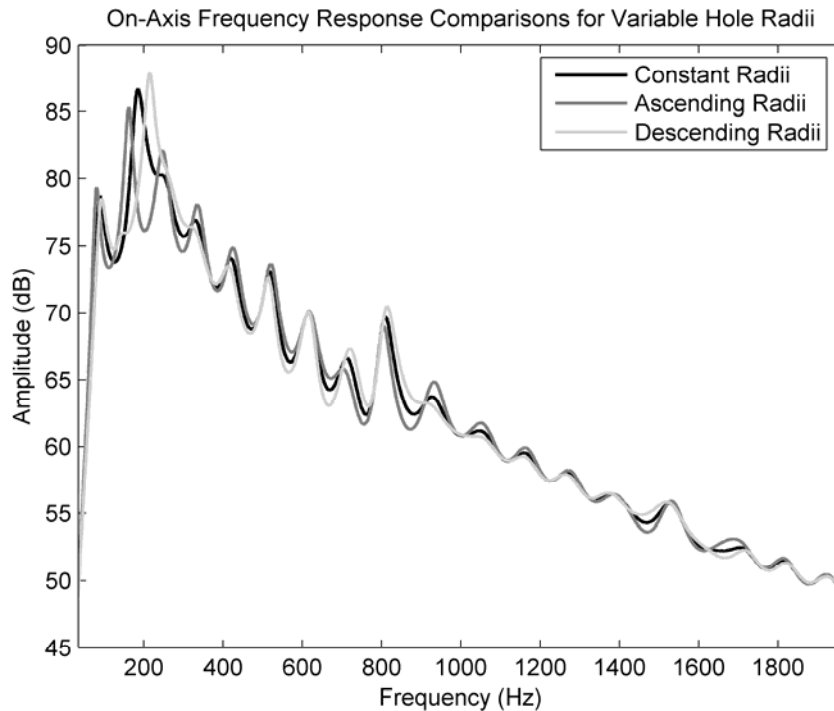
Figure 8.6. On-axis frequency response comparison for variable hole radii. The solid trace is for a constant hole radius of 1.27 cm. Both ascending (dashed trace) and descending (dotted trace) radii are centered around 1.27 cm radius with a range of 0.52 to 2.02 cm.

8.2   Hole Impedance Variations

Varying the hole impedance by way of resistive materials or small passive diaphragms was another variation on the shotgun tube that proved interesting. When the resistances of the holes are varied along the tube, a resistance profile is created. Similarly, when small diaphragms are placed over each hole and the diaphragm mass is

varied along the tube (which shifts the resonance frequencies of the diaphragms), a mass profile is created. Both of these configurations are explored below.

8.2.1 Resistance Profiles

A set of simulations was first run to investigate the effect that adding resistance profiles has on the beamwidth and frequency response. The first run was our benchmark set of data where no resistance was added to any holes. This is shown as the solid trace in Fig. 8.7. The remaining two traces in the figure are for ascending resistance (dashed trace) and descending resistance (dotted trace) profiles. The ascending and descending simulations had a resistance range from 0 to 10^5 *kg/s*, with a mean of $5*10^4$ *kg/s*. This figure shows that incorporating an ascending resistance profile worsens the beamwidth curve at all frequencies. Conversely, applying a descending resistance profile actually improves the performance by a sizeable amount.

Figure 8.8 shows the polar plots of all three configurations at 600 Hz. The left plot (no resistance) and the center plot (ascending resistance profile) are quite similar in where the nulls occur, but adding the ascending profile seems to fill in the nulls as we saw in the variable hole radii simulations in the previous section. This smearing of the polar pattern effectively widens the lobes and therefore decreases directional performance.
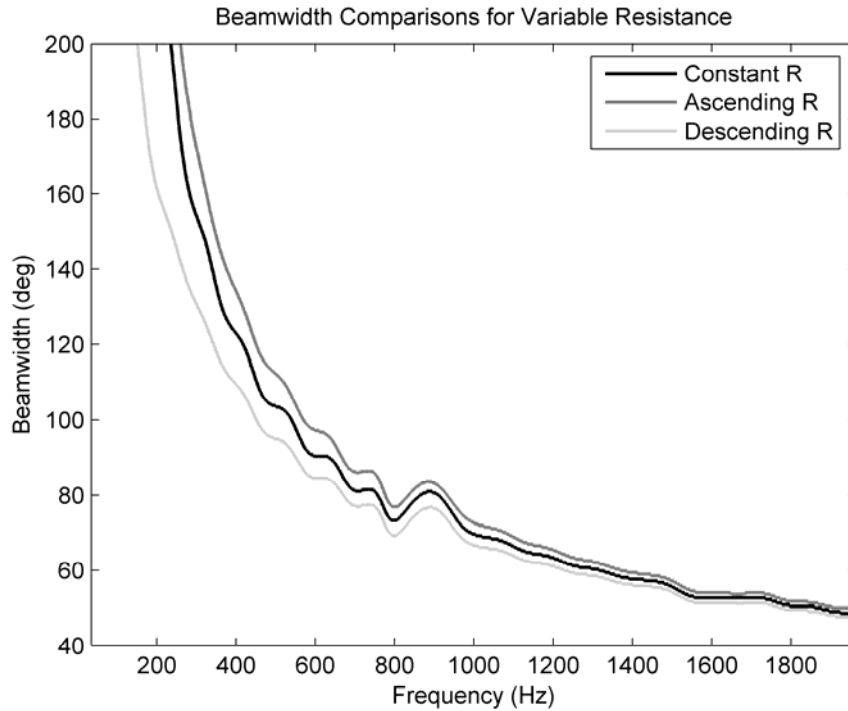
Figure 8.7. Beamwidth comparison for hole resistance profiles. The solid trace is for no added resistance. Both ascending (dashed trace) and descending (dotted trace) resistance profiles have a range from 0 to 10^5 kg/s. The beamwidth range has been zoomed in to better show the difference between simulations.

The right plot in Fig. 8.8, however, not only shares the deep nulls that zero resistance shows, but the nulls are also shifted a small amount toward the on-axis position (0˚). When the tube is terminated by an anechoic wedge, as it is in these simulations, there is a general decrease in hole volume velocity for holes farther from the source. The decrease is due to propagation losses and internal reflections at impedance discontinuities. The descending resistance profile reduces the output from the holes closest to the source by a larger amount, thus creating closer volume velocity matching for the outputs of all holes. The resulting increase in interference efficiency then improves the far field beamwidth results.

140
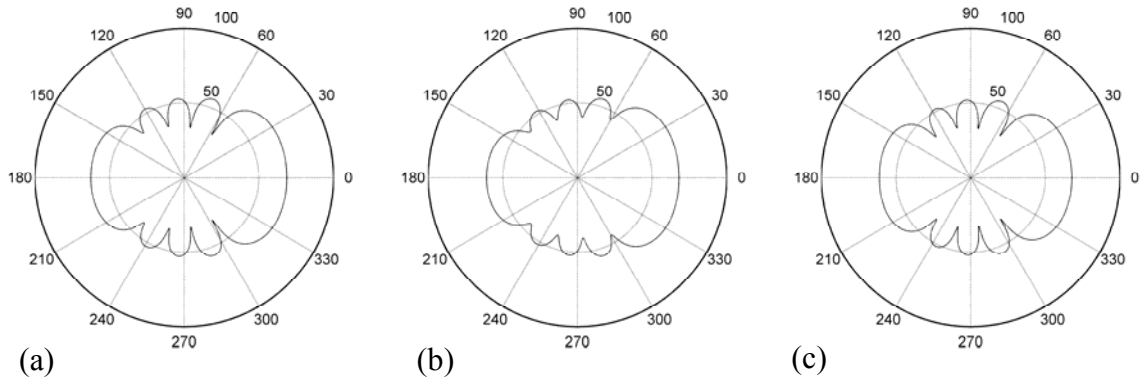
Figure 8.8. Polar plot comparison at 600 Hz. (a) No added resistance. (b) Ascending resistance profile. (c) Descending resistance profile.

Figure 8.9 shows the on-axis frequency response for all three simulations. In this case a noticeable difference in the low-frequency response is shown. As resistance is added to the holes, the output is reduced by a substantial amount and the response somewhat smoothed. Although the smoothing effect may be desirable, the reduced output may be detrimental in commercial applications where power amplification can be expensive.
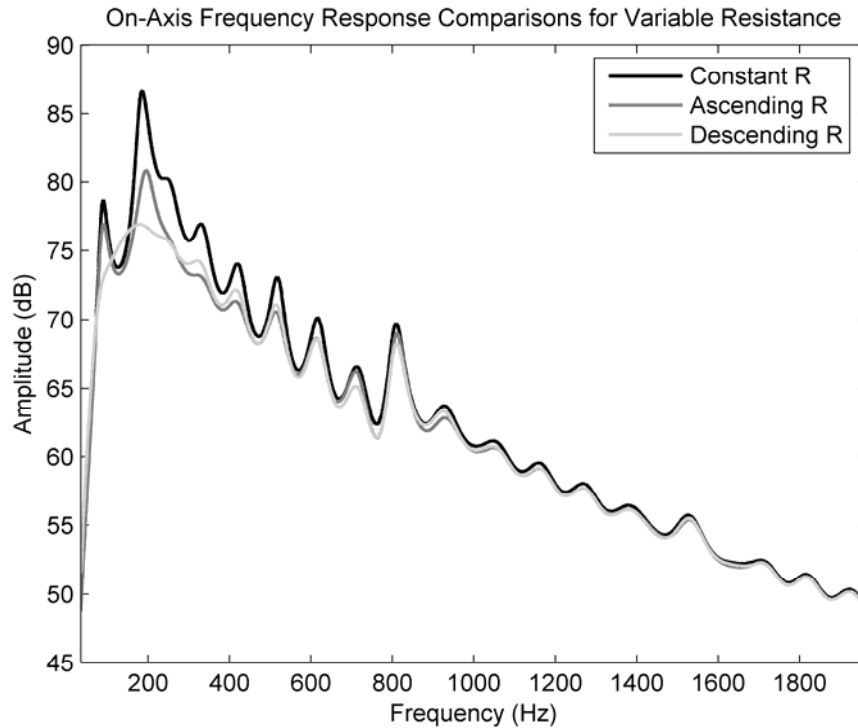
Figure 8.9. On-axis frequency response comparison for resistance profiles. The solid trace is no added resistance. Both ascending (dashed trace) and descending (dotted trace) resistance profiles have a range from 0 to 10^5 kg/s.

8.2.2 Mass Profiles

Another configuration of interest was the mass profile, which is a bit more complicated than simply increasing the acoustic resistance of an orifice. A mass profile is created by inserting a small diaphragm in each hole. This can be modeled using the same circuit used to model a drone cone termination in combination with the shotgun equivalent circuit. This combined circuit is shown in Fig. 8.10. This is basically a mass-spring system with internal damping. The values used in this simulation are given in Table 8.1. The variable mass of the system is what is of primary interest here.

142
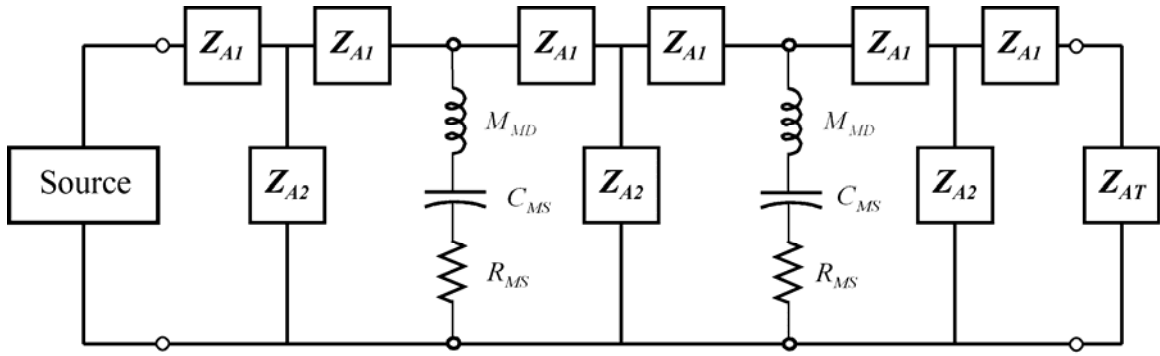
Figure 8.10. Equivalent circuit for a shotgun tube with diaphragms over the holes.

Parameter	Value	Units
R_{MS}	0.106	kg/s
C_{MS}	1893	μm/N
M_{MD}	variable	kg
S_d	6	cm^2

Table 8.1. Parameters used to model the diaphragms placed in tube holes to create the mass profiles.

As the mass varies, the resonance frequency of the system varies inversely. Figure 8.11 shows the reflection coefficient calculated at each hole looking into the diaphragm (given by Eq. (7.20)) when the mass is varied from 0.5 to 2 grams. All other parameters describing the system are given in Table 8.1. In this figure, it is clear that there is a well-defined resonance for each diaphragm where the reflection coefficient is at a minimum. For a mass of 2 grams, the resonance frequency is approximately 70 Hz. It slowly moves up as the mass is decreased, reaching a value of about 130 Hz for a mass of 0.5 grams. This variable resonance of the system caused by the addition or subtraction of mass is the focus of this simulation. Figure 8.12 shows the beamwidth curves for three different configurations: no diaphragms in the holes, an ascending mass profile, and a descending mass profile.
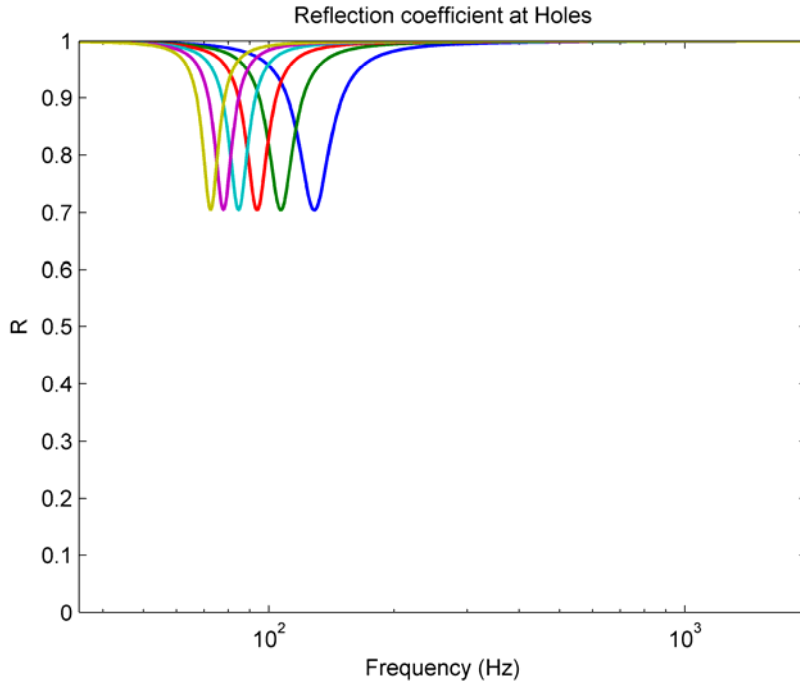
Figure 8.11. Reflection coefficient calculated at each hole using a mass profile. The mass of each diaphragm was varied from 0.5 to 2 grams.
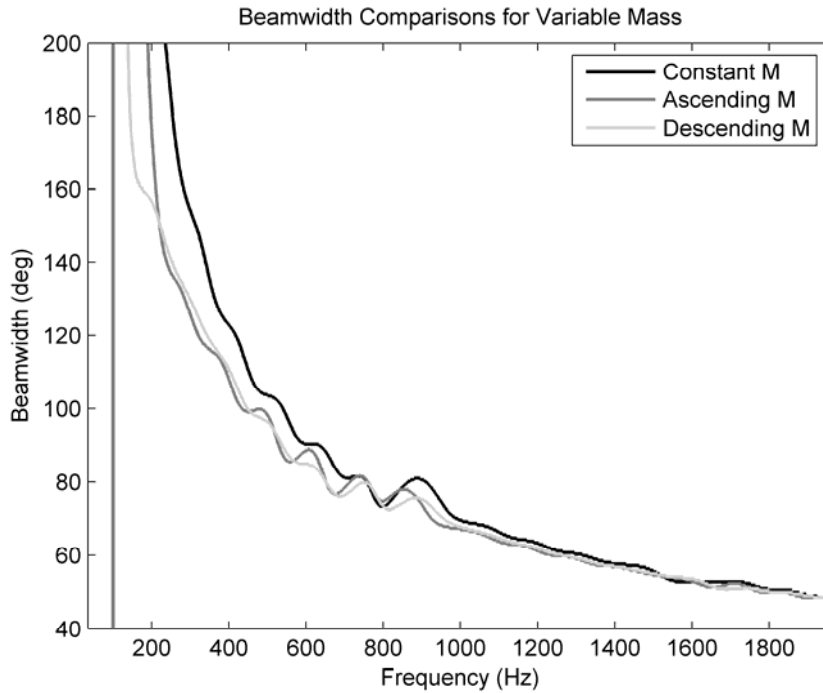
Figure 8.12. Beamwidth comparison for mass profiles. The solid trace is for 0 mass. Both ascending (dashed trace) and descending (dotted trace) mass profiles have a range of 0.5 to 2 grams. The beamwidth range has been zoomed in to better show the difference between simulations.

The first impression from Fig. 8.12 is that adding a mass profile into the holes only improves performance. Both ascending and descending configurations result in a narrower beamwidth and the descending profile does much better than either of the other two simulations below 200 Hz.

The polar patterns at 600 Hz are shown in Fig. 8.13 for comparison. As seen in the resistance profiles, an ascending mass profile smears the energy over the polar angle and fills in the nulls in the left plot, where no diaphragms are mounted in the holes. Although this smearing occurs, the main lobe is still substantially narrowed, which results in the improved beamwidth curve. The plot shown on the right of Fig. 8.13 shows many improvements. The width of the front lobe is narrowed even more than that seen in the ascending profile. Another improvement that has not been seen in any simulations thus far is the narrowing of the side and rear lobes, as well.

While this seems to show that using a mass profile improves the overall performance of the shotgun tube, a closer look at the amplitudes of the center and right plots in this figure raises a concern. The main lobe may be narrower, but the amplitude is drastically reduced from the benchmark simulation on the left.

Seeing this drastic reduction in amplitude led to the plots shown in Fig. 8.14. This figure shows the on-axis frequency responses found for each of the three simulations. It is obvious that both the ascending and descending profiles lead to a staggering decrease of approximately 35 dB across the entire frequency range. In the discussion of the resistance profiles, it was stated that a reduction of even 10 dB is detrimental to commercial applications, where input power can be expensive. The reductions seen here would then be quite unacceptable.
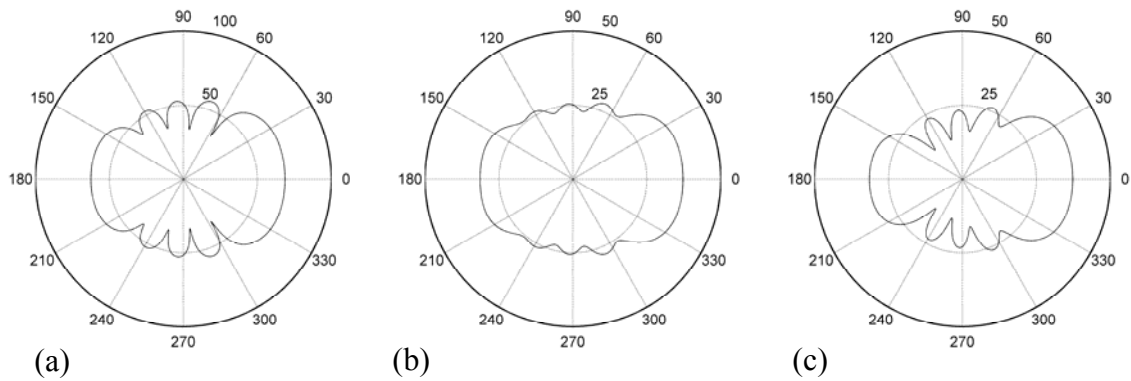
Figure 8.13. Polar plot comparison at 600 Hz. (a) 0 mass. (b) Ascending mass profile. (c) Descending mass profile.
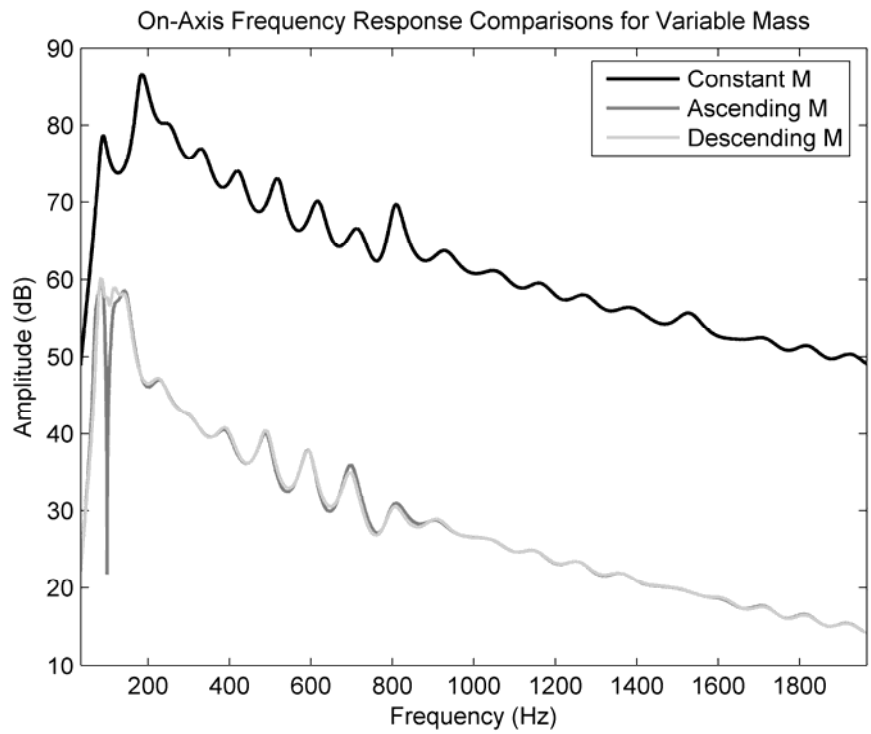
Figure 8.14. On-axis frequency response comparison for mass profiles. The solid trace is for 0 mass. Both ascending (dashed trace) and descending (dotted trace) mass profiles have a range of 0.5 to 2 grams.

146

8.3   Sensitivity Investigations

Although many of the previously discussed configurations improved the performance seen on the beamwidth curves, it was shown that the amplitude of the on-axis frequency response suffered. This led to the definition of a relative sensitivity variable, G, defined as

$$G = 20\log\left(\frac{|\hat{p}_s|}{|\hat{p}_{ff}|}\right) \tag{8.1}$$

where $|\hat{p}_s|$ is the on-axis pressure amplitude magnitude of a given shotgun tube configuration and $|\hat{p}_{ff}|$ is the far field on-axis pressure amplitude magnitude of the same driver mounted in a sealed sphere [20] (containing the same volume of air as the prototype source enclosure) and radiating into free space. The latter is based on the same voltage input as used in the shotgun loudspeaker. The value was calculated for three frequencies spread throughout the frequency range, for seven different configurations. The input voltage was set to one volt and the on-axis pressure value at one meter was calculated from the far-field pressure found by interpolating the value found at ten meters. This was done so that the original value calculated at ten meters was in the geometric and acoustic far field of the shotgun tube. The results are shown in Table 8.2.

The first row shows the results for the standard shotgun tube that has been our benchmark for comparison throughout this chapter. The remaining six configurations are the variations on the shotgun tube discussed in the previous sections. It is clear from this table that a mass profile reduces the sensitivity drastically and is therefore not recommended. At low frequencies, using a variable hole radius or applying a resistance profile along the tube does not change the sensitivity a substantial amount. At the mid

and high frequencies, however, the sensitivity begins to drop. When compared to the standard shotgun tube, though, the difference in sensitivity remains fairly uniform.

	G (300 Hz)	*G* (1000 Hz)	*G* (1600 Hz)
Standard Shotgun Tube	-4.3	-16.8	-22.4
Ascending Hole Radii	-5.4	-16.8	-22.6
Descending Hole Radii	-3.2	-16.7	-22.1
Ascending Resistance	-6.7	-17.2	-22.5
Descending Resistance	-5.9	-17.1	-22.4
Ascending Mass	-36.0	-49.7	-55.1
Descending Mass	-35.9	-49.8	-54.9

Table 8.2. Relative sensitivity values for seven configurations with an input of one volt at one meter for three frequencies.

When the beamwidth curves, on-axis frequency response, and sensitivity are all taken into account, it seems that a shotgun tube with a descending resistance profile applied to the holes is the best configuration shown thus far. Figure 8.7 showed that this profile has a much improved beamwidth curve from the standard shotgun tube. Table 8.2 shows that the sensitivity is no worse than the standard shotgun tube. Finally, Fig. 8.15 provides a plot of the on-axis frequency response for the descending resistance profile tube compared to the loudspeaker radiating into free-space mounted in a sphere containing a volume equal to that of the shotgun tube source model. While this resistance profile response is not as high as the free-field source response, the exceptional directivity control makes it an excellent option for applications requiring highly directional sources.
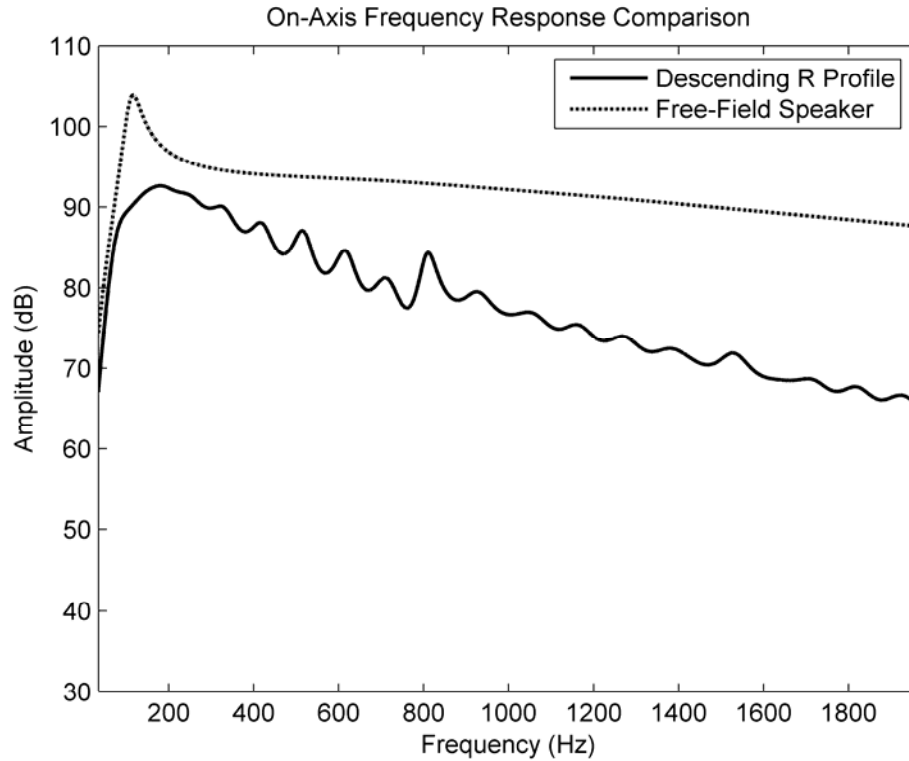
Figure 8.15. On-axis frequency response comparison for the descending resistance profile (solid trace) and a loudspeaker radiating into free-space (dashed trace).

8.4   High-Frequency Source Integration

The original goal of this research was to design a device that could be used to control the beamwidth of sound at low frequencies. The work thus far has shown that this can be accomplished with a shotgun tube. However, if such a device cannot be integrated with a directional high-frequency radiator, the usability of the shotgun tube in the commercial market decreases.

In order to investigate whether or not a combination of low and high-frequency drivers could be accomplished, a compression driver and horn were mounted on the end of each prototype. The compression driver shown in Fig. 8.16 had a sensitivity of 105 dB

with a one watt input and measured at one meter from the mouth between 250 and 4 kHz. The driver was mounted to the exponential horn shown in Fig. 8.17. The arrangement was then mounted to the end of each shotgun tube as shown in Fig. 8.18.

Figure 8.16. High-frequency source. A University Sound ID75 compression driver.

Figure 8.17. High-frequency horn attached to the compression driver. A Selenium HL14-25 exponential horn.

Figure 8.18. Long shotgun tube with high-frequency compression driver mounted on the end.

A close look at Fig. 8.18 reveals a crossover mounted to the top of the low-frequency source behind the shotgun tube. A close-up of the crossover is shown in Fig. 8.19. The impedance and frequency response of each driver was measured and imported into LSPCad Professional, to produce the crossover design. The measured frequency response of the full-bandwidth long prototype is shown in Fig. 8.20.
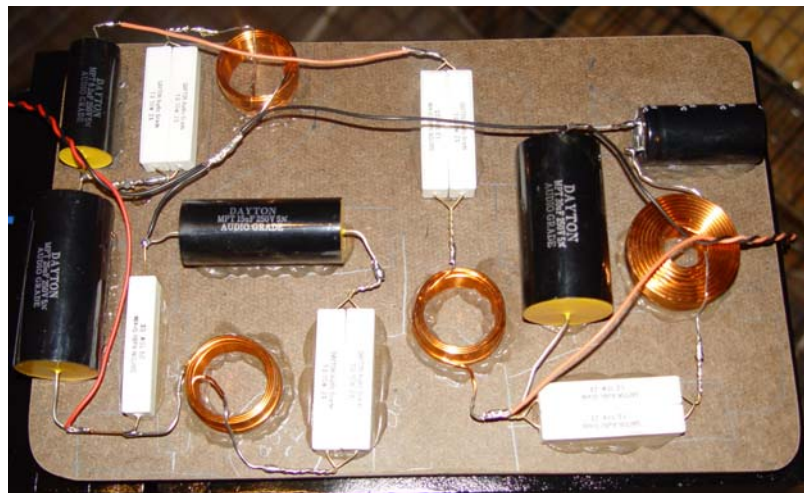
Figure 8.19. Crossover for the integration of a high-frequency compression driver with the shotgun tubes.

151
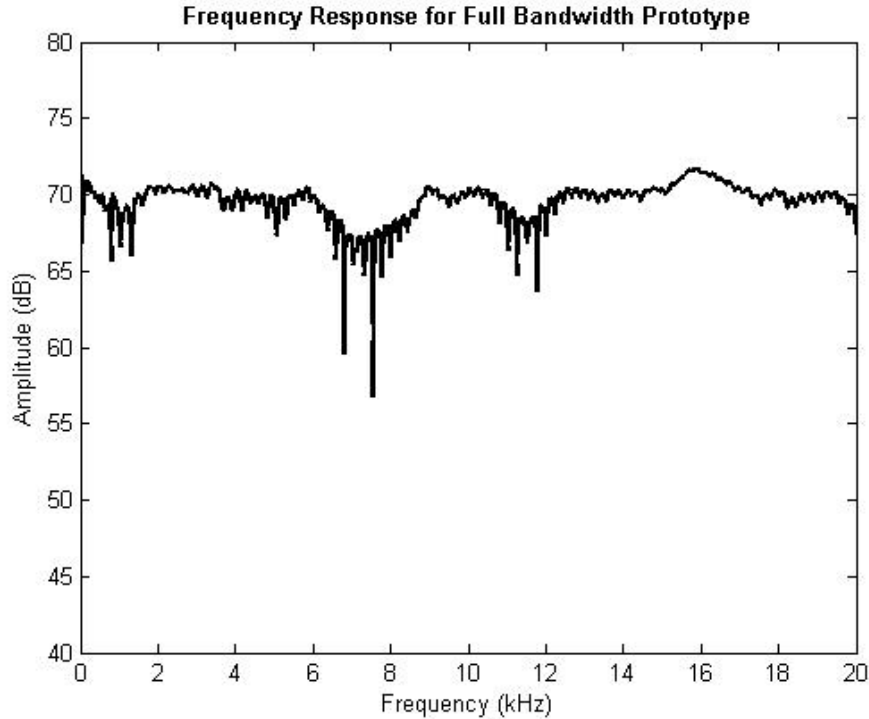
Figure 8.20. Measured on-axis frequency response of the full-bandwidth prototype.

The beamwidth curve was measured in the same manner as the low-frequency prototypes themselves, where a single microphone is held stationary in the far-field of the device. The horn-loaded shotgun tube was then rotated on a turntable and the 6 dB down points were found. The beamwidth curves for the long prototype with and without the high-frequency driver are plotted in Fig. 8.21. Similar measurements for the short prototype are plotted in Fig. 8.22.

A few things are clear from these two plots. First, as expected, the crossover region (centered around 1300 Hz) shows wild fluctuations that are a result of interference between the shotgun tube and the compression driver output. These unwanted interactions can be reduced by using a higher-order crossover to minimize the frequency content common to both drivers.

152

Second, at frequencies beyond the crossover region, the curve converges back to the modeled curve. This suggests that the exponential horn used in these measurements provides a reasonable match for integration with a shotgun tube.
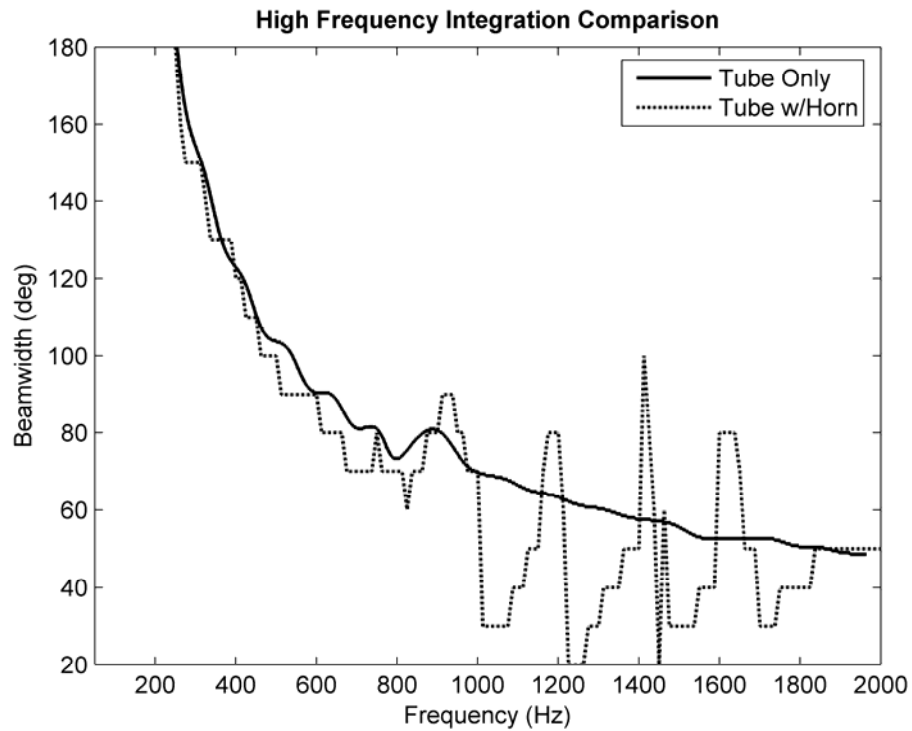
Figure 8.21. Beamwidth curve comparison for the long tube with an anechoic termination. The solid trace is the original long prototype beamwidth curve. The dashed trace is the same tube but with a high-frequency driver and horn attached to the end of the tube.
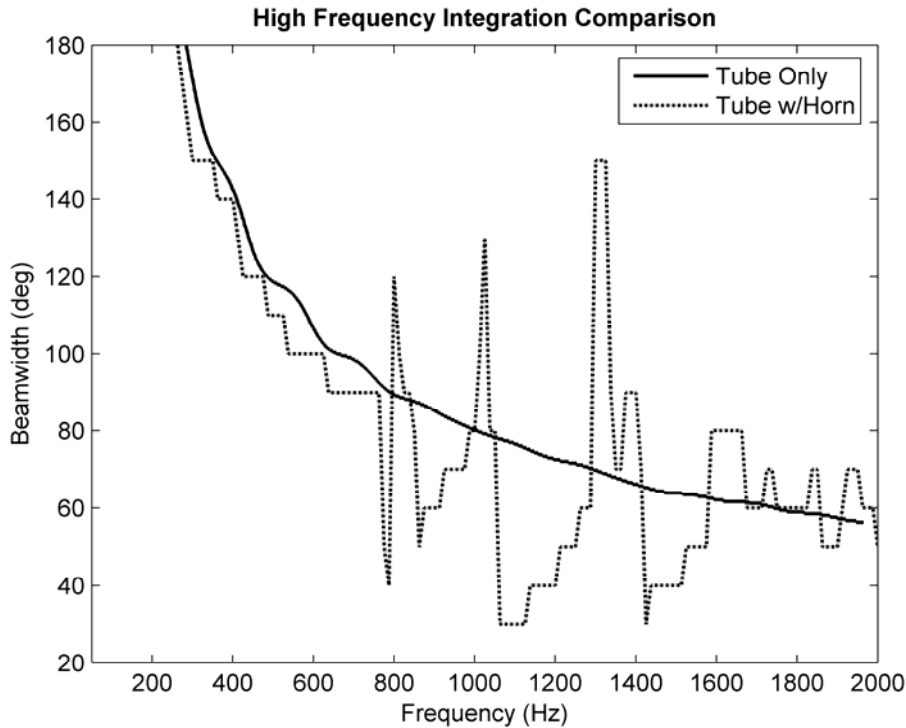
Figure 8.22. Beamwidth curve comparison for the short tube with an anechoic termination. The solid trace is the original short prototype beamwidth curve. The dashed trace is the same tube but with a high-frequency driver and horn attached to the end of the tube.

8.5 Directivity Comparison

For a simple comparison, Fig. 8.23 shows three beamwidth curves. The first curve (solid trace) is for a long shotgun tube with the physical characteristics given in Table 6.1. A descending resistance profile is applied to the holes. The second curve (dashed trace) is the measured beamwidth curve for a dual-parabolic dome (FP6030) provided to us by Soundtube Entertainment. Finally, the third curve (dotted trace) is for a baffled circular piston of radius $a = 5.24\,cm$ radiating into a semi-infinite free space. This third trace was added to the plot to show how radiation from a driver of the same size used in the shotgun tube differs in the far-field. Note that the maximum beamwidth the disk can reach is only 180˚ due to the infinite baffle in which it is mounted.

154

It is apparent that the baffled piston never becomes non-omnidirectional in our frequency range of interest. This is due to the small radius of the driver used with the shotgun tube. Figure 8.24 shows the same comparison, but now the radius of the disk mounted in an infinite baffle has been doubled and it finally reaches a point of non-omnidirectionality at approximately 1200 Hz. This comparison shows that the final shotgun tube design performed better than several available products on the market today.
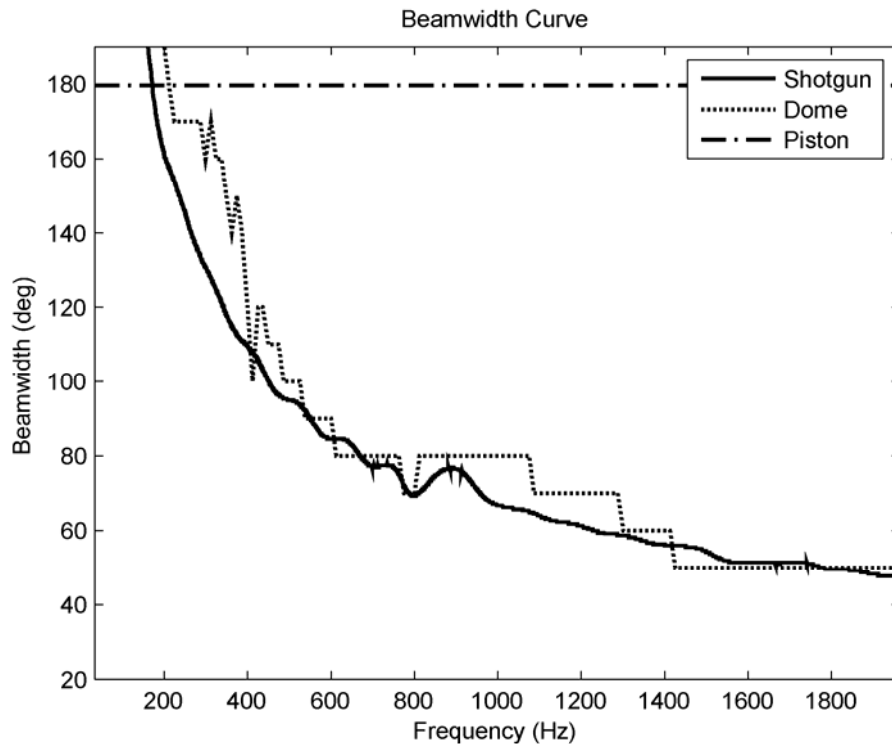
Figure 8.23. Beamwidth curve comparison between a shotgun tube (solid trace), dual-parabolic dome (dotted trace), and a circular piston mounted in an infinite baffle (dashed trace).
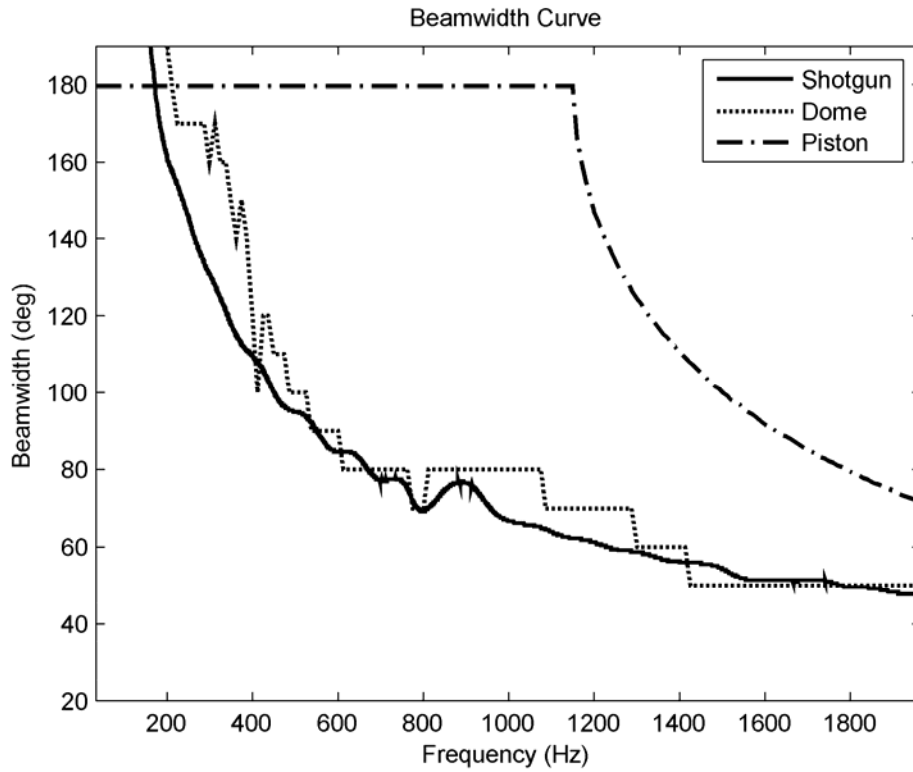
Figure 8.24. Beamwidth curve comparison between a shotgun tube (solid trace), dual-parabolic dome (dotted trace), and a circular piston mounted in an infinite baffle (dashed trace). The piston radius has been doubled from the simulation shown in Fig. 8.23.

CHAPTER 9

CONCLUSIONS

The preceding chapters have presented many different simulations of shotgun tube loudspeakers configurations, measurement results from prototype evaluations, and comparisons between the measurements and simulations. Further numerical simulations of shotgun tube variations were also presented and the results were discussed. This chapter summarizes what was learned throughout the research project and makes suggestions for future work beyond the scope of this thesis.

A shotgun tube loudspeaker may be modeled as a passive end-fire array employing a single loudspeaker coupled to a plane-wave tube with holes along the side. This modeling approach was shown to predict radiated far-field sound fields with reasonable accuracy. Additionally, improvements to the model were shown to improve the predictive capabilities of the model, including accurate far-field amplitude values and electric input impedance curves.

The overall length of the array was found to be the single most influential factor in the directional performance of the shotgun loudspeaker. The longer the tube, the better the performance (as evaluated by the beamwidth curves). Other factors that improve performance included an increased number of holes in the tube, increased spacing between holes, increased tube radius, and decreased hole radius. However, the impact of these factors was less dramatic.

An anechoic termination to a shotgun tube clearly delivers the best directional performance when compared to the other termination possibilities. The trade-off is that

an anechoic wedge typically needs to be on the order of one-forth the lowest wavelength of interest. This can prove to be a problem for many commercial applications where space is at a premium and shotgun tube length needs to be minimized.

This research has also revealed two major shortcomings of the shotgun tube design. First, there is the problem of spatial aliasing where the half-wavelength of interest is equal to the spacing between holes which results in directing energy in large side lobes. Second, the relative sensitivity of the shotgun tube is much lower than typical devices currently on the market which increases the amount of required input power.

Applying a descending resistance profile to the tube holes increases the performance at all frequencies when compared to the standard shotgun tube with equal resistance per hole. The cost of this improvement is a decrease in sensitivity or output power from the tube. Using a mass profile or variable hole radii did not result in any substantial improvement.

Finally, it has been shown that the integration of a shotgun tube and a high-frequency device is possible. However, there are interference effects present near the cross-over frequency which could be addressed in future work.

9.1 Future Work

Throughout the course of this research, several additional areas of investigation into the shotgun tube behavior have been brought to light that have not been fully explored. The following list may be used as a basis for further efforts:

- A more complete understanding of the tube resonances created by the holes is needed.

158

- Although variable hole radii have been investigated, variable hole spacing was not. This will also change the directivity and the harmonic structure of the acoustic input impedance. This may also have a drastic effect on eliminating spatial aliasing in the far-field.

- Vent noise created at the holes of the tube was mentioned but not investigated in this project. Measurements could be taken to quantify the level of the noise produced if the hole radii are too small.

- A nonuniform cross-sectional area over the length of the tube.

- Chapter 8 discussed the effect resistance and mass profiles have on the beamwidth and frequency response, but no physical measurements were made. Shotgun tubes with small resistive patches or radiating drone cones should be fabricated and measured for comparison with analytical results.

- More investigation into coupling a shotgun tube with a high-frequency device is also needed. Different horn flares or crossover designs should be examined.

- Finally, the level of the side lobes in relation to the main frontal lobe was mentioned early on in this thesis, but not as a measure of performance. The effect that side lobe levels have on perceived performance could also be investigated.

REFERENCES

[1]   T. N. Carnes, D. D. Reynolds and E. L. Hixson, "Analytical Modeling of Wave Interference Directional Microphones," J. of Eng. for Industry, vol. 103, pp. 361-371, (1981).

[2]   H. F. Olson, "Directional Microphones," J. Audio Eng. Soc., vol. 15, pp. 420-430, (1967 no. 4).

[3]   H. F. Olson, "The Quest for Directional Microphones at RCA," J. Audio Eng. Soc., vol. 28, pp. 776-786, (1980 no. 11).

[4]   W. P. Mason and R. N. Marshall, "A Tubular Directional Microphone," J. Acoust. Soc. Am., vol. 10, pp. 206-215, (1939).

[5]   M. M. Boone and O. Ouweltjes, "Design of a Loudspeaker System with a Low-Frequency Cardioidlike Radiation Pattern," J. Audio Eng. Soc., vol. 45, pp. 702-706, (1997 no. 9).

[6]   H. F. Olson, "Gradient Loudspeakers," J. Audio Eng. Soc., vol. 21, pp. 86-93, (1973 no. 2).

[7]   K. R. Holland and F. J. Fahy, "A Low-Cost End-Fire Acoustic Radiator," J. Audio Eng. Soc., vol. 39, pp. 540-550, (1991 no. 7/8).

[8]   H. F. Olson, *Elements of Acoustical Engineering*, D. Van Nostrand Company, Inc., 1940 and 1947.

[9]   L. J. Ziomek, *Fundamentals of Acoustic Field Theory and Space-Time Signal Processing*, CRC Press, 1995.

[10]   L. E. Kinsler, A. R. Frey, A. B. Coppens, and J. V. Sanders, *Fundamentals of Acosutics 4th Edition*, John Wiley and Sons, Inc., New York, 1982.

[11]   T. N. Carnes, *Analysis and Design of Wave Interference Directional Microphones*, The University of Texas at Austin, Ph.D. Dissertation, Physics Department, 1976.

[12]   T. W. Leishman, *Physics 562 Class Notes*, Department of Physics and Astronomy, 2003.

[13]   L. L. Beranek, *Acoustics*, McGraw-Hill, 1954 and Acoustical Society of America, 1986.

[14]   F. G. Leppington, "On the Theory of Woodwind Finger Holes," J. of Sound and Vib., vol. 83, pp. 521-532, (1982 no. 4).

[15]   D. H. Keefe, "Theory of the Single Woodwind Tone Hole," J. Acoust. Soc. Am., vol. 72, pp. 676-687, (1982 no. 3).

[16]   D. H. Keefe, "Experiments on the Single Woodwind Tone Hole," J. Acoust. Soc. Am., vol. 72, pp. 688-699, (1982 no. 3).

[17]   J. Kergomard, "Tone Hole External Interactions in Woodwinds Musical Instruments," 13th International Congress on Acoustics, Yugoslavia, vol. 3, pp 53-56, (1989).

[18]   A. D. Pierce, *Acoustics, An Introduction to its Physical Principles and Applications*, Acoustical Society of America, New York, 1991.

[19]   H. P. Neff, Jr., "Mutual Impedance of Circular Pistons," J. Audio Eng. Soc., vol. 43, pp. 695-699, (1995 no. 9).

[20]   E. Skudrzyk, *The Foundations of Acoustics, Basic Mathematics and Basic Acoustics*, Springer – Verlag, New York, 1971.

APPENDIX A

MEASURING REFLECTION COEFFICIENTS IN A PLANE-WAVE TUBE

One of the improvements made to the numerical model in Chapter 7 was the use of measured reflection coefficients to calculate the termination impedances for the anechoic and rigid shotgun tube terminations. The theory behind how these variables are calculated will be detailed in this appendix [12].

Figure A.1 shows a diagram of a plane-wave tube measurement system. This setup consists of a loudspeaker coupled to a cylindrical duct of length L terminated with an arbitrary impedance Z_T. The incident pressure wave, p_i, created at the loudspeaker propagates down the tube where a reflected pressure wave, p_r, is sent back towards the source. The total pressure field created by the superposition of the two opposing waves is sampled at two points in the tube, p_1 and p_2, by microphones whose outputs are denoted by e_1 and e_2, as shown in Fig. A.1.
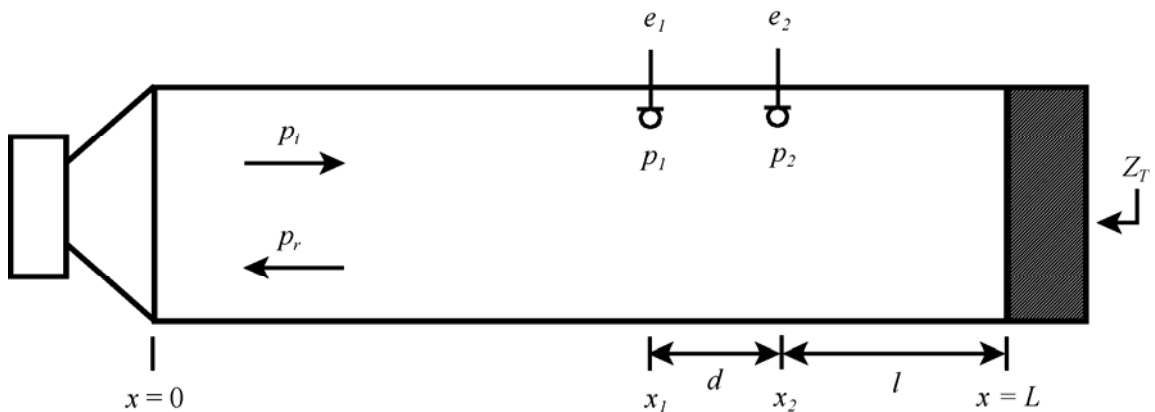
Figure A.1. Diagram of plane-wave tube.

The total pressure field inside the tube can be described by the superposition of the right-going incident wave and the left-going reflected wave by,

$$p(x) = p_i + p_r = Ae^{jk(L-x)} + Be^{-jk(L-x)} \tag{A.1}$$

where x is the position along the tube, L is the length of the tube, and A and B are the amplitudes of the incident and reflected waves, respectively. The total pressure detected by each of the two microphones can be written as,

$$p_1 = p(x_1) = Ae^{jk(l+d)} + Be^{-jk(l+d)} \tag{A.2}$$

$$p_2 = p(x_2) = Ae^{jkl} + Be^{-jkl} \tag{A.3}$$

where d is the spacing between microphones and l is the distance from the second microphone to the tube termination, as shown in Fig. A.1.

The reflection coefficient is defined as the reflected wave divided by the incident wave and gives a measure of how much energy is reflected back at a given measurement point. At any point in the tube, this coefficient can be given by,

$$R(x) = \frac{p_r(x)}{p_i(x)} = \frac{Be^{-jk(L-x)}}{Ae^{jk(L-x)}} = \frac{B}{A}e^{-j2k(L-x)}. \tag{A.4}$$

This then gives us a method for finding the reflection coefficient at the tube termination and each of the two microphones.

$$R(L) = \frac{B}{A} \tag{A.5}$$

$$R(x_1) = \frac{B}{A}e^{-j2k(l+d)} = R(L)e^{-j2k(l+d)} \tag{A.6}$$

$$R(x_2) = \frac{B}{A}e^{-j2kl} = R(L)e^{-j2kl} = R(x_1)e^{j2kd} \tag{A.7}$$

164

Equations (A.2) and (A.3) can now be written as,

$$p_1 = Ae^{jk(l+d)} + AR(L)e^{-jk(l+d)} = Ae^{jk(l+d)}\left[1 + R(x_1)\right] \qquad \text{(A.8)}$$

$$p_2 = Ae^{jkl} + AR(L)e^{-jkl} = Ae^{jkl}\left[1 + R(x_2)\right] \qquad \text{(A.9)}$$

In order to get an accurate frequency response measurement between the microphones, a relative calibration must be performed before we can proceed any further. The current test setup lends itself very nicely to the switching technique for calculating the calibration factor. The main reason for this is that the microphones are constrained to a fixed position in the tube wall. When the microphones are switched, there is essentially no error in the positioning of the microphones.

The switching technique involves two measurements for each microphone. Figure A.2 shows the initial signal path for the first set of measurements. Microphone #1 powered by electronics with frequency responses, M_1 and E_1 respectively, detects the pressure at position p_1, and outputs a voltage signal, e_{1a}. Microphone #2 does the same thing at position p_2.
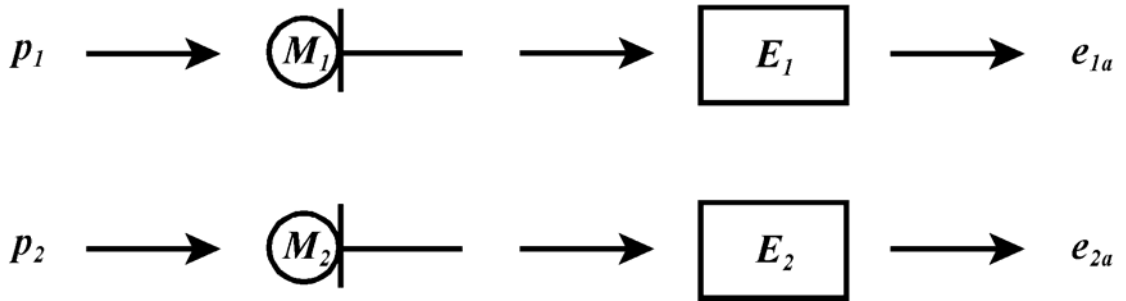
Figure A.2. Signal flow for the first step in the switching technique.

The transfer function between the two microphones is then defined as,

$$H_{12a} = \frac{e_{2a}}{e_{1a}} = \frac{p_2 M_2 E_2}{p_1 M_1 E_1}.$$ (A.10)

Next, the microphones and related electronics switch positions as shown in Fig. A.3 and the outputted voltage signals, e_{1b} and e_{2b}, are recorded.
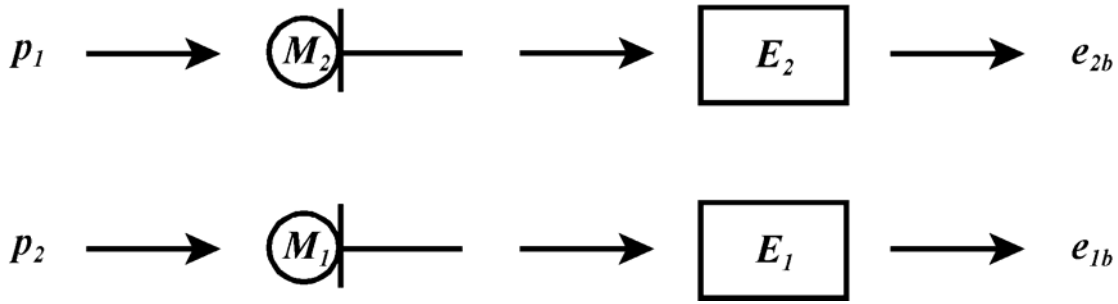
Figure A.3. Signal flow for the second step in the switching technique.

The transfer function between the two microphones in this case is given by,

$$H_{12b} = \frac{e_{2b}}{e_{1b}} = \frac{p_1 M_2 E_2}{p_2 M_1 E_1}.$$ (A.11)

A frequency-dependant calibration factor for the pair of microphones is then found by taking the geometric mean of H_{12a} and H_{12b}.

$$H_{cal,12} = \left(H_{12a} \cdot H_{12b} \right)^{\frac{1}{2}}$$ (A.12)

Using Eqs. (A.10) and (A.11), this then becomes,

$$H_{cal,12} = \left[\left(\frac{p_2 M_2 E_2}{p_1 M_1 E_1} \right) \cdot \left(\frac{p_1 M_2 E_2}{p_2 M_1 E_1} \right) \right]^{\frac{1}{2}} = \left[\frac{M_2^2 E_2^2}{M_1^2 E_1^2} \right]^{\frac{1}{2}} = \frac{M_2 E_2}{M_1 E_1}$$ (A.13)

which is our calibration factor.

Once the microphones have been relatively calibrated, $H_{cal,12}$ can be used to correct the frequency response function between the two microphones by,

$$H_{12} = \frac{\left(\dfrac{e_2}{e_1}\right)}{H_{cal,12}} = \frac{p_2}{p_1}.$$

(A.14)

Using Eqs. (A.8) and (A.9), H_{12} can be written as,

$$H_{12} = \frac{Ae^{jkl}\left[1 + R(x_2)\right]}{Ae^{jkl}e^{jkd}\left[1 + R(x_1)\right]} = \left[\frac{1 + R(x_2)}{1 + R(x_1)}\right]e^{-jkd}.$$

(A.15)

Substituting Eq. (A.7) into Eq. (A.15) gives,

$$H_{12} = \left[\frac{1 + R(x_1)e^{j2kd}}{1 + R(x_1)}\right]e^{-jkd}.$$

(A.16)

We can then solve for $R(x_1)$.

$$R(x_1) = -\left[\frac{H_{12} - e^{-jkd}}{H_{12} - e^{jkd}}\right]$$

(A.17)

Finally, substituting Eq. (A.17) into Eq. (A.6) gives our final expression for the reflection coefficient at the end of the tube as,

$$R(L) = -\left[\frac{H_{12} - e^{-jkd}}{H_{12} - e^{jkd}}\right]e^{j2k(l+d)}.$$

(A.18)

Once the reflection coefficient is known, the absorption coefficient and acoustic impedance of the termination can be found using the following two equations:

$$\alpha = 1 - \left|R^2\right|$$

(A.19)

$$Z_T = \left(\frac{\rho_0 c}{S}\right)\left[\frac{1+R}{1-R}\right].$$

(A.20)

The following pages contain all the MATLAB code developed for a numerical

representation of the shotgun tube.

Main Shotgun Tube Program

```
clear all; close all;

%%%%%  Tube Parameters  %%%%%
%A = ; %tube radius
%t = ; %thickness of tube wall
%L = ; %spacing between holes
%holes = ; %number of holes
%a_idx = ;
%a = a_calc(a_idx,holes);

%parameters for long tube
A = 5.08/100;
L = 22/100;
holes = 6;
t = 5/1000;
a = 1.27/100*ones(1,holes);
%a_idx = 2;
%a = a_calc(a_idx,holes);

%parameters for short tube
% A = 5.08/100;
% L = 11.85/100;
% holes = 8;
% t = 5/1000;
% a = 0.635/100*ones(1,holes);
% %a_idx = 1;
% %a = a_calc(a_idx,holes);

model = [1 1 1 1 1];

if model(1) == 1
   load Rdata_wedge;
   %load Rdata_rigid;
   f = fnew';
else
   f = 1000:5:2500;
end

omega = 2*pi*f;
```

```matlab
theta = 0:pi/800:2*pi;
c = 343;
rho = 1.21;
k = 2*pi*f/c;
r = 5.8928;
S = pi*A^2;

if model(2) == 1
   %%%%% Compensate for Losses in the Tube %%%%%
   eta = 1.85e-5;
   Pr = 0.710;
   gam = 1.402;
   alphac = omega.^2*eta/2/rho/c^3*(4/3+(gam-1)/Pr);
   alphaw = sqrt(eta*omega/2/rho)/A/c*(1+(gam-1)/sqrt(Pr));
   alpha = alphac+alphaw;
   k = k-j*alpha;
   c = omega./k;
end

if model(1) == 1
   ZmL = (rho*c'/S.*(1+Rnew)./(1-Rnew))';
else
   ZmL = rho*c/S;
   %ZmL = 1000*rho*c/S;
end

Zm = zeros(holes,length(f));
midx = 1;
switch midx
   case 1
      for n = 1:holes
         Zm(n,:) = rho*c.*k.^2/4/pi+j*omega*(rho*t/pi/a(n)^2+0.5*rho/a(n));
      end
   case 2
      %%%%% Resistance Profile %%%%%
      minR = 0;
      maxR = 100000;

      for n = 1:holes
         Zm(n,:) = rho*c.*k.^2/4/pi+j*omega*(rho*t/pi/a(n)^2+0.5*rho/a(n));
      end
      holeZr = holeZres(f,holes,minR,maxR);
      Zm = Zm+holeZr;
   case 3
      %%%%% Mass Profile %%%%%
      Cms = 1893/1e6; %m/N
      Sd = 6/10000; %m^2
      Rms = 0.106; %kg/s
      minMms = 0.5/1000; %kg
      maxMms = 2/1000; %kg

      [holeZm,holeZmrad] = holeZmass(f,holes,minMms,maxMms,Cms,Sd,Rms);
      Zm = holeZm+holeZmrad;
end
```

```
if model(3) == 1
    %%%%% Compensate for Mutual Radiation Impedances %%%%%
    for n = 1:holes
        tempd = [(1-n)*L:L:(holes-n)*L];
        d_idx = find(tempd ~= 0);
        d = tempd(d_idx);
        for m = 1:holes-1
            Rmut(m,:) = 2*besselj(1,k*a(n)).*besselj(1,k*a(n)).*sin(k*d(m))./k/d(m);
            Xmut(m,:) = 2*besselj(1,k*a(n)).*besselj(1,k*a(n)).*cos(k*d(m))./k/d(m);
        end
        Zmut(n,:) = sum(Rmut,1)+j*sum(Xmut,1);
    end
    Zm = Zm+Zmut;
end


f1 = j*rho*c.*tan(k*L/2)/S;
f2 = -j*rho*c.*csc(k*L)/S;


N = (holes-1)*4+7;
Z = zeros(N,length(f));
for n = 1:N;
    if n == 1
        Z(N-n+1,:) = ZmL+f1;
    elseif mod(n,2) == 0
        if mod(n,4) ~= 0
            Z(N-n+1,:) = 1./(1./Z(N-n+2,:)+1./f2);
        elseif mod(n,4) == 0
            m = n/4;
            Z(N-n+1,:) = 1./(1./Z(N-n+2,:)+1./(Zm(holes+1-m,:)));
        end
    elseif mod(n,2) == 1
        Z(N-n+1,:) = f1+Z(N-n+2,:);
    end
end


if model(4) == 1
    %%%%% Compensation for Air Gap %%%%%
    T = 0.0191;

    f1e = j*rho*c.*tan(k*T/2)/S;
    f2e = -j*rho*c.*csc(k*T)/S;
    Ztemp = f1e+1./(1./f2e+1./(f1e+Z(1,:)));

    Sg = pi*0.0762^2;
    f1g = j*rho*c.*tan(k*T/2)/Sg;
    f2g = -j*rho*c.*csc(k*T)/Sg;
    Zinput = f1g+1./(1./f2g+1./(f1g+Ztemp));
else
    Zinput = Z(1,:);
end


if model(5) == 1
    %%%%% New Speaker Model %%%%%
    eg = 2.83;
    [boxU,Zest,Zesff] = speak(eg,f,Zinput);
```

170

```
else
   boxU = ones(1,length(f));
end

utemp = zeros(holes*2,length(f));
for d = 1:holes*2
   if d == 1
      if exist('Sg') == 1
         ucava = boxU.*f2g./(f2g+Ztemp+f1g);
         ucavb = ucava.*f2e./(f2e+Z(1,:)+f1e);
         utemp(1,:) = ucavb.*f2./(f2+Z(3,:));
      else
         utemp(1,:) = boxU.*f2./(f2+Z(3,:));
      end
   elseif mod(d,2) == 0
      utemp(d,:) = utemp(d-1,:).*Zm(d/2,:)./(Zm(d/2,:)+Z(2*d+1,:));
   elseif mod(d,2) == 1
      utemp(d,:) = utemp(d-1,:).*f2./(f2+Z(2*d+1,:));
   end
end

if exist('Sg') == 1
   utemp = [ucavb ; utemp];
else
   utemp = [boxU ; utemp];
end
utemp2 = -1*diff(utemp,1,1);

U = zeros(holes,length(f));
for g = 1:holes
   U(g,:) = utemp2(2*g,:);
end

L2 = zeros(holes,1);
if mod(holes,2) == 1
   for n = 1:(holes-1)/2
      L2(n) = -((holes-1)/2-n+1)*L;
      L2(holes-n+1) = -L2(n);
   end
   L2((holes-1)/2+1) = 0;

elseif mod(holes,2) == 0
   for n = 1:holes/2
      L2(n) = -(holes/2-n+0.5)*L;
      L2(holes-n+1) = -L2(n);
   end
end

Ptemp = zeros(holes,length(theta));
temp = (length(theta)-1)*3/4;
b = 1;
gui_active(1);
h = progressbar([],0,'Calculating...');
M = length(f);
for F = 1:M
```

```matlab
        h = progressbar(h,1/M);
        if ~gui_active
            break;
        end

        for n = 1:holes
            if model(2) == 1
                Ptemp(n,:) = j*rho*c(F)*k(F)*U(n,F)*exp(-j*k(F)*(r+L2(n)*sin(theta)))/4/pi/r;
            else
                Ptemp(n,:) = j*rho*c*k(F)*U(n,F)*exp(-j*k(F)*(r+L2(n)*sin(theta)))/4/pi/r;
            end
        end

        P2 = sum(Ptemp);
        if model(5) == 1
            Beam = 20*log10(abs(P2)/20e-6);
        else
            Dir = P2./max(abs(P2));
            Beam = 20*log10(abs(Dir))+50;
            idx = find(Beam < 0);
            Beam(idx) = 0;
        end

        Beam = [Beam(temp:end) Beam(1:temp-1)];

        for n = 1:length(Beam)/2
            da = Beam(1)-Beam(n);
            if da >= 6
                break;
            end
        end
        step = theta(2);
        width(b) = 2*((n-1)*step/pi*180);
        data(b,:) = Beam;
        b = b+1;
    end

progressbar(h,-1);

%cuttoff frequency for tube of radius A
fc = 1.84*343/2/pi/A;

figure;
plot(f,width,'k-','LineWidth',1.5);
title('Beamwidth Curve','FontWeight','Bold');
xlabel('Frequency (Hz)');
ylabel('Beamwidth (\theta)');
xlim([f(1) f(end)]);
ylim([20 370]);
```

Calculate Hole Radii for Variable Configuration

```
function [a] = a_calc(a_idx,holes);

switch a_idx
  case 1
    a = 1.27/100*ones(1,holes);
  case 2
    amin = 0.52/100; %m
    amax = 2.02/100; %m

    aconfig = 2;
    switch aconfig
      case 1
        a = asc_desc(amin,amax,holes,1);
      case 2
        a = asc_desc(amin,amax,holes,2);
      case 3
        if mod(holes,2) == 0
          holes2 = holes/2;
          a1 = asc_desc(amin,amax,holes2,1);
          a2 = asc_desc(amin,amax,holes2,2);
          a = [a1 a2];
        else
          holes2 = (holes+1)/2;
          a1 = asc_desc(amin,amax,holes2,1);
          a2 = asc_desc(amin,amax,holes2,2);
          a = [a1 a2(2:end)];
        end
      case 4
        if mod(holes,2) == 0
          holes2 = holes/2;
          a1 = asc_desc(amin,amax,holes2,2);
          a2 = asc_desc(amin,amax,holes2,1);
          a = [a1 a2];
        else
          holes2 = (holes+1)/2;
          a1 = asc_desc(amin,amax,holes2,2);
          a2 = asc_desc(amin,amax,holes2,1);
          a = [a1 a2(2:end)];
        end
    end
end
```

Calculate Spacing for Ascending or Descending Configurations

```
function [a] = asc_desc(mina,maxa,holes,b)

diff = maxa-mina;
da = diff/(holes-1);

for n = 1:holes
   if b == 1
      a(n) = mina+(n-1)*da; %ascending
   else
      a(n) = maxa-(n-1)*da; %descending
   end
end
```

Calculate Resistance Profiles

```
function [holeZr] = holeZres(f,holes,minR,maxR);

rindex = 2;
switch rindex
   case 1
      R = asc_desc(minR,maxR,holes,1);
   case 2
      R = asc_desc(minR,maxR,holes,2);
   case 3
      if mod(holes,2) == 0
         holes2 = holes/2;
         a1 = asc_desc(minR,maxR,holes2,1);
         a2 = asc_desc(minR,maxR,holes2,2);
         R = [a1 a2];
      else
         holes2 = (holes+1)/2;
         a1 = asc_desc(minR,maxR,holes2,1);
         a2 = asc_desc(minR,maxR,holes2,2);
         R = [a1 a2(2:end)];
      end
   case 4
      if mod(holes,2) == 0
         holes2 = holes/2;
         a1 = asc_desc(minR,maxR,holes2,2);
         a2 = asc_desc(minR,maxR,holes2,1);
         R = [a1 a2];
      else
         holes2 = (holes+1)/2;
         a1 = asc_desc(minR,maxR,holes2,2);
         a2 = asc_desc(minR,maxR,holes2,1);
         R = [a1 a2(2:end)];
      end
end

for n = 1:holes
```

```
    holeZr(n,:) = R(n)*ones(1,length(f));
end
```

Calculate Mass Profiles

```
function [holeZm,holeZmrad] = holeZmass(f,holes,minMms,maxMms,Cms,Sd,Rms);

d_index = 1;
switch d_index
    case 1
        Mms = asc_desc(minMms,maxMms,holes,1);
    case 2
        Mms = asc_desc(minMms,maxMms,holes,2);
    case 3
        if mod(holes,2) == 0
            holes2 = holes/2;
            a1 = asc_desc(minMms,maxMms,holes2,1);
            a2 = asc_desc(minMms,maxMms,holes2,2);
            Mms = [a1 a2];
        else
            holes2 = (holes+1)/2;
            a1 = asc_desc(minMms,maxMms,holes2,1);
            a2 = asc_desc(minMms,maxMms,holes2,2);
            Mms = [a1 a2(2:end)];
        end
    case 4
        if mod(holes,2) == 0
            holes2 = holes/2;
            a1 = asc_desc(minMms,maxMms,holes2,2);
            a2 = asc_desc(minMms,maxMms,holes2,1);
            Mms = [a1 a2];
        else
            holes2 = (holes+1)/2;
            a1 = asc_desc(minMms,maxMms,holes2,2);
            a2 = asc_desc(minMms,maxMms,holes2,1);
            Mms = [a1 a2(2:end)];
        end
end

Cas = Cms*Sd^2;
Mas = Mms/Sd^2;
Ras = Rms/Sd^2;

rho = 1.21;
c = 343;
omega = 2*pi*f;
k = omega/c;

ka = omega/c*sqrt(Sd/pi);
Rar = 1-besselj(1,2*ka)./ka;
Xar = real(besselh(1,2*ka)./ka);
for n = 1:holes
```

```
   holeZmrad(n,:) = rho*c/Sd*Rar+j*rho*c/Sd*Xar;
end

for n = 1:length(Mas)
   holeZm(n,:) = Ras+1./(j*omega*Cas)+j*omega.*Mas(n);
end
```

Calculate Drone Cone Radiation Impedance

```
function [ZmL] = droneZ(f);

omega = 2*pi*f;
c = 343;
rho = 1.21;

Cms = 750/1e6; %m/N
Mms = 75/1000; %kg
Rms = 0.5; %kg/s
Sd = 0.0194; %m^2

Cas = Cms*Sd^2;
Mas = Mms/Sd^2;
Ras = Rms/Sd^2;

ka = omega/c*sqrt(Sd/pi);
Rar = rho*c/Sd*ka.^2/4;
Mar = rho*c/Sd*0.61*ka;

Zdriver = Ras+1./(j*omega*Cas)+j*omega*Mas;
Zrad = Rar+j*Mar;

ZmL = Zdriver+Zrad;
```

Calculate Speaker Diaphragm Impedance and Volume Velocity Output

```
function [Ut,Zest,Zes] = speak(eg,f,Zinput)

rho = 1.21;
c = 343;
omega = 2*pi*f;

%%% ST woofer T/S parameters %%%
a = 0.0524; %radius of diaphragm in m
Sd = pi*a^2; %surface area in m^2
Fs = 73.6885; %free-air resonance (from MLSSA)
Qms = 3.0355; %(from MLSSA)
```

```
Mms = 9.6645/1000; %kg (from MLSSA)
Cms = 482.7695/1e6; %m/N (from MLSSA)
Bl = 6.5975; %Tm (from MLSSA)


Re = 5.4225; %ohms (from MLSSA)
L1 = 0.152/1000; %H (from MLSSA)
L2 = 0.488/1000; %H (from MLSSA)
R2 = 16.553; %ohms (from MLSSA)
Rg = 0.1; %internal resistance of signal generator (typical value is approx 0.1 ohms)


Mmd = Mms-8/3*rho*a^3; %Mms-mass of fluid loading
Mad = Mmd/Sd^2; %acoustic mass of driver
Cas = Cms*Sd^2; %acoustic compliance of driver
Rms = 1/2/pi/Fs/Cms/Qms; %acoustic resistance of driver
Ras = Rms/Sd^2;


%%%%  voice coil parameters -- Zr->elements in MM domain, Zra->elements in AI domain
Zr = (Rg+Re+j*omega*L1)/Bl^2+j*omega*L2*R2/Bl^2./(j*omega*L2+R2); %Rg+Re+L1+L2//R2
Z1 = Bl^2/Sd^2/(Rg+Re);
Z2 = j*omega*L1/Bl^2/Sd^2;
Z3 = Bl^2/Sd^2/R2+j*omega*L2/Bl^2/Sd^2;
Zra = 1./(1/Z1+1./Z2+1./Z3);


psource = eg/Bl/Sd./Zr;


%dimensions of box in m
D = 0.1905; %depth (7.5")
W = 0.1397; %width (5.5")
H = 0.1397; %height (5.5")
V = D*W*H; %internal volume of box in m^3


M = 30;
Zar = Zcalc(V,a,f,M,1); %cap in sphere
Rar = real(Zar);
Mar = imag(Zar);


Rab = 10000; %acoustic resistance of box
Mab = 0.3*rho*a/Sd; %acoustic mass of box
Cab = V/rho/c^2; %acoustic compliance of box


Zdriver = Ras+1./(j*omega*Cas)+j*omega*Mad; %combined Z of driver
Zbox = Rab+1./(j*omega*Cab)+j*omega*Mab; %combined Z from box


%%% calculate the input impedance for the tube and volume velocity at the diaphragm
Zradt = Zinput; %Zinput from tube
Zast = Zra+Zdriver+Zradt+Zbox;
Zest = Zr*Bl^2+Bl^2/Sd^2./(Zast-Zra)-Rg;
Zest = abs(Zest);
Ut = psource./Zast;


%%% calculate the input impedance as if there were no tube attached to the driver
Zrad = Rar+j*Mar; %combined Z from radiation terms
Zas = Zra+Zdriver+Zrad+Zbox;
Zes = Zr*Bl^2+Bl^2/Sd^2./(Zas-Zra)-Rg;
```

```
Zes = abs(Zes);
U = psource./Zas;
Wt = abs(U.^2).*Rar;
pff = sqrt(rho*c*Wt);
pref = sqrt(rho*c*10^-12);
pffdB = 20*log10(pff/pref);
```

Calculate Radiation Impedance for a Free-Field Loudspeaker

```
function Zar = Zcalc(aveV,ac,f,M,b)

u0 = 1;
a = (aveV*3/4/pi)^(1/3);
theta0 = asin(ac/a);
theta = 0;
Sc = 4*pi*a^2*sin(theta0/2)^2;

omega = 2*pi*f;
c = 343;
rho = 1.21;
k = omega/c;
ka = k*a;
kac = k*ac;

gui_active(1);
if b == 1
   h = progressbar([],0,'Calculating Driver Response...');
elseif b == 2
   h = progressbar([],0,'Calculating Port Response...');
end

Zar = 0;
for n = 1:M
   m = n-1;

   h = progressbar(h,1/M);
   if ~gui_active
      break;
   end

   if m == 0
      Um = u0/2*(1-cos(theta0));
   else
      Pp = legendre(m+1,cos(theta0));
      Pm = legendre(m-1,cos(theta0));
      Um = u0/2*(Pm(1)-Pp(1));
   end

   jmp = sqrt(pi/2./ka).*besselj(m+1+0.5,ka);
   jmn = sqrt(pi/2./ka).*besselj(m-1+0.5,ka);
   nmp = sqrt(pi/2./ka).*bessely(m+1+0.5,ka);
   nmn = sqrt(pi/2./ka).*bessely(m-1+0.5,ka);
```

```matlab
    for mm = 1:length(nmp)
       if nmp(mm) ~= Inf
          break;
       end
    end

    for nn = 1:mm-1
       nmp(nn) = nmp(mm);
       nmn(nn) = nmn(mm);
    end

    delta = atan(((m+1)*jmp-m*jmn)./(m*nmn-(m+1)*nmp));

    D = ((m+1)*jmp-m*jmn)/(2*m+1);
    for mm = 1:length(D)
       if D(mm) ~= 0
          break;
       end
    end

    for nn = 1:mm-1
       D(nn) = D(mm);
    end

    Bm = D./sin(delta);

    jm = sqrt(pi/2./ka).*besselj(m+0.5,ka);
    nm = sqrt(pi/2./ka).*bessely(m+0.5,ka);
    h2 = jm-j*nm;

    for mm = 1:length(h2)
       if abs(h2(mm)) == Inf
          h2(mm)=0;
       end
    end

    Zar = Zar+rho*c*4*pi*a^2/(u0*Sc)^2*Um^2./Bm/(2*m+1).*exp(j*delta).*h2;
end

progressbar(h,-1);
```